Nanomanufacturing towards Flexible Electronic and Photonic Devices

Yu Shu

Supervised by Professor Harish Bhaskaran



Wolfson College

Department of Materials

University of Oxford

A thesis submitted for the degree of

Doctor of Philosophy

Trinity 2022

This thesis is dedicated to

my parents and grandparents

Acknowledgement

I greatly appreciate the memorable DPhil student life in Oxford where all happiness and sadness make a better me. This thesis cannot be achieved without massive care and support from my laboratory colleagues, friends and family during the past four years.

First of all, I would like to thank my supervisor Professor Harish Bhaskaran for his guidance and encouragement to make me confidently overcome each difficulty on the way to pursuing the research. All the one-to-one meetings with him effectively addressed my confusions and problems as a new student in the first year, which significantly improve my confidence and help me independently conduct research in the following years. I am very grateful as he always gives full support to my trials of new ideas. He is always my favourite supervisor in the life.

Thank every colleague of the Advanced Nanoscale Engineering group for all your help and collaborations. Particularly I would like to show my sincere gratitude to Dr. Benjamin Porter, Dr. Nhlakanipho Mkhize for the guidance and mentorship of being a good researcher. A big thank you to Dr. Eugene Soh, Dr. Sridevi Siddarama, Dr. Mengyun Wang, Dr. Nikolaos Farmakidis and Dr. Seongdong Lim for all the support and discussions while carrying out my projects. I am also grateful to my collaborators Professor Jamie Warner, Dr. Feras Alkhalil and Dr. Satyajit Das from Pragmatic Semiconductor Ltd. for your contributions to my projects. All your efforts have made my research achievement.

I appreciate the precious friendship during my DPhil life. To my bestie Utku Emre Ali, I owe you the deepest gratitude. We joined the group at the same time and have witnessed each other's remarkable progress in the past four years. I enjoy a lot of fun with him walking and chatting in the University Park. I feel so happy to share the same hobby with him as a tea lover. He always stands with me and trusts me, which gives me enormous courage and braveness. In addition, I would like to appreciate my amazing friends and colleagues James, Tara, Xuan, Wen, Bowei, Samarth, Jason, Yuhan, Yi, Antonios, Havard, Kairan and Luci

for all the valuable and enjoyable moments. To all my best friends from my hometown, thank you for the endless care and backing even though we are far away from each other.

Finally, a special thank you to my most important family for their unconditional love and indefinite support. The life attitudes of my parents and grandparents have taught me how to be optimistic all the time and never give up. The warmth gained from them always illuminates the darkness on the way of my growth. To my baby cat Latte, thank you for all the happiness and comfort since your coming. I am also grateful to my dearest boyfriend Yang Lu, who always accompanies and supports me especially during the hardest pandemic lockdown period and every frustrating day due to experimental failures.

Yu Shu

09/2022

Abstract

Nanomanufacturing plays a dominant role in the invention of advanced devices based on wearable and flexible technology. Most conventional nanomanufacturing techniques inevitably require the use of hazardous chemicals during the fabrication process, releasing a great amount of chemical wastes. Thus, sustainability has become a crucial concern in order to avoid contaminations to the environment. The utilisation of harsh solvents and strong radiation in existing fabrication processes also restricts applications in sensitive materials such as polymers, two-dimensional materials (2DMs) and biomaterials, because the degradation or creation of defects is prone to occur while processing these materials. Both the sustainability concern and the vulnerability of flexible materials require the minimisation of using hazardous chemicals in novel nanomanufacturing techniques. In this thesis, I explored both novel and existing nanomanufacturing techniques that are sustainable and integrated them with sensitive materials.

The first demonstration is the development of an environmentally-friendly mechanical bilayer lithography that uses just water for development and lift-off. This is achieved by using a water-soluble resist of polyvinyl alcohol (PVA). The water-based process effectively reduces the release of chemical wastes at the source, hence the enhancement of its sustainability. This technique is able to write arbitrary patterns. The highest resolution of a line pattern achieved is 310 nm. This technique is further demonstrated to be suitable for patterning on a polymeric substrate of polyethylene terephthalate (PET) which has relatively lower chemical resistance and mechanical stability than that of rigid substrates.

To further explore the applicability of the water-based mechanical bilayer lithography, this technique is used to fabricate a flexible MoS_2 photodetector on a PET substrate. The reason to choose MoS_2 is that defects and impurities in such 2DMs tend to be induced by the strong radiation and harsh organic solvents in conventional fabrication process. The difference in the device performance of two flexible MoS_2 photodetectors fabricated by the mechanical

bilayer lithography and conventional photolithography is investigated. The photodetector fabricated by the mechanical bilayer lithography shows a faster response time of 42 ms due to less defects created during the water-based fabrication process.

In the final part of the thesis, I seek the opportunity of using biomolecules as the ink in the low-cost and rapid prototyping electrohydrodynamic printing (EHD printing) technique. The EHD printing is shown to be able to achieve the on-demand functionalisation of thin-film transistors (TFTs) for biosensing applications. Compared to other covalent functionalisation techniques such as drop casting, the on-demand characteristic of EHD printing enables a great reduction of the waste of materials. The localised functionalisation is achieved by EHD printing of 3-Aminopropyl)triethoxysilane (APTES) and the antibody of cardiac troponin I (cTnl) protein in sequence on the selected semiconductor channels in an array of TFTs. The negative shift of the threshold voltage in the transfer characteristic of the modified TFT confirms the overall functionalisation effect of APTES and cTnl antibody. Moreover, the functionalised TFT shows a characteristic response to the presence of cTnl protein.

Table of Contents

Chapter 1 Introduction 1

1.1 From nanotechnology to nanomanufacturing 1

1.2 Sustainable nanomanufacturing for flexible technologies 3

1.3 Thesis outline 5

1.4 Key contributions 6

Chapter 2 Nanomanufacturing of flexible devices: state of the art 7

2.1 Materials for flexible devices 7

2.1.1 Polymers 8

2.1.2 Biopolymers 12

2.1.3 Nanomaterials 16

2.2 Nanomanufacturing techniques for flexible devices 23

2.2.1 Scanning probe lithography 23

2.2.2 Inkjet printing 28

2.2.3 Electrohydrodynamic printing 33

2.2.4 Direct laser writing 41

2.2.5 Nanoimprint lithography 43

2.3 Chapter summary 46

Chapter 3 Experimental methodology and metrology 50

3.1 Introduction 50

3.2 Equipment 50

3.2.1 Mechanical lithography by AFM 50

3.2.2 EHD printing setup 52

3.3 Metrology 54

3.3.1 Characterisation techniques 54

3.3.2 Electrical measurement 58
3.3.3 Photocurrent measurement 59
Chapter 4 Water-based mechanical bilayer lithography 60
4.1 Introduction 60
4.2 Aims of chapter 62
4.3 Method and materials 62
4.3.1 Spin coating of PVA and PMMA Layer 63
4.3.2 Patterning and development 63
4.3.3 Deposition and lift-off 64
4.4 Demonstration of fabrication process 64
4.4.1 Selection of bilayer resist materials 64
4.4.2 Optimisation of fabrication process 65
4.5 Write patterns with high resolution and various shapes 71
4.5.1 High resolution 71
4.5.2 Various shapes 73
4.6 Patterning on polymer substrates 74
4.7 Limitation 76
4.8 Sustainability analysis 78
4.9 Conclusions 78
4.10 Author contributions 79
Chapter 5 Fabrication of flexible MoS_2 photodetectors 80
5.1 Introduction 80
5.2 Background 81
5.2.1 Radiation effects and chemical doping of TMDs 81
5.2.2 Exfoliation of MoS_2 82

5.3 Aims of chapter 84

5.4 Methods and materials 84

5.4.1 EHD printing of liquid exfoliated MoS_2 84

5.4.2 Mechanical exfoliation of MoS_2 85

5.4.3 Characterisation of MoS_2 85

5.4.4 Fabrication of flexible MoS_2 photodetectors 85

5.4.5 Device measurement 86

5.5 Preparation of MoS_2 86

5.5.1 EHD printing of liquid exfoliated MoS_2 86

5.5.2 Mechanical exfoliation of MoS_2 91

5.6 Flexible MoS_2 photodetectors 92

5.6.1 Fabrication by mechanical lithography 92

5.6.2 Fabrication by photolithography 94

5.7 Conclusion 99

5.8 Author contributions 99

Chapter 6 Modifications of thin-film transistors by electrohydrodynamic printing 100

6.1 Introduction 100

6.2 Layout of TFTs from PragmatIC 102

6.3 Aims of chapter 103

6.4 Method and materials 104

6.4.1 Modification with APTES 104

6.4.2 Modification with the antibody 105

6.4.3 Preparation of cardiac troponin I protein 105

6.4.4 Fabrication of microfluidic channels 106

6.4.5 Electrical measurement of TFTs 106

6.4.6 Fluorescence microscope imaging 106

6.5 Characteristics of bare TFTs 107

6.6 Modification 110

6.6.1 Modification by APTES 110

6.6.2 Modification with the cTnI antibody 112

6.7 Integration with microfluidic channels 115

6.8 Device limitation for biosensing 117

6.9 Conclusions 119

6.10 Author contributions 121

Chapter 7 Conclusions and future work 122

7.1 Conclusions 122

7.2 Future work 124

Publications and Conferences 127

Reference 129

List of Figures

Figure 1-1 Novel applications enabled by flexible and wearable technology. a. The full-colour OLED display attached on the hand skin (adapted from [22]). b. The colourimetric biosensor for sweat monitoring attached on the arm (adapted from [23]). 4

Figure 2-1 Silk-based electronic devices biotransferred onto a. the skin and b. the tooth (adapted from [78]). 13

Figure 2-2 a. A pinwheel made of graphene/silk film (adapted from [85]). b. Silk-based thermoelectric generator attached to the arm to convert the body heat to voltage output (adapted from [82]). 14

Figure 2-3 *a.* A silk-based wavy waveguide (adapted from [89]). b**.** An image of a silk-based microlens arrays (adapted from [76]). 15

Figure 2-4 a. A AgNW wearable heater for thermotherapy (adapted from [95]). b. The S-shaped AgNW-cloth attached on the gloves to reflect heat back to the body (adapted from [96]). 17

Figure 2-5 a. A transparent stretchable strain sensor based on AgNW/PEDOT:PSS/PU (adapted from [56]). b. A smart strain sensor based on AgNPs which can recognise the facial expression (adapted from [99]). 19

Figure 2-6 a. The schematic of bending the heterstructure of graphene-WS_2 on the PEN substrate. b. Optical image of the heterstructure in which S1, S2 and S3 represent graphene, monolayer WS_2 and multilayer WS_2, respectively. c. Kelvin probe microscopy image of the highlighted area in b. Adapted from [102]. 20

Figure 2-7 a. The photograph of the FET with the heterostructure of MoS_2-graphene-hBN and the curve of field-effect mobility vs. strain (adapted from [104]). b. An all-2D FET with the heterostructure of WSe_2-hBN-graphene and its transfer characteristics (adapted from [105]). 21

Figure 2-8 a. A flexible and transparent GaSe photodetector (adapted from [110]). b. Time resolved curve of the photocurrent of GaSe photodetector when the light is switched on/off

under different bending radii (adapted from [110]). c. A flexible near-infrared photodetector based on $MoTe_2$ and graphene (adapted from [111]). d. Photoswitching behavior of the flexible $MoTe_2$/graphene photodetector after 5000 bending cycles (adapted from [111]) 22

Figure 2-9 a. Schematic process of writing patterns in PMMA-AuNPs using AFM lithography. b. SEM image of the line patterns indicating PMMA-AuNPs are removed by the tip. c. SEM image after the deposition of AuNPs with bigger size on the line-pattern area. Adapted from [121]. 25

Figure 2-10 a. Schematic process of using the tip to write nanostructures in the resist layer and transferring the pattern onto the substrate by the deposition of Au and the lift-off of the resist. b. Dark-field images of nanostructures. Adapted from [123]. 26

Figure 2-11 Problems of AFM lithography: a. Under-cutting. b. Over-cutting. 27

Figure 2-12 Drop-on-demand Inkjet printing process: a. piezoelectric mode. b. thermal mode. Adapted from [127] 28

Figure 2-13 a. Images and static contact angles of drops of water on the untreated paper and modified papers with different organosilanes. B. Optical images of printed silver lines on the untreated paper and modified papers. Adapted from [130]. 31

Figure 2-14 The structure of the ultrathin all-organic FET: a. Lateral view. b. Overview. Adapted from [136]. 32

Figure 2-15 a. Schematic of a typical EHD printing system (adapted from [153]). b. The formation of Taylor cone and the liquid jet ejection in EHD printing (adapted from [154]). ... 33

Figure 2-16 Different modes of EHD printing. Adapted from [157]. 35

Figure 2-17 Various optical free-form elements printed by DLW: a, b Free-form lens. c, d Free-form lens with high NA. e, f Beam expander. Adapted from [222]. 43

Figure 2-18 Schematic of nanoimprinting process: a. Thermal nanoimprinting. b. UV nanoimprinting. Adapted from [227]. 44

Figure 3-1 a. SEM image of a new Tap-300 G probe with the rotated tip. b. SEM image of the zoom-in view of the new tip. 50

Figure 3-2 Photograph of the EHD setup, including camera, XY stages, Z stage, Syringe pump, DC power supply, voltage amplifier and computer. 52

Figure 3-3 Optical images of the tips during printing of the same ink: a. A large droplet of ink accumulating near to the untreated tip. b. A smaller droplet of ink accumulating near to the PFDT treated tip..... 54

Figure 3-4 a. The photograph of the home-built probe station. b. The photograph of the semiconductor analyser. 58

Figure 3-5 a. Probe station with laser input. b. A 633 nm laser diode. c. Keithley source meter 2614B. 59

Figure 4-1 Schematic process flow of the fabrication process of water-based mechanical bilayer lithography..... 63

Figure 4-2 Structural formula of PVA..... 64

Figure 4-3 Investigation of mechanical forces that should be applied on the tip. a. AFM image of bilayer resist with a gap. b. Height profile of the dashed line 1 in a. c. AFM image of PVA with a gap. d. Height profile of the dashed line 2 in c. e. Schematic diagram of the AFM tip patterning. f. Force vs depth curve obtained by using gradually increasing mechanical forces and measuring the corresponding depth after patterning. 66

Figure 4-4 a. SEM image of a new tip. b. SEM image of a used tip. 68

Figure 4-5 Structural collapse of the bilayer occurs during the development in room-temperature water: a. for 9 s. b. for 4 s. c. for 2 s. 68

Figure 4-6 Comparison between proper development and improper development. a. Optical image of square patterns after improper development. Structural collapse occurred due to the development of unpatterned PVA. b. Optical image of square patterns after proper development. 69

Figure 4-7 Cross section of bilayer structure after development. a. SEM image of the cross section under lower magnification. b. SEM image of the cross section under higher magnification. c. SEM image of the pattern which shows the overhanging structure. 69

Figure 4-8 Optical images of an electrode pattern after key steps, including a. mechanical patterning of the bilayer resist, b. water-based development, c. metal deposition prior to lift-off, and d. metal electrode after lift-off. 71

Figure 4-9 High-resolution patterns on SiO_2/Si substrates fabricated by bilayer lithography. False-coloured SEM micrographs of a. line patterns, b. highest resolution line pattern, demonstrating an achievable line width of 310 nm, c. spacing of 471 nm between two patterns..... 72

Figure 4-10 Patterns with various shapes written by mechanical bilayer lithography. False-coloured SEM micrographs of a. a circular pattern, b. a triangular pattern, and c. a ring pattern. d. SEM image of nine square patterns. e. AFM scan of these square patterns. f. Height profile of the dashed line marked in e. 74

Figure 4-11 Square patterns on PET substrates at different stages of the fabrication process. a. AFM image of square patterns after patterning. b. Height profiles of the dashed lines in a. c. Optical image of square patterns after patterning. d. Optical image of square patterns after development in water. 75

Figure 4-12 Square patterns on PET substrates. a. A photo of a PET substrate with square patterns of Cr and Au. b. AFM scan of these square patterns on the PET substrate. c. Height profile of the dashed line marked in b. 76

Figure 5-1 Photographs of a. Bulk MoS_2 powder, b. MoS_2 dispersions before sonication, c. MoS_2 dispersion after sonication, d. MoS_2 dispersion after centrifuge. e. SEM image of MoS_2 dispersion before sonication. f. SEM image of exfoliated MoS_2. 87

Figure 5-2 a. UV-vis spectrum of exfoliated MoS_2 dispersions. b. Raman spectrum of exfoliated MoS_2 nanosheets. 88

Figure 5-3 Optical images of EHD printed lines at different velocities of the stage: a. 5 mm/s, b. 6 mm/s, c. 7 mm/s, d. 8 mm/s..... 89

Figure 5-4 a. AFM image of the printed MoS_2 nanosheets. Statistical analysis of three dimensions of printed nanosheets: b. width, c. length, d. thickness..... 90

Figure 5-5 Raman spectrum of printed MoS_2 91

Figure 5-6 MoS_2 thin film transferred onto the PET substrate. a. Optical image of MoS_2 thin film transferred on the PET substrate before patterning. b. Raman spectroscopy of MoS_2 thin film on the PET substrate. c. AFM image of MoS_2 thin film on the PET substrate. d. Height profile of the dashed line AB in c. 92

Figure 5-7 Flexible MoS_2 photodetector device. a. Schematic diagram of the flexible MoS_2 photodetector. b. Optical image of the flexible MoS_2 photodetector. c. I-V curve of the photodetector in the dark and under different illumination powers. d. Photocurrent of the photodetector under different illumination powers for V = 1 V. e. Photoresponsivity of the MoS_2 photodetector. f. Time-resolved photoresponse of the photodetector for V = 0.5 V and an illumination power of 38 μW. The calculated response time is 42 ms. 94

Figure 5-8 a. Optical image of the flexible MoS_2 photodetector fabricated by photolithography. b. AFM image of the flexible MoS_2 photodetector fabricated by photolithography. c. Height profile of the dashed line 1 in b. 95

Figure 5-9 A comparison of photoresponse of the MoS_2 photodetector fabricated by photolithography. a. I-V curve of the photodetector in dark and under different illumination powers. b. Photocurrent of the photodetector under different illumination powers for V = 1 V. c. Photoresponsivity of the MoS_2 photodetector. d. Time-resolved photoresponse of the photodetector for V = 0.5 V and an illumination power of 38 μW. The calculated response time is 348 ms. 96

Figure 6-1 Schematic of drop casting functionalisation. 101

Figure 6-2 Schematic of TFTs provided by PragmatIC. a. The top-view of the TFT array. b. The cross-section of each component layer of TFTs, including Si/SiO_2 substrate, the dielectric layer, the bottom gate electrode, IGZO semiconductor channel and source/drain electrodes. 103

Figure 6-3 a. Modification of the IGZO surface (red rectangular area) through on-demand EHD printing. b. the structure to be built by EHD printing on the IGZO surface, including APTES as the amino-silane linker and the antibody of cTnI. 104

Figure 6-4 The comparison of the transfer characteristic of the TFT between under illumination and under dark conditions. 107

Figure 6-5 Comparison of the transfer characteristic of the bare TFT measured by two methods: a. the symmetrical scanning approach. b. non-symmetrical scanning approach. 108

Figure 6-6 Comparison of the transfer characteristic of the TFT modified with APTES measured by two methods: a. the symmetrical scanning approach. b. non-symmetrical scanning approach. 109

Figure 6-7 a. The microscope image of a 50 µm × 5 µm TFT. b. The output characteristics of the TFT with V_g varied from 2 V to 4 V. c. The transfer characteristic of the TFT at the V_{ds} = 0.5 V. d. The $I_{ds}^{0.5}$- V_g curve at the V_{ds} = 0.5 V. 110

Figure 6-8 a. Schematic of the modification of IGZO surface with APTES molecules. b. N 1s XPS spectra of IGZO surface with or without the modification of APTES. 111

Figure 6-9 a. Optical image of the IGZO channel modified with APTES. b. Comparison of transfer curves of the TFT before and after printing APTES. 111

Figure 6-10 Fluorescence microscope image of the sample with the printed line of APTES. Before imaging, the sample was incubated with a mixture of nonflorescent cTnl antibody and a mixture of fluorescent secondary antibody (Goat anti-Rabbit IgG-Alexa 488) in sequence. 112

Figure 6-11 a. The EHD printing process of the improved cTnl antibody mixture into a continuous line. b. The printed dot of cTnl antibody which just covers the IGZO channel. 113

Figure 6-12 a. Modification and sensing procedures. b–f. The transfer characteristics of TFTs before/after modified with APTES and antibody mixture, as well as after sensing cTnl protein with different concentrations: b. 125 ng/mL, c. 500 ng/mL, d. 1 µg/mL, e. 50 ng/mL, f. 250 ng/mL. 114

Figure 6-13 a. Schematic of the microfluidic channel design. b. Schematic of the structure of a PDMS cell attaching on a TFT chip with enhanced adhesion by SS4120 primer. ... 116

Figure 6-14 a. Photograph of the PDMS cell adhered on the TFT chip. b. Optical images of the DI water flowing through the microfluidic channel..... 117
Figure 6-15 a–d. Optical images of the IGZO channel attached with the microfluidic channel while: a. no PBS is input. b. PBS is input. c. PBS is input and the completion of the first I_{ds} vs. V_g measurement. d. PBS is input and the completion of the second I_{ds} vs. V_g measurement. e–f. The I_{ds} vs. V_g curve under the fixed V_{ds} of 0.1 V: e. before PBS is input into the channel. f. after PBS is input into the channel. 119

List of Tables

Table 1-1 Total waste and hazardous waste of three lead companies in semiconductor industry 5

Table 2-1 Key properties of commonly used polymeric substrates 10

Table 2-2 Functional ink materials of EHD printing for flexible and wearable technologies 40

Table 2-3 Summary of current manufacturing techniques for flexible technologies[11,113,235] 48

Table 3-1 Details of each component in EHD printing setup 53

Table 5-1 The comparison of properties of two flexible MoS_2 photodetectors fabricated by photolithography and mechanical bilayer lithography 98

List of Abbreviations

2DMs: Two-dimensional materials

UV: Ultraviolet

PVA: Polyvinyl alcohol

PET: Polyethylene terephthalate

EHD printing: Electrohydrodynamic printing

TFTs: Thin-film transistors

APTES: (3-Aminopropyl)triethoxysilane

cTnl: Cardiac troponin I protein

LEDs: Light-emitting diodes

OLEDs: Organic light-emitting diodes

PDMS: Polydimethylsi-loxane

2D: Two-dimensional

PEN: Polyethylene naphthalate

PI: Polyimide

PEEK: Polyether ether ketone

PC: Polycarbonate

PS: Polystyrene

PES: Polyethersulphone

PEI: Polyethylenimine

PEDOT:PSS: Poly(3,4-ethylenedioxythiophene): poly(styrenesulfonate)

ITO: Indium tin oxide

OFETs: Oragnic field-effect transistors

NPs: Nanoparticles

NWs: Nanowires

NTs: Nanotubes

TMDs: Transition metal dichalcogenides

hBN: hexagonal boron nitride

SPL: Scanning probe lithography

STM: Scanning tunneling microscope

AFM: Atomic force microscope

PMMA: Poly(methyl methacrylate)

DOD: Drop-on-demand

Re: Reynolds number

We: Weber number

Oh: Ohnesorge number

DC: Direct

AC: Alternating current

DLW: Direct laser writing

3D: Three-dimensional

OLS: Optical lever sensitivity

PFDT: 1H,1H,2H,2H-perfluorodecanethiol

DMF: Dimethylformamide

SEM: Scanning probe microscopy

UV-vis: Ultraviolet-visible

XPS: X-ray photoelectron spectroscopy

PL: Photoluminescence

DMSO: Dimethyl sulfoxide

IPA: Isopropyl alcohol

IGZO: Indium gallium zinc oxide

EDC: N-(3-Dimethylaminopropyl)-N′-ethylcarbodiimide

NHS: N-Hydroxysuccinimide

PBS: Phosphate buffer solution

Chapter 1

Introduction

1.1 From nanotechnology to nanomanufacturing

Nanotechnology is a broad scientific and technological field where properties and performance of materials can be significantly tuned by manipulating their nanostructures for the purpose of industrial applications. The development of nanotechnology has significantly promoted new discoveries and inventions in next-generation electronic and photonic devices of the semiconductor industry such as nanoscale light-emitting diodes (LEDs)[1,2], thin-film transistors (TFTs)[3–5], high-efficiency batteries and solar cells[6,7], quantum computers[8], etc. Nanomanufacturing plays an important role in transforming nanoscale science into functional devices. Therefore, nanomanufacturing is the basis of nanotechnology.

Nanomanufacturing approaches are classified into two categories, including top-down and bottom-up methods. Top-down nanomanufacturing is a deterministic process in which the bulk material is processed into the desired nanoscale structure[9]. Top-down approaches (e.g. photolithography, electron-beam lithography, nanoimprinting and scanning probe lithography) usually involve using the resist layer where the desired pattern is written by ultraviolet (UV) light/X-rays, electron-beam, stamping moulds or nanoscale tips, followed by the development, etching/deposition and resist removal/lift-off processes[10]. The highest resolution of top-down approaches can reach sub-2 nm (electron-beam lithography)[11]. However, the use of resist generates the waste of materials, and the use of organic solvents as the developer and remover produces a large amount of hazardous chemical waste. Therefore, the disposal and recycle of the hazardous waste has become a serious issue and made these techniques less sustainable in the long term. In addition, some of these techniques (electron-beam lithography and photolithography) also require expensive

facilities, such as cleanroom, which makes themselves hardly affordable and accessible. In spite of this, most current integrated circuits still rely on the resist-based techniques due to their advantages of high resolution and quality.

Bottom-up nanomanufacturing (e.g. inkjet printing, dip-pen printing and electrohydrodynamic printing) is an additive process where materials and devices with complex structures are directly constructed from relatively smaller units (e.g. atoms, molecules and nanoparticles)[12]. Materials are selectively and rapidly deposited onto the specific position of the substrate, which reduces the waste of materials and fabrication cost. The fabrication equipment can be operated at room temperature and pressure, which saves the energy consumption and improves the accessibility. Therefore, bottom-up techniques are with higher sustainability. Inkjet printing as a typical bottom-up approach is a rapid prototyping manufacturing technique for features in or above microscale. By adding enough pressure within the liquid ink to overcome the surface tension, drops or jets are ejected from the nozzle[13]. A wide range of novel materials have been demonstrated to be suitable for inkjet printing, including two-dimensional materials (2DMs)[14,15], biomaterials[16], conductive polymer[17] and functional nanoparticles[18,19]. One limitation of inkjet printing is that its resolution is restricted by the nozzle size. To achieve a higher resolution, Electrohydrodynamic printing (EHD printing) can be a better option. The difference between inkjet printing and EHD printing is that EHD printing mainly uses high electric potential between the nozzle and the substrate to pull the ink out. The high electrical voltage causes the formation of the Taylor cone at the tip of the nozzle[20]. With the further increasing voltage, the Taylor cone stabilises and a jet is ejected to the substrate[21]. In this case, EHD printing is able to write much finer patterns than the nozzle size. However, overall there is still much space to improve these techniques for the purpose of manufacturing nanoscale devices due to their slightly lower resolution at the microscale for most cases and less precision to position patterns compared to top-down techniques.

The top-down and bottom-up techniques are developed not to compete but complement with each other. The use of both types of techniques can build electronic and photonic devices with more functionalities and higher quality.

1.2 Sustainable nanomanufacturing for flexible technologies

With the development of wearable and flexible technologies, a wide range of novel applications have been implemented in electronics and photonics including organic light-emitting diodes (OLEDs), curved displays, foldable touchscreens, wearable sensors, and so on. For example, Choi *et al.* have presented a wearable full-colour OLED display integrated with the two-dimensional (2D) material of MoS_2[22]. The integration with MoS_2 which has atomic thickness and outstanding electrical properties enables the stable current level while the OLED is shrunk/stretched on the skin (**Figure 1-1**a). Koh *et al.* have proposed a wearable colourimetric biosensor based on a soft microfluidic system for sweat monitoring[23]. The flexible polydimethylsiloxane (PDMS) microfluidic system can be attached on the skin to collect sweat and quantitatively analyse the pH, glucose, lactate and chloride of the sweat, which gives a simple way to monitor health in real time (**Figure 1-1**b).

Flexible substrates have been regarded as a promising replacement for silicon substrates. There are three types of flexible substrates, including thin glasses, polymers and metal foils. Compared to rigid substrates, flexible substrates have several advantages of conformability, flexibility, light weight, good transmittance and low cost[24]. Therefore, it is highly promising to seamlessly integrate flexible devices with wearing clothes and accessories. However, the construction of functional devices on flexible substrates is a big challenge, especially at the nanoscale. As most flexible substrates have drawbacks of low chemical resistance, poor processability, higher roughness and lower mechanical stability, most conventional top-down nanomanufacturing approaches such as electron beam lithography and photolithography are not suitable for sensitive flexible substrates[25]. Compared to the top-down approaches, bottom-up nanomanufacturing approaches are more compatible with

flexible substrates but still lack higher resolution. To build nanoscale functional devices on sensitive flexible substrates, the current fabrication technique mainly relies on the transfer printing[26]. The nanoscale/microscale structure is firstly fabricated on a rigid substrate by electron-beam lithography or photolithography, and then transferred onto the flexible substrate by a specific stamp such as PDMS or shape memory polymer[26]. This complex process requires additional cost and time/energy compared to conventional fabrication process on rigid substrates. Therefore, it is essential to develop new cost-effective and sustainable nanomanufacturing techniques particularly for sensitive flexible substrates.

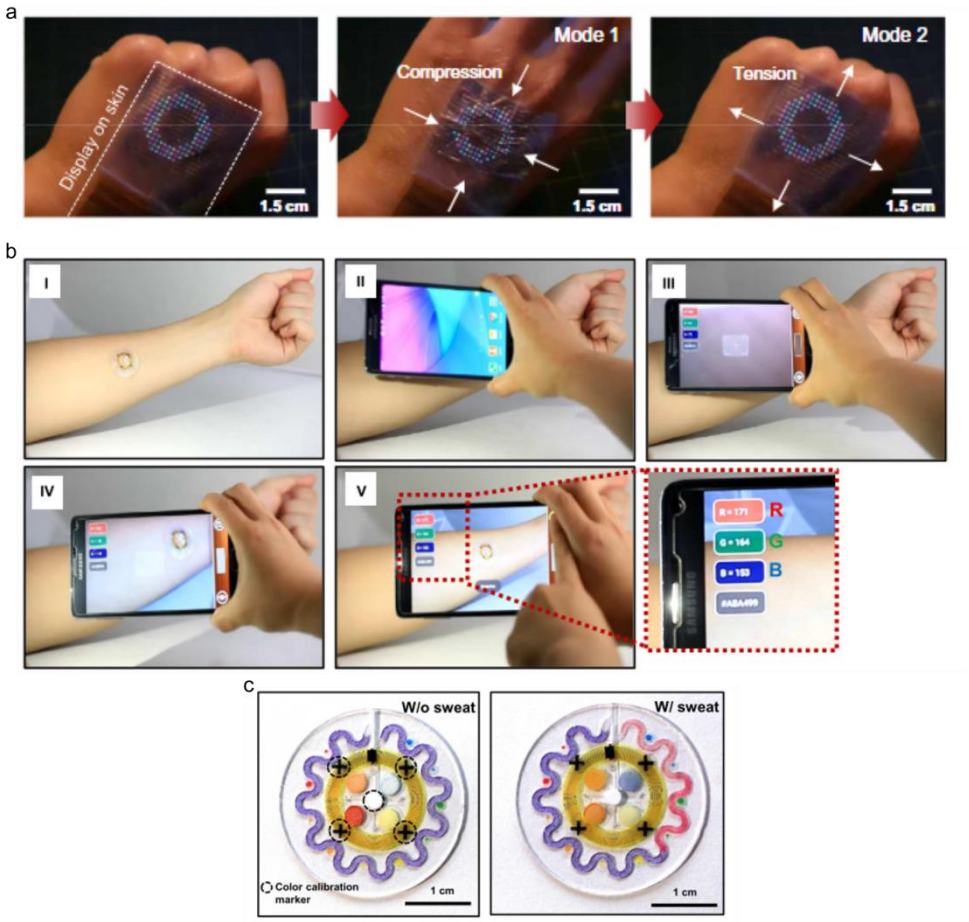


Figure 1-1 Novel applications enabled by flexible and wearable technology. a. The full-colour OLED display attached on the hand skin (adapted from [22]). b. The colourimetric biosensor for sweat monitoring attached on the arm (adapted from [23]).

The sustainability and cost-effectivity of newly developed nanomanufacturing techniques should be highlighted. **Table 1-1** summarise the yearly weight of total waste and hazardous waste outsourced by three lead companies in the semiconductor industry in 2020 and 2021.

Among them, it can be noted that the weight of hazardous waste accounts for nearly 50% of the weight of total waste in TSMC in 2020 and 2021. According to 2020 TSMC Corporate Responsibility Report, 1.01 kg of waste is produced to fabricate a 12-inch equivalent wafer mask layer. Compared with non-hazardous waste, the disposal and recycle of hazardous waste is more difficult and consumes more cost and energy, as harmful waste requires additional and professional treatment before disposing or reusing them[27,28]. Even with the proper disposal, it still poses a great threat to the living environment such as water and soil contaminations. Thus, the development of a technique for flexible devices should not only consider the resolution, scalability, cost and sensitivity of flexible materials, but also minimise the harm to the environment.

Table 1-1 Total waste and hazardous waste of three lead companies in semiconductor industry

	ASML[1]	TSMC[2]	Apple[3]
2020 Total Waste (Tons)	5,257	550,275	50,390.64
2020 Hazardous Waste (Tons)	372	280,635	2,026.89
2021 Total Waste (Tons)	5,878	645,832	57,860.05
2021 Hazardous Waste (Tons)	411.46	319,763	1,762.92

[1] ASML: Advanced Semiconductor Materials Lithography. Data are from 2020/2021 ASML Annual Report.

[2] TSMC: Taiwan Semiconductor Manufacturing Company. Data are from 2020 TSMC Corporate Responsibility Report & 2021 TSMC Sustainability Report.

[3] Data are from 2022 Apple Environmental Social Governance Report.

1.3 Thesis outline

The aim of this thesis is to develop new sustainable and cost-effective nanomanufacturing approaches and seek more possibilities in integrating existing low-cost nanomanufacturing techniques with sensitive flexible materials. This is to provide more accessible and environmentally-friendly ways to build advanced flexible electronic and photonic devices. After briefly discussing the advantages/disadvantages of current nanomanufacturing

techniques and highlighting the importance of nanomanufacturing for wearable and flexible technologies in the first chapter, the rest of the thesis will seek to:

- Discuss the state-of-the-art materials and nanomanufacturing techniques for building functional devices on flexible substrates. (Chapter 2)
- Introduce the details of methodology and metrology used in the thesis. (Chapter 3)
- Propose a nanoscale mechanical bilayer lithography which uses water as the developer and remover, which enhances the sustainability. (Chapter 4)
- Demonstrate the application of the water-based mechanical bilayer lithography in photonics by fabricating a flexible MoS_2 photodetector. (Chapter 5)
- Demonstrate the localised functionalisation of thin film transistors using electrohydrodynamic printing for biosensing cardiac troponin I protein. (Chapter 6)

The final chapter summaries the conclusions and present the future work that is meaningful to do based on this thesis.

1.4 Key contributions

This thesis highlights the importance of sustainability in the proposal of novel nanomanufacturing techniques for flexible technologies. The sustainability is enhanced by minimising the use of hazardous chemicals in the fabrication process of proposed techniques. Meanwhile, the functionality and compatibility to sensitive materials in proposed techniques are also described. The key contributions are listed as follows:

- The demonstration of the sustainable mechanical bilayer lithography that uses water as the developer and remover. This technique is suitable for patterning on both rigid and soft substrates.
- The ability of the water-based mechanical bilayer lithography to write arbitrary patterns and achieve resolution down to 310 nm.
- The applicability of water-based mechanical bilayer lithography to fabricate a flexible MoS_2 photodetector with the rapid response time down to 42 ms.

- The printability of the antibody of cardiac troponin I protein in EHD printing. This indicates the good compatibility of EHD printing with sensitive biomolecules.
- The demonstration of the on-demand localised functionalisation of TFTs by EHD printing of APTES and the antibody of cardiac troponin I protein on the selected semiconductor channels in an array of TFTs. This enables the functionalised TFT to show a response to the presence of cardiac troponin I protein.

Chapter 2

Nanomanufacturing of flexible devices: state of the art

Conventional nanomanufacturing techniques are mainly based on rigid substrates such as silicon chips. Photolithography and electron-beam lithography are two typical approaches used to manufacture silicon integrated circuits due to their ultra-high resolution. However, these techniques which use organic solvents in large volumes during the fabrication process are not compatible with flexible substrates which have low chemical resistance and poor mechanical stability. As a result, alternative nanomanufacturing techniques for flexible devices have been developed in consideration of the materials properties and poorer processability.

In this chapter, I will discuss the state-of-the-art materials and nanomanufacturing techniques that have been employed in flexible devices.

2.1 Materials for flexible devices

The most important advantage of flexible electronic and photonic devices over their rigid counterparts is the flexibility which enables their conformability with curved surfaces such as clothes, skin and banknotes. Materials to be used for flexible devices must satisfy the flexible characteristic so that these devices can be stretched, compressed or bended into complex geometries without significantly compromising their performance. Materials with a smaller thickness is therefore usually preferred. Based on the flexible characteristic, there are mainly three types of materials which are frequently used for flexible devices. In this section, the key properties, applications and manufacturing approaches of the three types of materials will be elaborated by discussing the typical examples in each category.

2.1.1 Polymers

Traditional rigid wafers have restricted electronic and photonic applications because of the intrinsic brittleness and the lack of optical transparency. These drawbacks make rigid wafers difficult to interface with soft curvilinear morphology. In comparison, a variety of polymers have been widely used as the substrates for flexible electronic and photonic devices such as thin-film transistors[29,30], wearable health-monitoring sensors[31,32], foldable displays[33,34], and solar cells[35,36] due to their advantages of excellent mechanical flexibility and conformability, light weight, high optical clarity and low cost. However, to replace the rigid substrates, there are additional strict requirements for polymeric substrates to fulfil[24,37]:

1. A good solvent resistance as the patterning of complex micro/nanoscale structures on polymeric substrates always uses hazardous organic solvents or alkaline solutions.
2. Stubborn dimensional stability under various conditions such as harsh solvent environment, high temperature and repeating bending/stretching/compressing.
3. Suitable thermal stability which requires the polymer chain not to deform or degrade under the processing temperature.
4. A low water/gas permeability to minimise the influence of humidity/air on the performance of functional devices.

Depending on various applications, it may also have other particular requirements of dielectric properties, optical transmission in the visible spectrum range, reflective index and specific mechanical parameters (e.g. Young's modulus and flexural modulus). **Table 2-1** lists the key properties of commonly used polymeric substrates. Compared to other polymeric substrates listed in **Table 2-1**, the overall properties of polyethylene terephthalate (PET) and polyethylene naphthalate (PEN) are relatively better balanced, especially the high optical clarity, good solvent resistance and dimensional stability. However, they are not so thermally stable because of their relatively low glass transition temperature. Polyimide (PI) is also a class of high-performance polymers because it possesses the

highest glass transition temperature and good solvent resistance, but its thermal/dimensional stability needs to be further improved. Although most properties of polyetheretherketone (PEEK) are excellent, it is not optically transparent. Therefore, it is more suitable for the applications without optical requirement.

Another essential polymer is polydimethylsiloxane (PDMS) that has been frequently used in flexible devices. Due to its good flexibility, chemical resistance and dimensional stability, it has been widely employed as the flexible substrate. Also, its optical transparency and biocompatibility enable PDMS another important application in microfluidics. PDMS is the most commonly used material in the fabrication of the microfluidic system, which promotes the development of DNA sequencing, drug delivery and point-of-care biosensing for clinical diagnostics[38]. The use of microfluidic channel reduces the required volume of analytes, which reduces materials and energy consumption as well as the waste and cost of chemical and biological process.The microfluidic channel acts as the interface between the biomolecules and the functional devices so that the lab-on-chip devices become achievable. The flexibility of PDMS enables the wearability of functional devices instead of carrying bulky equipment, leading to a convenient and efficient way to monitor health. In addition, PDMS is a popular material for designing flexible and optical waveguide due to its refractive index and easy mouldability into various shapes[39].

However, the comparison of **Table 2-1** is just within polymers. The chemical resistance, dimensional stability and thermal stability of polymeric substrates are still not comparable with rigid substrates. The sensitivity of polymeric substrates to hazardous chemicals, heat and UV light brings a processing challenge, as the conventional nanomanufacturing techniques using organic solvents/acid/alkaline, electron beam or UV are not suitable for them[25]. The softness and poor dimensional stability make it difficult to handle polymeric substrates during the fabrication process[40].

Table 2-1 Key properties of commonly used polymeric substrates

Polymer materials	T_g (℃)	T_m (℃)	Optical clarity (%)	Young's modulus (GPa)	Flexural modulus (GPa)	Water absorption (%)	Solvent resistance[1]	Dimensional stability	Reference
Polyethylene terephthalate (PET)	67–81	267	90	1.7	2	0.5	Good	Good	24,41–44
Polydimethylsiloxane (PDMS)	−123	−47	75–92	3.6×10^{-4}–8.7×10^{-4}	-	-	Good	Good	41,45–48
Polycarbonate (PC)	150	-	92	2.38	2.34	0.25	Poor	Fair	24,41,42
Polystyrene (PS)	100	240	89	3.2–3.4	3.1	1.4	Poor	Fair	24,41,42
Polyimide (PI)	>300	-	30–86	2.5	3.1	0.24	Good	Fair	24,41,42
Polyethylene naphthalate (PEN)	117	265	88	2	2.5	0.4	Good	Good	41,42,44
Polyether ether ketone (PEEK)	145	340	-	3.56	3.7	0.15	Good	Good	41,49
Polyethersulphone (PES)	220	-	85	2.41	2.55	0.43	Poor	Good	24,50
Polyethylenimine (PEI)	215	-	80	3.3–3.6	3.5	0.25	Fair	Good	49,51

[1] Soluble or swell in common ketone, alcohols esters hydrocarbon, acid and alkali solvents.

In addition to non-conductive polymeric substrates, conductive polymers are also widely used in the flexible technology. Recently poly(3,4-ethylenedioxythiophene): poly(styrenesulfonate) (PEDOT:PSS) has attracted much attention in various research fields because of its capabilities for applications as the flexible transparent electrodes[52,53], electroactive layers[54], active sensing layers[55,56], interconnectors/charge transport layers[57,58], etc. The conductivity of PEDOT:PSS can be adjusted by varying the ratio of PEDOT to PSS[59]. By doping PEDOT:PSS with polar solvents[60,61], acids[62,63] and ionic liquids[57,64], its conductivity can be significantly enhanced by 2–3 orders of magnitude[65]. Combining the high conductivity with the high transparency, PEDOT:PSS has been regarded as an alternative to indium tin oxide (ITO) electrodes. The advantage of PEDOT:PSS over ITO is its low fabrication cost and exceptional mechanical flexibility to conform with soft substrates. Therefore, it has been extensively used in applications of organic solar cells[66], OLEDs[67] and organic field-effect transistors (OFETs)[68]. In addition, its biocompatibility and conformability enable itself to be used as clinical electrodes for recording neural activities. Ganji *et al.* have demonstrated that a high-density PEDOT:PSS microelectrode array is safe to be implanted on the brain gyrus and is capable of measuring the differential neural modulation under different clinically relevant conditions with high signal-to-noise ratios[69]. There are also other conductive polymers including poluacetylene, polythiophene, polyaniline, polyphenylene and polypyrrole. Owing to their biocompatibility and conductivity, they all have a wide range of sensing, neural and biomedical applications[70,71].

In summary, there is a vast collection of functional polymers developed over the years so that researchers can browse for their demands. Polymers are promising materials for flexible technologies not only due to their mechanical flexibility to integrate with the complex geometry, but also because of their superb optical and electrical functionalities such as the high transparency, dielectric parameters, reflective index and electrical conductivity. The biocompatibility of polymers is also a crucial material property for

biomedical and healthcare applications. However, their relatively poor chemical resistance and thermal/dimensional stability make the fabrication of flexible devices at the nanoscale challenging. Thus, it is necessary to develop efficient manufacturing techniques that are compatible with polymers.

2.1.2 Biopolymers

Biopolymers can be classified into two groups including natural biopolymers and synthetic biopolymers[72]. Natural biopolymers are derived from plants or animals such as silk, cellulose and gelatin, while synthetic biopolymers are prepared using a variety of complex chemical/biochemical processing methods such as biopolymers of polyactic acid, polydopamine and polyhydroxyalkanoate[73].

Biopolymers have advantages of lightweight, non-toxicity, mechanical flexibility, biocompatibility and biodegradability[74]. Compared with many polymers that are difficult to degrade and dispose, the use of biodegradable biopolymers that can be disposed in the form of microbial degradation in flexible electronics and photonics is more sustainable and eco-friendly as the disposal of them brings no harm to the environment[75]. The mechanical flexibility of biopolymers highly satisfies the basic requirement of flexible technology. To further make biopolymers great candidates in electronic and photonic applications, the structure and composition of biopolymers can be altered via chemical modification to achieve the desired electrical properties (e.g. conductivity) or optical properties (e.g. refractive index). Due to their excellent biocompatibility, the use of biopolymers makes implantable medical devices more acceptable by the human body.

Silk fibroin as a typical biopolymer is extracted by removing the sericin during the degumming of the silk[74]. Silk fibroin possess outstanding mechanical properties (e.g. high toughness, tensile strength and stiffness), water-solubility, intrinsic biocompatibility and tunable biodegradability[76,77]. Silk fibroin can be fabricated into various forms of fibres,

textiles and films. These advantages give silk fibroin a great variety of applications in flexible technologies.

Silk fibroin acts as both passive and active components in flexible electronic devices. Due to the robust mechanical properties and insulating behaviour, silk fibroin has been used as the passive component of the substrate or the encapsulating material for flexible electronics. The excellent biocompatibility and tunable biodegradability make it feasible to use silk-based flexible electronic devices to be implanted onto the surfaces of organs such as skin, brains and enamels[78,79] (**Figure 2-1**). With the biodegradation of the silk fibroin substrate or package, the functional components can be transferred onto the organs without sign of inflammation[80].

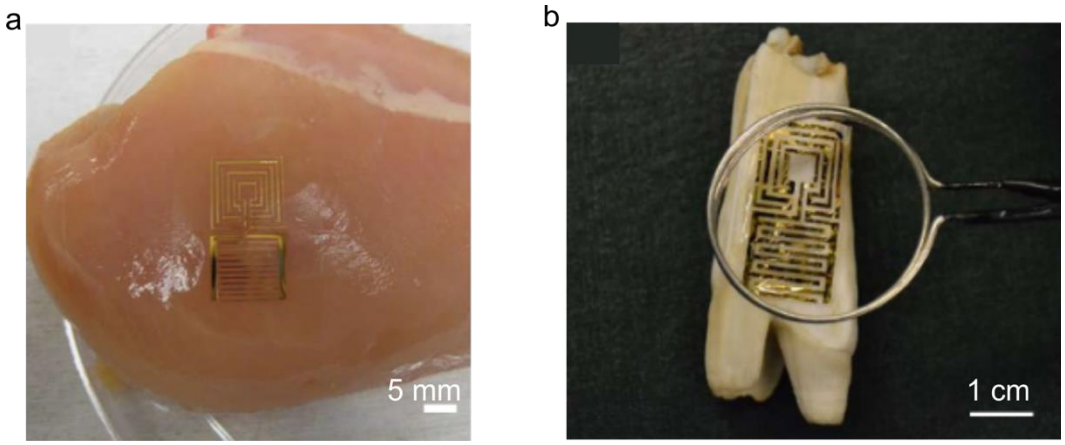


Figure 2-1 Silk-based electronic devices biotransferred onto a. the skin and b. the tooth (adapted from [78]).

To make silk fibroin a smart material, researchers have made significant advancement in combining silk fibroin with other functional materials to make the hybrid structure conductive and capable of strain sensing, energy harvesting and energy storing[81–84]. For instance, Liang *et al.* have demonstrated that coating graphene oxide (GO) onto silk fibres followed by the reduction of GO into graphene can make the insulating silk fibroin electrically conductive[85](**Figure 2-2**a). Lu *et al.* have proved the creation of a wearable thermoelectric generator by combining a silk fabric with Bi_2Te_3 and Sb_2Te_3[82]. The

generator can be attached to the arm skin to harvest the thermal energy from the person and generate a voltage output of 6.02 mV (**Figure 2-2**b).

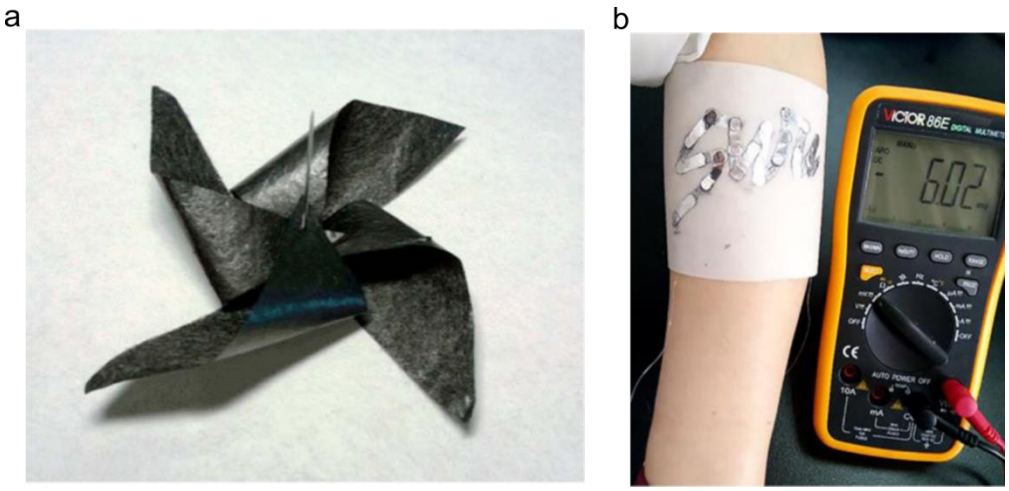


Figure 2-2 a. A pinwheel made of graphene/silk film (adapted from [85]). b. Silk-based thermoelectric generator attached to the arm to convert the body heat to voltage output (adapted from [82]).

Regarding being the active component in flexible electronics, silk fibroin is a promising dielectric material for OFET due to its dielectric properties. Wang *et al.* have demonstrated that choosing the thin film of silk fibroin as the dielectric layer can significantly enhance the operating speed of pentacene OTFTs with the high mobility of 23.2 $cm^2 V^{-1} s^{-1}$, while the pentacene OTFTs with SiO_2 as the dielectric layer only shows a low mobility of 0.22 $cm^2 V^{-1} s^{-1}$ [86]. Owing to the high optical transparency, robustness, good flexibility and light weight, silk fibroin has also been used as the insulating resistive-switching layer in resistive-switching memory devices[87,88].

In addition to the applications in flexible electronics, silk fibroin has also been used in flexible photonics due to its great optical and mechanical properties. The refractive index of silk is about 1.55 at the wavelength of 1.55 μm which is higher than the index of most polymers[39]. Thus, silk can be used as the core material in optical waveguides. Parker *et al.* have demonstrated the direct printing of both the straight and wavy silk waveguides using aqueous solution of silk fibroin as the ink[89] (**Figure 2-3**a). The printed waveguide is able to guide light at the wavelength of 633 nm. By adding a laser dye of Rhodamine

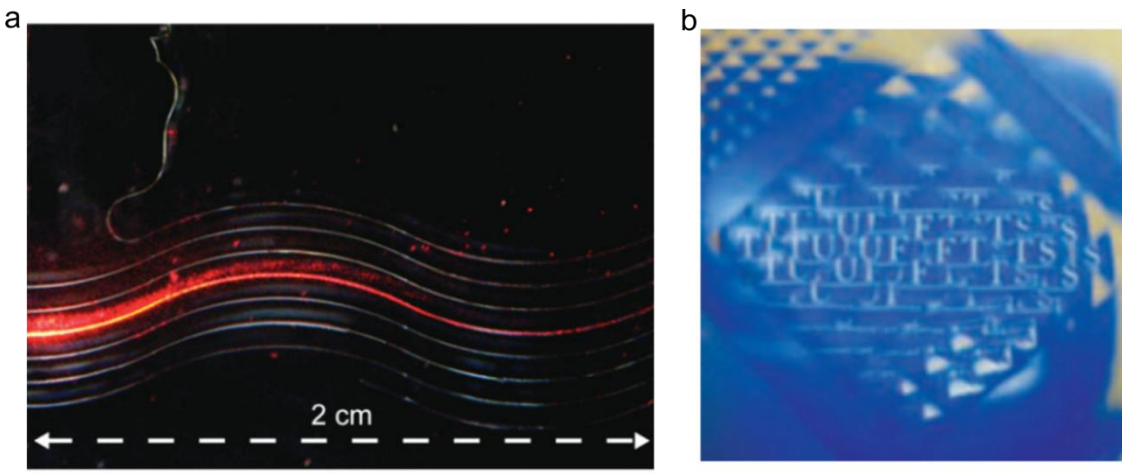


Figure 2-3 *a.* A silk-based wavy waveguide (adapted from [89]). b**.** An image of a silk-based microlens arrays (adapted from [76]).

6G into silk fibroin ink, the laser light of 532 nm wavelength is coupled into the doped silk waveguide, which is consistent with the absorption spectrum of the dye. This indicates that the silk fibroin ink can be functionalised by dopants to achieve various photoactivation of the waveguide. There are also other silk-based photonic structures, including microlens arrays (**Figure 2-3**b), diffractive optical elements, microprism arrays, photonic lattices and Fresnel lens[76,90].

As silk fibroin is soluble in water, the fabrication of silk-based flexible devices is mainly based on the aqueous silk fibroin solution. Silk fibroin films can be fabricated by drop casting, spin-coating, dip-coating and layer-by-layer assembly[91]. To further build nanoscale structures on silk fibroin films without damaging the film, transfer printing is applied as the main manufacturing technique which uses PDMS stamps to transfer the pre-fabricated structure on the rigid substrate onto the silk fibroin film[92]. The fabrication of silk-based electronic devices at or above the microscale mainly depends on spin-coating, soft-lithography, nanoimprinting, inkjet printing, stenciling and contact printing[90], among which most of these techniques utilises aqueous silk fibroin solutions and involve less hazardous chemicals.

The fabrication strategies of other biopolymers-based electronic and photonic devices are similar to those of silk fibroin. Biopolymers are likely to degrade under the strong

radiation, thermal treatment and chemical corrosion[93]. Conventional photolithography techniques are not suitable for manufacturing these devices in case biopolymers are dissolved or deformed by organic solvents and radiations of the strong energy electron-beam or photons [94]. Biopolymers are usually dissoluble in water, acid or organic solvents. Therefore, the manufacturing of such flexible devices based on biopolymers mainly relies on additive solution-based approaches such as screen printing and inkjet printing. The additive manufacturing techniques are low-cost and scalable but lack high resolution. To achieve nanoscale features, transfer printing is a solution but has low throughput and involves complex fabrication processes. In consideration of the instability of biopolymers during the manufacturing process, the fabrication techniques for biopolymer-based electronic and photonic devices still need to be improved to achieve high resolution while maintaining low cost and scalability.

2.1.3 Nanomaterials

Nanomaterials including one-dimensional and 2D materials have the prominent benefit of nanoscale dimensions to perfectly integrate with soft or curved surfaces. There are a wide range of nanomaterials including nanoparticles (NPs), nanowires (NWs), nanotubes (NTs), graphene, transition metal dichalcogenides (TMDs), hexagonal boron nitride (hBN), etc. These materials attract much attention not only because of their dimensional characteristic but also due to their excellent electrical and optical properties. Quantum effects in nanomaterials enable them to exhibit phenomenal electrical and optical properties compared to their bulk counterparts. The high surface to volume ratio of nanomaterials leads to a higher reactivity, which opens more opportunities for creating high-sensitivity chemical sensors and biosensors. Nanomaterials usually serve as the active components in flexible electronics and photonics. Nanoscale dimensions enable that their electrical and optical properties can be well maintained during the deformation of stretching, compressing and bending. The whole functional device can be thinned down to achieve the goal of the miniaturization of electronics and photonics.

Many polymeric substrates exhibit excellent mechanical flexibility but insufficient electrical conductivity and corrosive resistance. Conductive NPs and NWs are a solution to enhancing the stability and electrical properties of polymeric substrates[97]. Conductive NPs and NWs such as Au, Ag and Cu can be dispersed in aqueous or organic solvents. Therefore, it is feasible to deposit the solution-based NPs and NWs on flexible substrates by assembly, drop casting, spin coating, dip coating and printing.

Flexible and wearable actuators and sensors are two main applications of NPs and NWs. The applications of flexible actuators include thermal management and therapy, artificial muscles and drug delivery[98]. Hsu *et al.* have reported that the dip-coated AgNW-cloth is

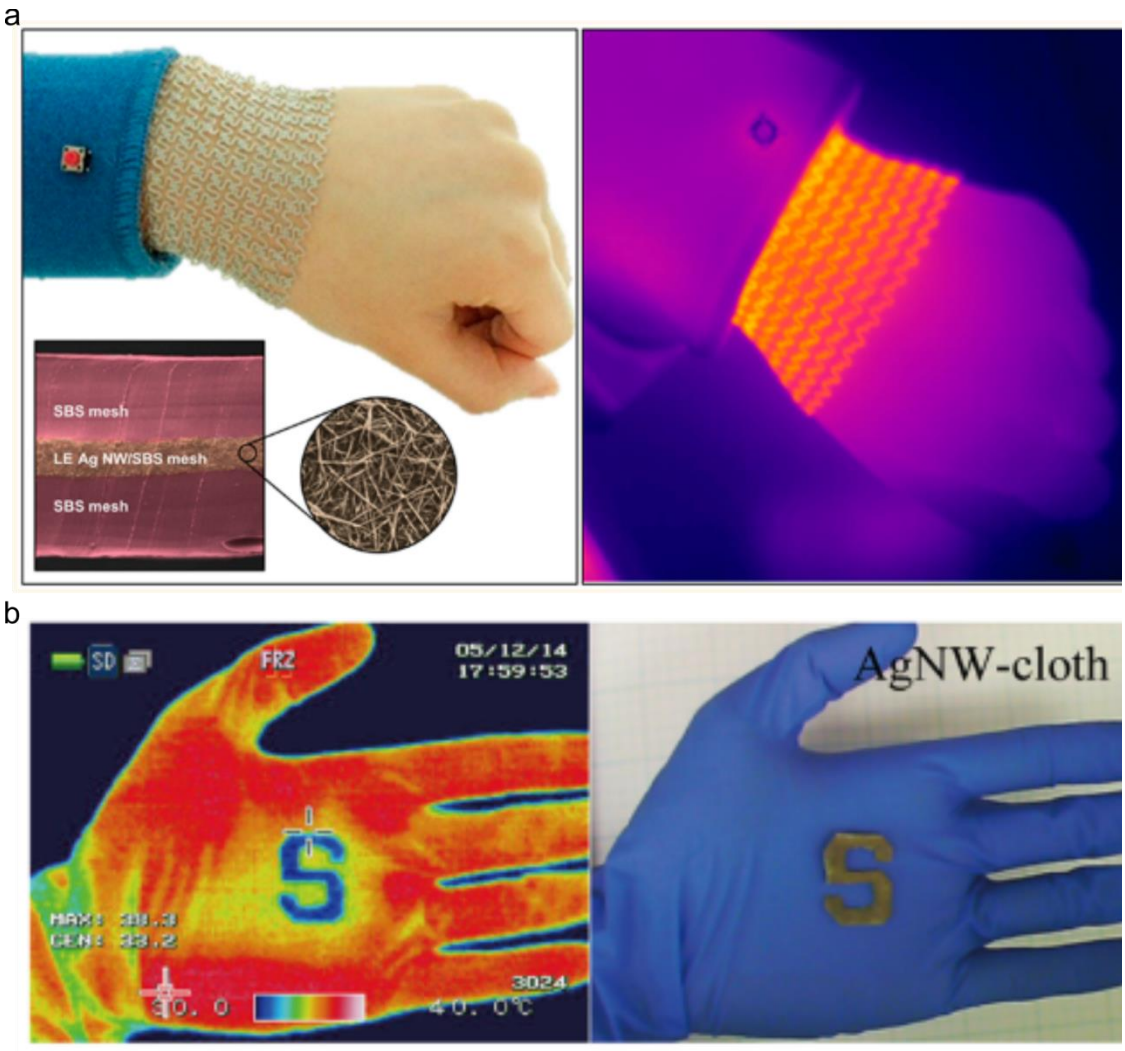


Figure 2-4 a. A AgNW wearable heater for thermotherapy (adapted from [95]). b. The S-shaped AgNW-cloth attached on the gloves to reflect heat back to the body (adapted from [96]).

able to reduce the heat loss of the human body by reflecting the body heat back to the body, which effectively keeps the thermal comfort of the body[95] (**Figure 2-4**b). The spacing between NWs is controlled to be smaller than the wavelength of infrared radiation from the body but much larger than the dimension of a water molecule. In this case, the human body can be kept warm and meanwhile feel comfortable wearing the cloth. Thermal therapy is an important treatment for many diseases. Choi *et al.* have developed a soft and wearable heater by using the nanocomposite of AgNWs and thermoplastic elastomer for thermotherapy[96]. This lightweight heater can be worn on the wrist or the knee to transfer heat to muscles and blood vessels, which offers a convenient and comfortable thermal treatment compared to the conventional heavy and rigid heaters (**Figure 2-4**a).

There are various types of wearable sensors based on NPs and NWs including strain sensors, pressure sensors and temperature sensors which can be worn to detect the human movements and monitor health[98]. Owing to the high surface-to-volume ratio as well as excellent mechanical and electrical properties of NPs and NWs, such sensors can be made of only a small quantity of materials but exhibit outstanding sensitivity and stretchability simultaneously. The wearability of such sensors makes the sensing process more convenient and effective. For example, Hwang *et al.* have demonstrated that a transparent stretchable strain sensor consisting of AgNW/PEDOT:PSS/PU nanocomposite can be attached on the human skin at various locations to recognize the strain change with high sensitivity[56]. The sensor is an integrated system including a supercapacitor and a triboelectric nanogenerator which are based on the same material composition (**Figure 2-5**a). This enables a self-powered sensing platform to monitor different human activities. A similar smart strain sensor based on AgNPs which can be attached on the facial skin to recognize facial expressions has also been reported by Su and co-workers[99] (**Figure 2-5**b).

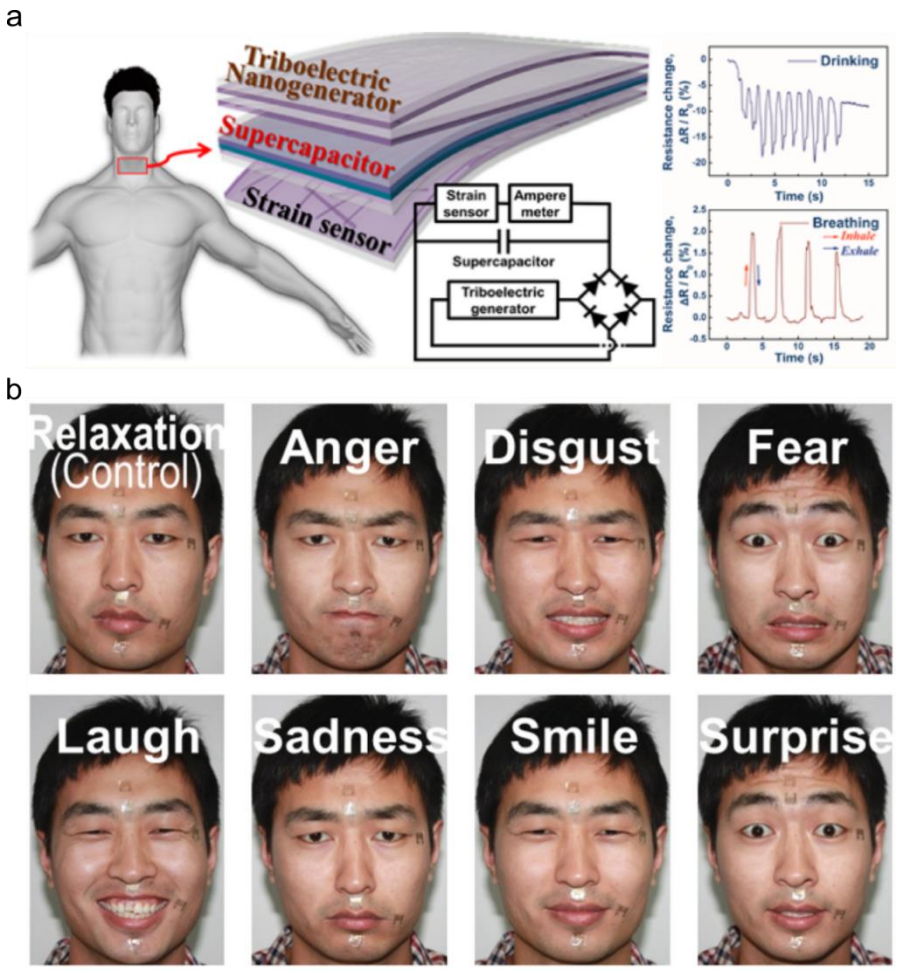


Figure 2-5 a. A transparent stretchable strain sensor based on AgNW/PEDOT:PSS/PU (adapted from [56]). b. A smart strain sensor based on AgNPs which can recognise the facial expression (adapted from [99]).

In addition to NPs and NWs, 2DMs also have a wide range of applications in wearable and flexible technologies. 2DMs are a big family consisting of metals, semiconductors and insulators. 2DMs can be obtained by mechanically exfoliating the bulk crystal to the monolayer or few-layer material. This is a simple and low-cost method but the exfoliated flake size is quite small. Alternatively, chemical vapour deposition is the solution to obtaining large-area thin-films of 2DMs. Depending on the thickness, the semiconducting 2DMs such as MoS_2 and WS_2 possess tunable bandgap[100]. When these semiconductors are thinned down to monolayer, their indirect bandgap transits to direct bandgap, showing a strong photoluminescence. Therefore, they have superior electrical and optical properties. Compared to conventional bulk semiconductors, 2D semiconductors

have excellent mechanical properties and optical transparency. Thus, 2DMs have the pronounced advantage of mechanical flexibility to be conformal on flexible substrates[101].

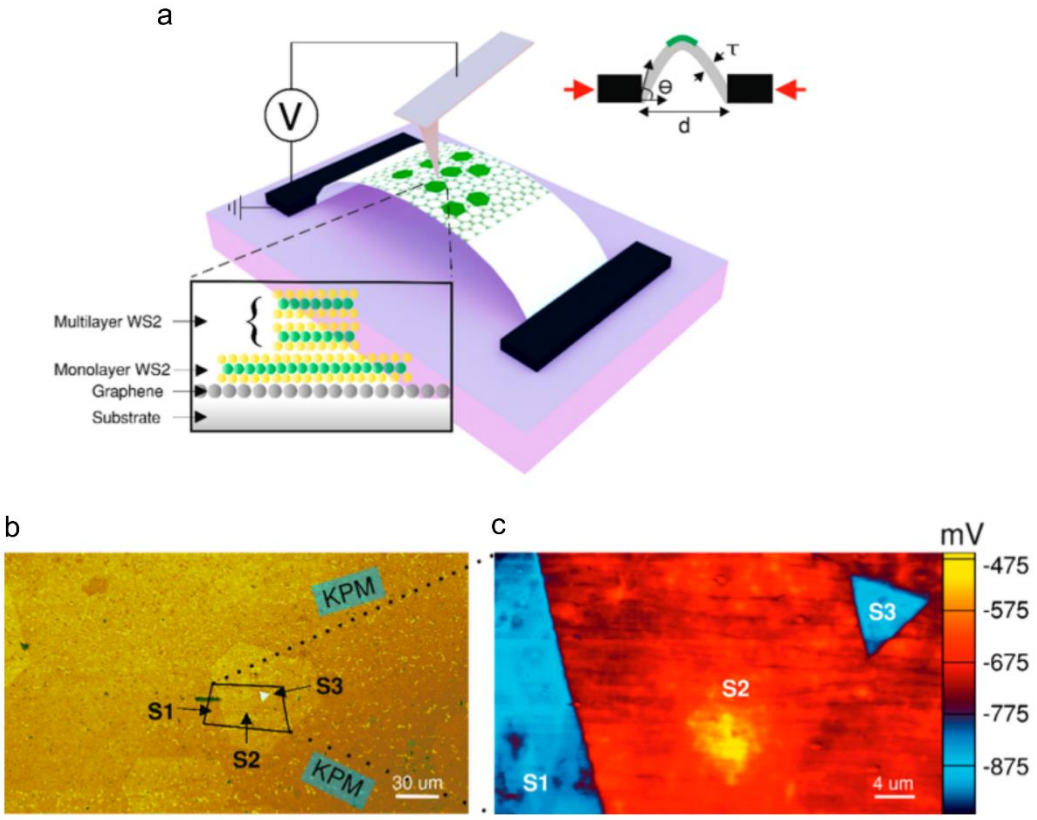


Figure 2-6 a. The schematic of bending the heterstructure of graphene-WS_2 on the PEN substrate. b. Optical image of the heterstructure in which S1, S2 and S3 represent graphene, monolayer WS_2 and multilayer WS_2, respectively. c. Kelvin probe microscopy image of the highlighted area in b. Adapted from [102].

During the mechanical stretching/bending of 2DMs, the induced local strain may lead to the change in electrical and optical properties[103]. Sarwat *et al.* have reported the effect of uniaxial tensile strain on the work function of the heterostructure of graphene-WS_2[102]. The strain is applied through bending the PEN substrate with the heterostructure, and the corresponding work function is characterised by Kelvin probe microscopy under different strain values (**Figure 2-6**). With the increasing strain, there is an increase of work function of graphene and WS_2 due to the decrease of the Fermi Level[102]. Therefore, it is important to understand the strain-induced effect while integrating 2DMs with flexible substrates.

With the advantages of sizable bandgap, optical transparency, high mechanical strength as well as good electrical properties, 2DMs have been extensively used to fabricate flexible transistors[106,107]. Lee *et al.* have demonstrated a flexible and transparent FET using MoS_2 as the semiconducting channel, hBN as the dielectric layer and graphene as the gate electrode[104]. The use of 2D hBN rather than conventional dielectrics such as SiO_2 greatly enhances the field-effect mobility. The hysteresis effect is also eliminated, indicating an obvious reduction of charge traps at the interface between MoS_2-graphene-hBN. By applying 1.5% strain on this 2DMs-based FET, it shows stable performance due to the excellent flexibility of 2DMs (**Figure 2-7**a). Similarly, all 2D, flexible and transparent FETs with the heterostructure of WSe_2-hBN-graphene have also been demonstrated by Das and co-workers[105] (**Figure 2-7**b). The device with the 2DMs-based heterostructure shows a fast carrier mobility of 45 $cm^2\ V^{-1}\ s^{-1}$, a high on-off ratio of 10^7 as well as the unique feature of both electron and hole conduction.

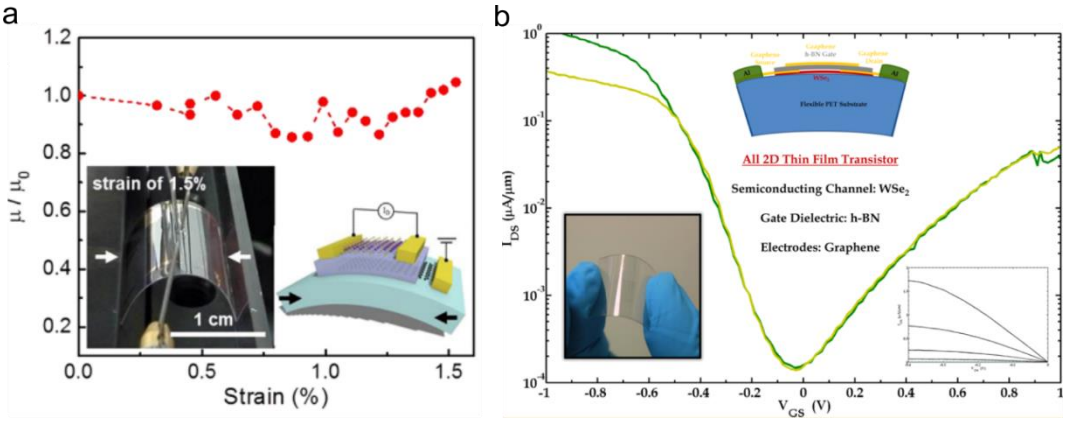


Figure 2-7 a. The photograph of the FET with the heterostructure of MoS_2-graphene-hBN and the curve of field-effect mobility vs. strain (adapted from [104]). b. An all-2D FET with the heterostructure of WSe_2-hBN-graphene and its transfer characteristics (adapted from [105]).

The tunable bandgap and good transmittance also make 2DMs competitive as the materials of flexible photodetectors[108]. Depending on the bandgap of 2DMs, the response wavelength range varies from the visible light (e.g. MoS_2) to near-infrared light (e.g. $MoTe_2$)[109]. Zhou *et al.* have demonstrated a flexible and transparent GaSe photodetector which shows efficient photoresponse to the visible light with a photoresponsivity of 30 mA/W[110]. Even though the flexible GaSe photodetector is

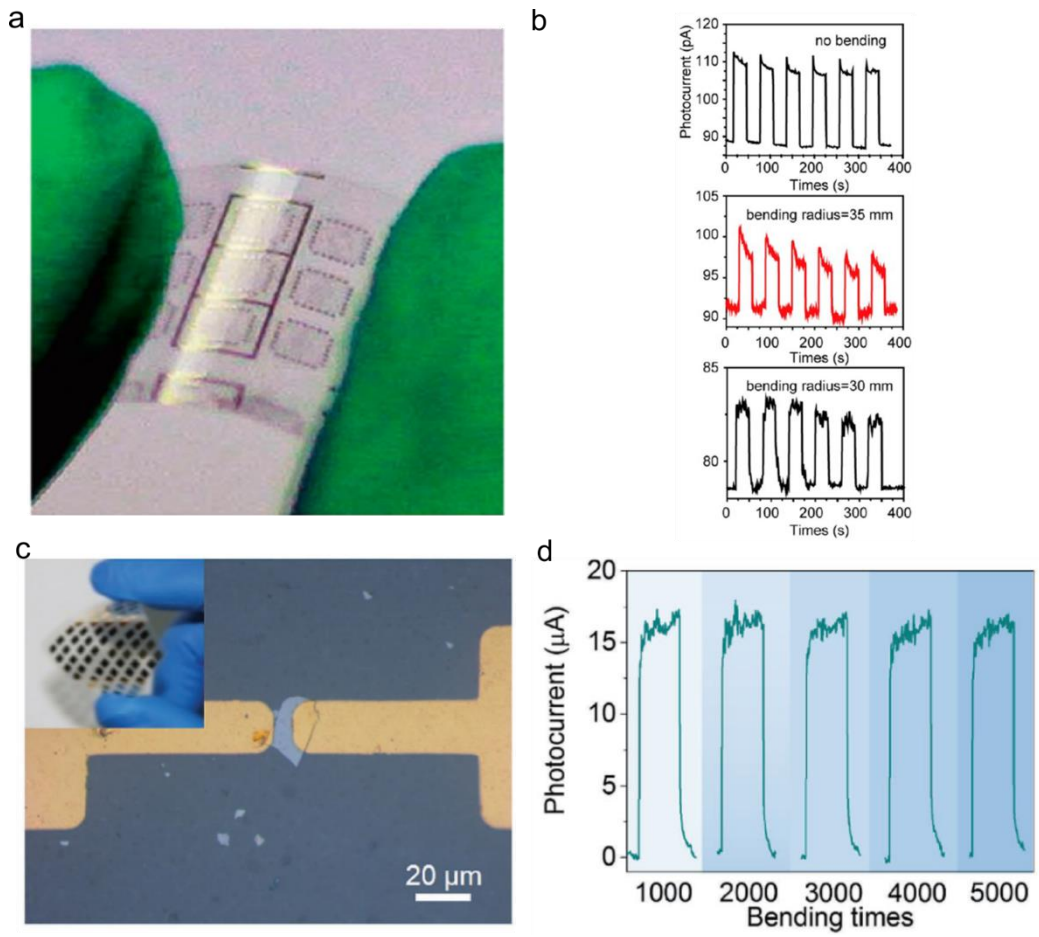


Figure 2-8 a. A flexible and transparent GaSe photodetector (adapted from [110]). b. Time resolved curve of the photocurrent of GaSe photodetector when the light is switched on/off under different bending radii (adapted from [110]). c. A flexible near-infrared photodetector based on $MoTe_2$ and graphene (adapted from [111]). d. Photoswitching behavior of the flexible $MoTe_2$/graphene photodetector after 5000 bending cycles (adapted from [111]).

repeatedly bended with different radii, the photoresponse can be fairly maintained (**Figure 2-8**a). With the bandgap of about 1 eV, $MoTe_2$ is the choice for near-infrared photodetector. Yu *et al.* have reported a flexible photodetector based on the heterostructure of $MoTe_2$ and graphene with a high photoresponsivity of 60 A/W at the wavelength of 1064 nm[111]. The monolayer graphene significantly increases the conductance and carrier mobility of the device, leading to a high photoresponsivity. After bending the flexible photodetector for 5000 times with the 1.2% tensile strain, the device still exhibits the same photoresponsivity, and no wrinkles and cracks are observed during the bending test due to the excellent mechanical properties of $MoTe_2$ and graphene[111] (**Figure 2-8**b).

However, the difficulty of patterning both polymeric substrates and 2DMs has restricted the applications of 2DMs in wearable and flexible technologies as both types of materials are quite sensitive to the strong radiation and hazardous chemicals. Although the conventional photolithography is still used to fabricate these flexible devices, the device performance is negatively influenced to some extent due to the defects induced by the UV light and organic solvents during the fabrication process[112–114]. The selection of polymeric substrate is limited as some polymers may be dissolved/damaged by the organic solvent. To build the flexible 2DMs-based devices with higher performance, it is important to develop a new sustainable manufacturing technique that is suitable for these sensitive materials.

2.2 Nanomanufacturing techniques for flexible devices

Despite the excellent mechanical flexibility, flexible materials are still facing the challenge of poor processability due to their degradation under strong radiation, hazardous chemicals and high temperature. Therefore, the microscale/nanoscale manufacture of flexible electronic and photonic devices is different from the conventional techniques used for rigid devices. The development of nanomanufacturing techniques that are suitable for flexible materials is the foundation of flexible technologies because nanomanufacturing builds the bridge between the new science and real flexible products. In this section, the main manufacturing techniques for the fabrication of flexible devices are discussed.

2.2.1 Scanning probe lithography

Scanning probe microscope has been used to write patterns for the first time in the late 1980s, indicating that scanning probe lithography (SPL) has become an alternative maskless lithoghraphy approach[115]. SPL can be based on either scanning tunneling microscope (STM) or atomic force microscope (AFM). Due to the advantage of operating the tip in ambient condition instead of high vacuum, most SPL techniques are based on AFM which relies on the force between the tip and the substrate surface to control the

tip position. An extremely sharp tip is utilised to write patterns with the feature size down to 10 nm[116]. Due to the ability to image the topography of the material surface, SPL possesses the unique advantage of writing and imaging patterns. As AFM can image the topography with the ultra-high resolution of 0.1 nm, the imaging ability helps to precisely locate the position where the pattern needs to be written. This is beneficial to writing features with strict alignment requirements. As the conventional photolithography always has the difficulty of nanoscale alignment due to the diffraction limit of light, alternatively, the AFM lithography technique will be a good solution to the problem without using markers as the reference.

Depending on the interaction between the tip and the substrate, SPL can be divided into mechanical, thermal, electrical and diffusive processes[115], among which the mechanical method is more suitable for patterning sensitive flexible materials without heating and chemical reactions. Mechanical SPL writes patterns in the material by applying the mechanical force on the tip through adding a constant voltage in contact-mode AFM. It can be regarded as a scratching process to remove the material in the patterned area. Mechanical SPL is able to pattern a wide range of materials that are softer than the tip, including metals, 2DMs, biomaterials and polymers[117–120]. Chen *et al.* have reported that using AFM lithography can pattern plasmonic AuNPs together with poly(methyl methacrylate) (PMMA) film at a high speed of 1000 μm s^{-1} [121] (**Figure 2-9**a, b). AuNPs grow up to a different size and shape at the pattern area where PMMA has been removed, forming a multiplexed nanostructure that can be used in OLED devices (**Figure 2-9**c). Zhang *et al.* also used mechanical AFM lithography to investigate the relationship between cutting forces and lattice orientations of graphene, which enables a better understanding of the mechanical properties along different lattice orientation of graphene[122].

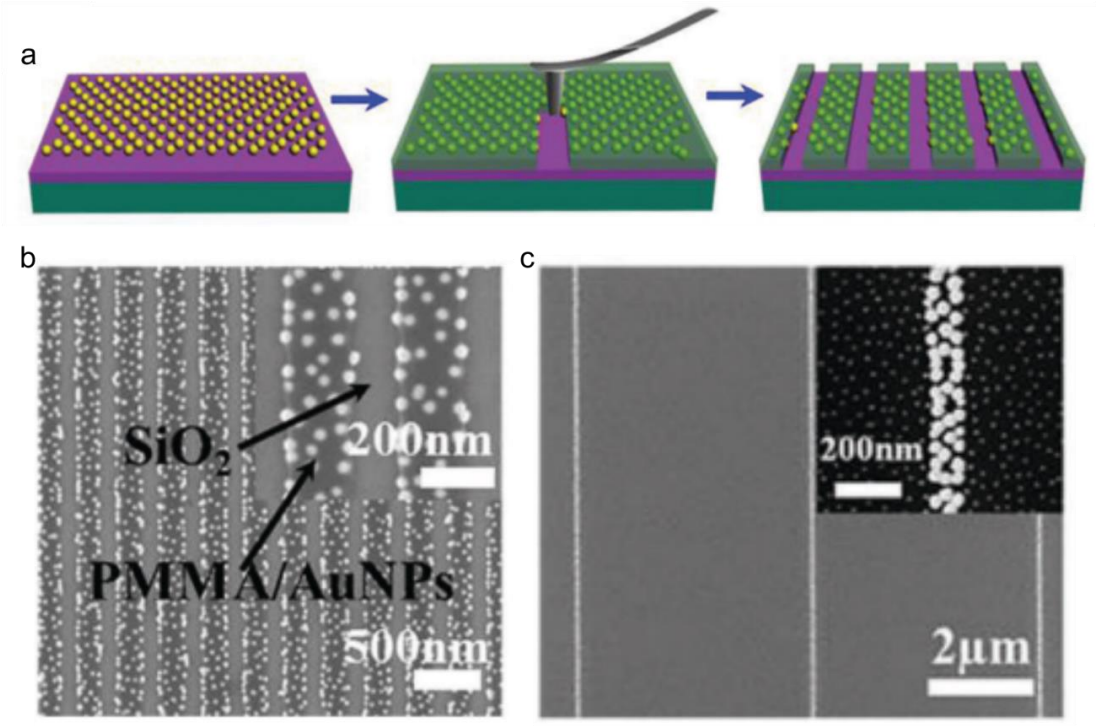


Figure 2-9 a. Schematic process of writing patterns in PMMA-AuNPs using AFM lithography. b. SEM image of the line patterns indicating PMMA-AuNPs are removed by the tip. c. SEM image after the deposition of AuNPs with bigger size on the line-pattern area. Adapted from [121].

Among various applications of AFM lithography, one common use of mechanical AFM lithography is to write patterns in a sacrificial polymeric resist layer such as PMMA, PS and PC. The pattern on the resist layer can then be transferred onto other materials through the following etching or lift-off process. Kim *et al.* have used the tip to write nanostructures in the bilayer polymer resist and transferred the nanostructures on the substrate by the deposition of Au and then the lift-off of the resist[123] (**Figure 2-10**). The mechanical force applied on the tip is kept constant during scratching the resist layer to make sure consistent feature size. The amount of the applied mechanical force is dependent on the thickness of the resist layer: the thicker the resist layer is, the bigger the mechanical force should be. However, a bigger mechanical force also leads to a bigger feature size written in the resist layer due to the pyramidal or conical shape of the tip. Therefore, to achieve fine features, a thinner sacrificial layer should be coated on the substrate.

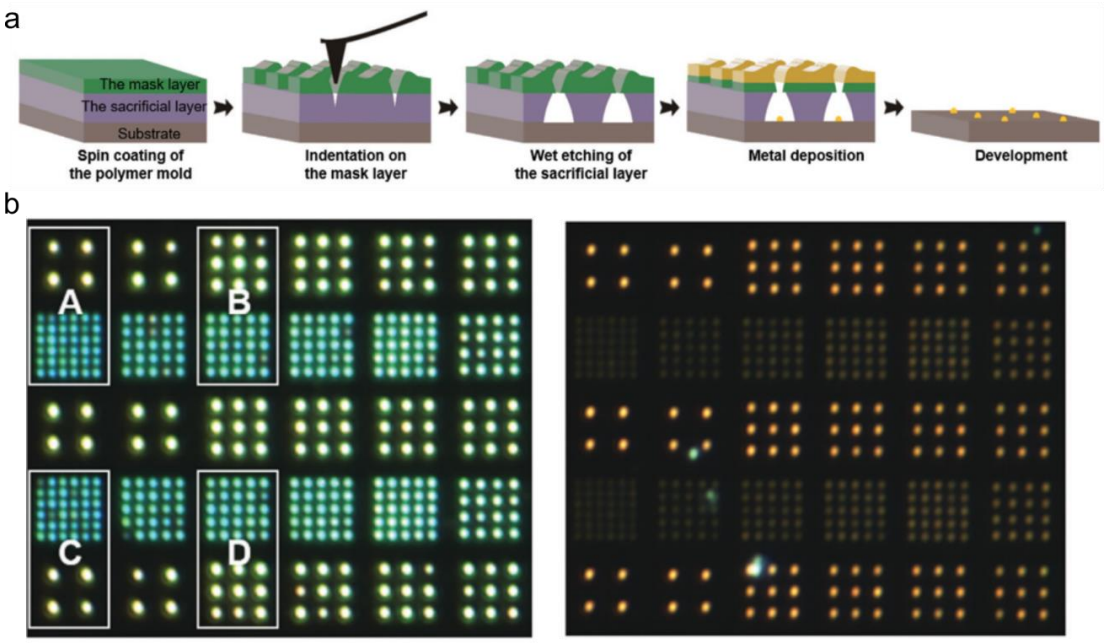


Figure 2-10 a. Schematic process of using the tip to write nanostructures in the resist layer and transferring the pattern onto the substrate by the deposition of Au and the lift-off of the resist. b. Dark-field images of nanostructures. Adapted from [123].

In addition, the feature size written by AFM lithography is also closely related to the dimension and the geometry of the tip. A finer tip is able to achieve a higher resolution, and the change in the tip geometry will cause a different shape of the pattern. Farmakidis *et al.* have demonstrated that the employment of an asymmetric tip and controlling the rotation of the scanning head can write patterns with the feature size varying from 1 μm to sub-50 nm within a single writing step[124]. This versatile approach provides an effective way to write complex lithographic patterns.

AFM lithography faces the challenge of properly controlling the mechanical force[125]. If the force is too small, it will cause the under-cutting problem where the resist layer is not completely removed. The final pattern will disappear after washing out the resist layer (**Figure 2-11**a). If the force is too large, it will cause the over-cutting problem where the tip scratches the substrate, which may severely damage the tip and substrate (**Figure 2-11**b). Both under-cutting and over-cutting should be avoided by monitoring the force so that the tip can stay at the interface between the resist layer and the substrate surface during scratching to exactly remove the resist. However, this is not easy to realise. With

the scratching process going on, the resist materials that have been scratched away will be piled up on the edge of the pattern, leading to an unstable writing process. To improve the stability of the writing process, Liu *et al.* have developed a phase-mode AFM lithography approach which combines a piezoceramic disk underneath the sample to cause the vibration of the cantilever during patterning and detects the phase response of the cantilever vibration[125]. As the phase response is related to the machining depth, monitoring the phase response can promptly adjust the tip position in vertical direction while writing patterns. By using this method, the under-cutting, over-cutting, and tip wearing problems can be addressed. This method is also able to nanomachine 2DMs with the advantages of the layer controllability and debris avoidance[126]. In spite of this new method, there are still limited solutions to these problems. Therefore, new approaches should be developed to make AFM lithography more effective in writing high-quality patterns.

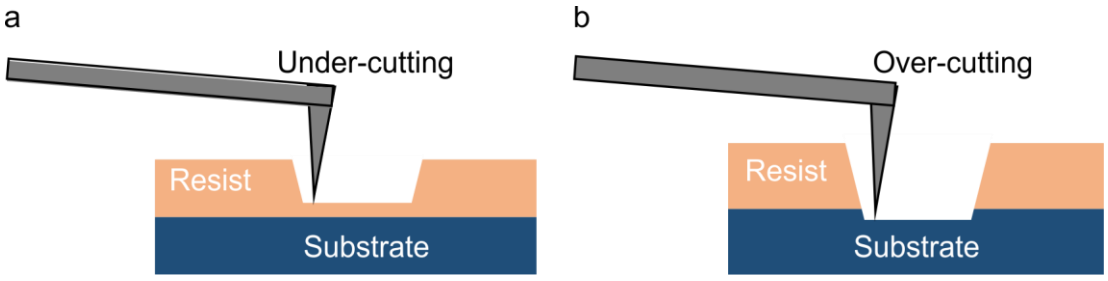


Figure 2-11 Problems of AFM lithography: a. Under-cutting. b. Over-cutting.

So far, AFM lithography has been barely used to fabricate flexible electronic and photonic devices, because the tip may damage the flexible substrates if the mechanical force is not properly controlled, and the chemical used to remove the resist layer may also dissolve/deform the flexible substrates. Based on these problems, a water-based mechanical bilayer lithography using AFM has been proposed to fabricate flexible functional devices for the first time in the thesis and details will be discussed in Chapter 4.

2.2.2 Inkjet printing

Inkjet printing is a ubiquitous rapid-prototyping technique that has been frequently used in daily life such as paper printing. It allows a direct writing way to deposit the solution-based materials into the preset pattern on the substrate, which reduces the materials waste and offers a sustainable solution.

Inkjet printing process

There are two working modes of inkjet printing: drop-on-demand (DOD) mode and continuous mode in which DOD mode is more frequently used. In a typical process of DOD mode, the solution-based ink is loaded into the nozzle before printing. By adding a pressure within the liquid, the ink overcomes the surface tension, enabling the ejection of ink droplets from the nozzle onto the substrate[127]. There are two mechanisms to generate the pressure within the liquid. One is enabled by the deformation of the piezoelectric actuator so that the generated pressure drives out the ink droplet (**Figure 2-12**a). The other method is based on the thermal process (**Figure 2-12**b). A heater mounted on the nozzle heats the liquid above the boiling temperature to form a bubble. The rapid expansion and collapse of the bubble can generate the pressure to push the ink droplet out. The piezoelectric actuator has fewer restrictions on the selection of ink

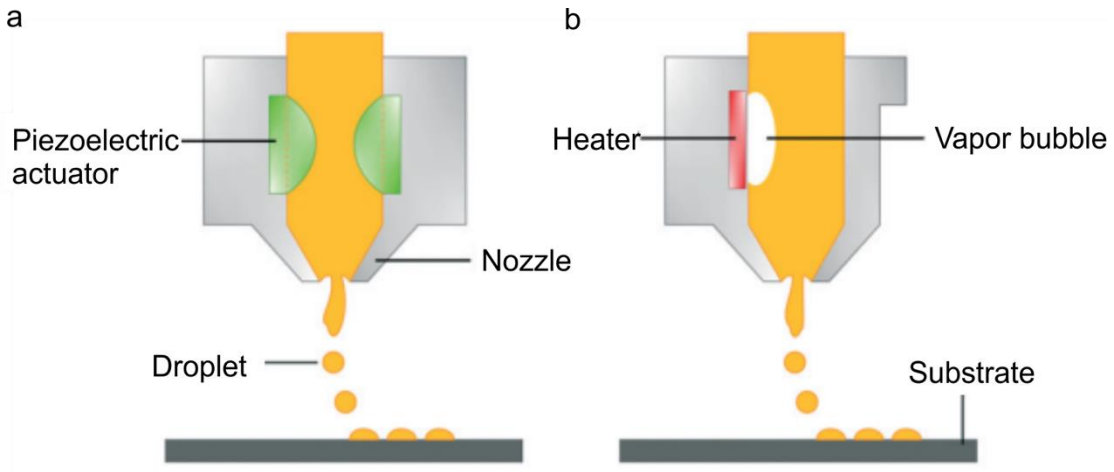


Figure 2-12 Drop-on-demand Inkjet printing process: a. piezoelectric mode. b. thermal mode. Adapted from [127].

materials compared to the thermal process, because the heat may adversely influence the properties of some ink materials.

Ink materials for inkjet printing

The droplet formation of DOD inkjet printing is dependent on the physical properties of the ink material such as the density, the surface tension and the viscosity. These properties are related to three dimensionless numbers of Reynolds number (Re), Weber number (We) and the inverse of Ohnesorge number (Oh) which are defined as follows[19]:

$$\mathrm{Re} = \frac{\text{inertial force}}{\text{viscous force}} = \frac{\rho v d}{\eta}$$

Equation 2-1

$$\mathrm{We} = \frac{\text{inertial force}}{\text{surface tension force}} = \frac{\rho v^2 d}{\gamma}$$

Equation 2-2

$$Z = \mathrm{Oh}^{-1} = \frac{\mathrm{Re}}{\sqrt{\mathrm{We}}} = \frac{\sqrt{\gamma \rho d}}{\eta}$$

Equation 2-3

where ρ, η and γ are the density, dynamic viscosity and surface tension, respectively, while v is the fluid velocity and d is the nozzle dimension. Z is the reciprocal of Ohnesorge number.

To obtain a stable jettability in DOD inkjet printing, Z value is recommended to be kept within the range of 1 to 10. If Z is below 1, viscous forces prevent the drop ejection from the nozzle. When Z is over 10, satellite droplets will form, leading to a low printing quality. As the dynamics of the fluid is rather complex, the Z value is just an approximate estimation of the jettability which suits most inkjet printing cases, but not all of them.

Based on these parameters, the composition of the ink is accordingly adjusted to realise high stability of the printing process. The selection of the solvent is important because

the solvent dissolves/disperses other ink materials and mainly determines the density, surface tension and viscosity of the ink. Solvents are divided into two categories which are aqueous and organic solvents (e.g. ethanol, isopropanol, toluene, glycols, etc.). Compared to the organic solvents, the viscosity and evaporation rate of aqueous ink are lower, and the surface tension is higher[127]. Volatile solvents evaporate quickly and have no additional requirement of heating, resulting in a simple and fast deposition process. However, the too fast evaporation speed may cause nozzle clogging. To balance the viscosity, surface tension and evaporation speed of the ink, a mixture of different solvents is commonly used[128].

In addition to the solvent, a small quantity of additives can be added to the ink as the surfactant, stabliser or dispersing agent. For instance, the polymer of ethyl cellulose is used to stablise the 2D material inks by extending the stable period of ink and improving the uniformity of printed patterns[15]. Triton X-100 is used to reduce the surface tension of TiO ink and prevent the appearance of cracks during the post thermal process[129].

Resolution of inkjet printing

The noncontact inkjet printing has a moderate resolution of about 5 μm. Its resolution is higher than screen printing but lower than conventional top-down lithography. There are several factors that determine the resolution of inkjet printing. Firstly, the feature size is directly related to the nozzle diameter. The reduction of the nozzle inner diameter can decrease the droplet size, but the droplet size is still equal to or even larger than the inner diameter of the nozzle. If the nozzle diameter is reduced to sub-micrometer, extremely high pressure is required to push the ink out and nozzle clogging problem may happen.

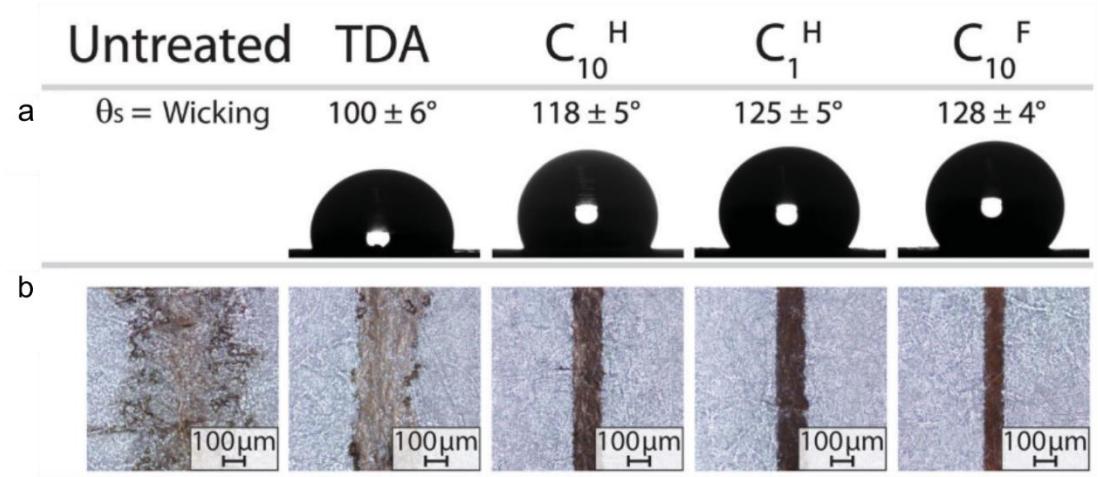


Figure 2-13 a. Images and static contact angles of drops of water on the untreated paper and modified papers with different organosilanes. B. Optical images of printed silver lines on the untreated paper and modified papers. Adapted from [130].

Surface modification of the nozzle is able to improve the resolution. Wu *et al.* have proposed a liquid-repellent modification method to make the surface of nozzle superamphiphobic, which decreases the droplet size[131]. The second factor that influences the resolution of inkjet printing is the coffee-ring effect caused by the capillary flow from the centre to the periphery within a drop[132]. When the solvent evaporates, the solute particles prefer accumulating at the periphery of the drop, forming a ring-like structure which is called the "coffee ring"[19]. The coffee-ring effect can be minimised by the method of Marangoni flow to drive the particles flow back to the centre[133,134]. The third factor influencing the resolution is the substrate wettability. Compared to the non-wetting surface, the droplet tends to spread on a wetting surface, leading to a large feature size[135]. Thus a higher resolution can be achieved by controlling the surface chemistry of the substrate. Lessing *et al.* have proposed that using omniphobic fluoroalkylated paper as the substrate can improve the resolution of the printed conductive pattern[130]. By making the paper hydrophobic with different organosilanes, the printed water droplet is finer on each modified paper compared to that on the untreated substrate[130] (**Figure 2-13**).

Applications in flexible technologies

A wide range of materials have been used as ink materials in inkjet printing including polymers, biomaterials, 2DMs, and metallic materials[14,16,19,137–141]. Inkjet printing has the advantage of the excellent compatibility with flexible substrates such as paper, PET and PEN[142–144]. Thus, it has been extensively used to manufacture flexible and wearable devices with low cost and high throughput, including various sensors(e.g. biological/gas/temperature/strain sensors), OLEDs, TFTs, energy storage devices, and photodetectors[145–151]. Viola *et al.* have used inkjet printing to fabricate an all-organic FET with only 150 nm thickness which allows perfect adhesion on the curved surface of skin and bending with the radius less than 1 μm[136]. The insulating polymer of poly(vinyl formal) (PVF) is printed as both the substrate and the dielectric layer, the organic semiconductor as the active channel, and the conducting polymer of PEDOT:PSS as the source/drain and gate electrodes (**Figure 2-14**).

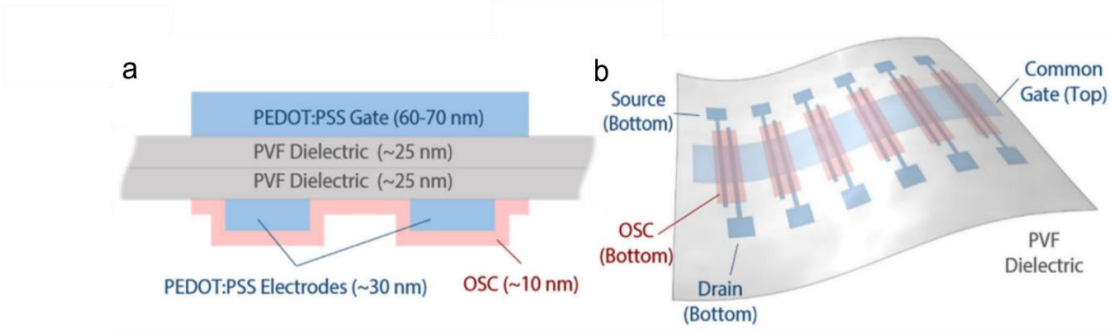


Figure 2-14 The structure of the ultrathin all-organic FET: a. Lateral view. b. Overview. Adapted from [136].

Although inkjet printing is an economical and scalable manufacturing technique that has various applications in flexible and wearable technologies, its relatively poor resolution of about 5 μm still blocks the industrialisation way to the mass production of flexible integrated circuits with high resolution. To achieve higher resolution, a high electric field has been integrated with inkjet printing, leading to the development of EHD printing technique.

2.2.3 Electrohydrodynamic printing

The resolution of inkjet printing is limited by the fact that reducing the nozzle diameter to sub-micrometre is rather difficult because it requires extremely high pressure to overcome the capillary force. EHD printing is an improved direct printing technique based on the inkjet printing, and its resolution can reach 50 nm which is much higher than that of inkjet printing[152]. The difference between EHD printing and inkjet printing is that EHD printing employs the electric force to pull the ink out while inkjet printing utilises the pressure to push the ink out.

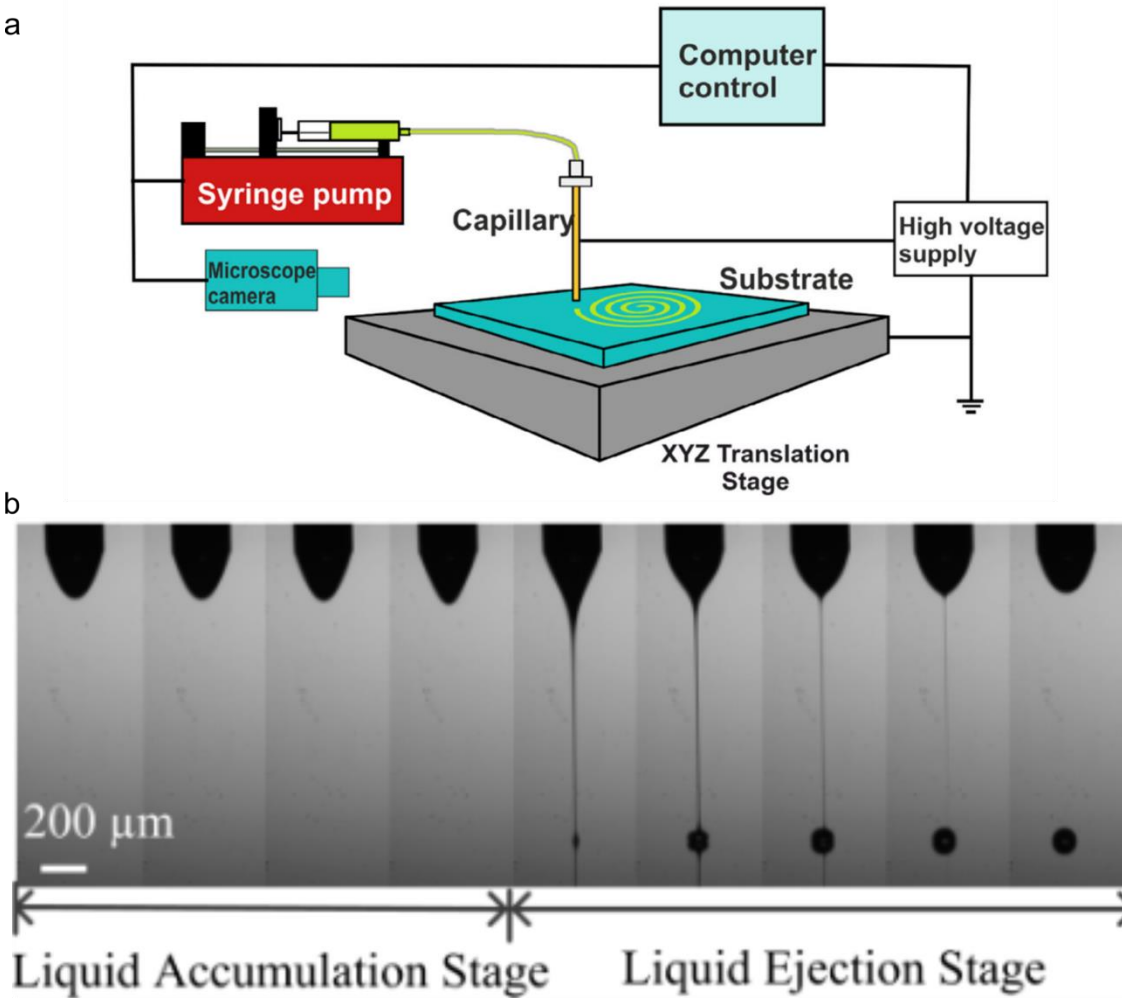


Figure 2-15 a. Schematic of a typical EHD printing system (adapted from [153]). b. The formation of Taylor cone and the liquid jet ejection in EHD printing (adapted from [154]).

Mechanisms of EHD printing

A typical EHD printing system consists of three-axis stages, a high voltage supply, a camera system, a back pressure supply system (e.g. syringe pump or pneumatic system), a nozzle and a computer controlling system (**Figure 2-15**a). In EHD printing, a high electric field is applied between the nozzle and the substrate, forming a meniscus at the tip of the nozzle under the balance between the surface tension force and the sum of electric force and gravitational force[155]. When the electric field is high enough to overcome the surface tension force, the meniscus will deform into a Taylor cone and form a liquid jet (**Figure 2-15**b). The voltage corresponding to the formation of the Taylor cone is called critical voltage. Therefore, the printed feature size can be 10-1000 times smaller than the inner diameter of the nozzle[156]. Due to its direct printing capability, EHD printing is a sustainable, low-cost and high-yield manufacturing technique without the redundant waste of materials.

Modes of EHD printing

The EHD printing process can be categorised into different modes: dripping mode, pulsating mode, cone jet, tilted jet, twin jets and multi jets[157,158]. With the low flow rate and electric field, droplets pinch off from the nozzle mainly due to the gravitational force but still with the help of electric force[157]. By slightly increasing the flow rate and electric field, a pulsating jet forms due to the repeated cycle of the formation of Taylor cone, droplet ejection and relaxation back to the spherical meniscus[21]. A further increase in the electric voltage higher than the critical voltage results in the cone jet. It is the ideal mode of EHD printing as the Taylor cone is kept stable and a continuous jet falls along the capillary axis (**Figure 2-16**). By continually increasing electric field, tilted jet, twin jets and multi jets can be obtained because of the excessive charge built up on the tip of the nozzle[158].

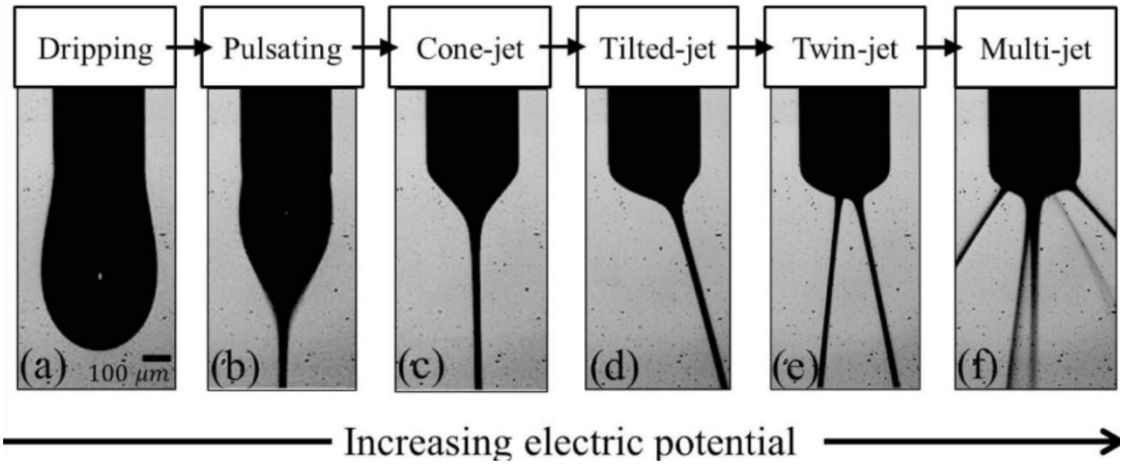


Figure 2-16 Different modes of EHD printing. Adapted from [157].

Properties of ink

Chen *et al.* have estimated the jet flow rate Q in EHD printing by using the Poiseuille-type relation[159,160]:

$$Q \approx \frac{\pi d_N^4}{128\mu L}\left(\Delta P + \frac{1}{2}\varepsilon_0 E^2 - \frac{4\gamma}{d_N}\right)$$

Equation 2-4

Where d_N and L are the diameter and length of the nozzle, respectively, ΔP is the hydrostatic pressure, μ is the viscosity of ink, ε_0 is the vacuum permittivity, E is the external electric field, and γ is the surface tension of the interface between ink and air. Thus, the viscosity and surface tension are two important factors to influence the jet flow rate in EHD printing. Higher viscosity of ink corresponds to lower jet flow rate. However, the recommended jet formation range of Z value of $1<Z<10$ in inkjet printing has been rarely used in EHD. Instead, the condition to eject the ink from the nozzle in EHD printing is when the flow rate Q is over 0 according to Equation 2-4, which means $\Delta P + \frac{1}{2}\varepsilon_0 E^2 > \frac{4\gamma}{d_N}$. Therefore, the surface tension of ink should be controlled within a proper range. Otherwise, a too low surface tension will result in the formation of satellite droplets and

a too high surface tension will require an extremely high electric field to ensure jet ejection[161,162].

The conductivity of ink is another key factor to influence the EHD printing process. Under the electric field applied between the nozzle to the substrate, charges in the ink tend to accumulate at the tip of nozzle, forming the meniscus. Owing to the colulombic repulsion between the same type of charges, the radius of the meniscus becomes gradually smaller until the jet ejection happens when the electrostatic force overcomes the surface tension[21]. Ink with the higher conductivity carries a higher density of charges, hence facilitating the ejection process. Zhang *et al.* used 10 kinds of dielectric silicone oils with almost the same conductivity but various viscosities as the inks of EHD printing, but no continuous cone jet was observed due to the low conductivity of inks[163]. Instead, only unsteady jets were generated.

In addition, ink properties also influence the droplet resolution in EHD printing. Guo *et al.* have studied the individual influence of the viscosity and conductivity of the ink on the resolution of the printed droplet while keeping other systematic parameters unchanged (e.g. applied voltage, nozzle-to-substrate distance and moving speed of the substrate)[154]. They find that under the condition when Taylor cone forms, lower viscosity and higher conductivity of the ink are favourable to achieve a high-resolution pattern due to the reduction of the ejection volume. Additives are also used to optimise these factors in EHD printing. For example, Chang *et al.* have used polyethylene oxide (PEO) to increase the viscosity and the surface tension of PEDOT:PSS ink for EHD printing[164].

Systematic parameters

The EHD printing process is very complex as systematic parameters also affect the jettability other than properties of the ink. Systematic parameters include the applied voltage, the nozzle-to-substrate distance, the flow rate, the nozzle diameter and the moving speed of translational stages.

The magnitude of the electric field is mainly determined by the applied voltage together with the nozzle-to-substrate distance. Under a constant applied voltage, the nozzle-to-substrate distance should be controlled at a proper length to obtain a continuous and stable jet. The distance should be far enough for the jet formation and meanwhile close enough to avoid the disintegration of the jet into droplets while falling[153]. A high voltage with small nozzle-to-substrate distance may lead to electrical breakdown, resulting in the damage to substrate surface. A direct (DC) voltage has been mostly applied in previous EHD printing examples in the literature. However, for insulating substrates, the excessive charges on the ejected jet may cause non-uniform patterning and even position shift. Byun *et al.* have demonstrated the DOD EHD printing on the polymer substrate by using alternating current (AC) voltage[165]. The use of AC voltage enables the continuous ejection of droplets which happens at either positive peak or negative peak of the electrical signal.

Flow rate is controlled by the back pressure which guarantees continuous delivery of the ink to the nozzle tip. As discussed before, the flow rate and electric field are closely related to the mode of EHD printing. Chen and Scheideler have reported that a minimum flow rate is necessarily applied to stabilise the Taylor cone-jet and is dependent to the diameter of the nozzle for highly viscous inks[166]. However, an extremely high flow rate is also unfavourable because it may lead to satellite droplets.

Other than inkjet printing, the nozzle diameter in EHD printing can be reduced to nanoscale. Galliker *et al.* have demonstrated to directly print nanostructures with the resolution up to about 50 nm with the use of a 550-nm nozzle[152]. The reduction of nozzle diameter helps to achieve a high-resolution pattern at the nanoscale. Surface modification by coating the metallic nozzle surface with a hydrophobic monolayer also assists to obtain finer features[21,167].

Translational stages are used to control the motion of the substrate during printing. The moving speed of stages influences the feature size and quality of printed patterns[168]. Phung *et al.* have demonstrated that a too slow speed will cause a bigger feature size but a too quick speed will lead to a discontinuous pattern for EHD printing[169]. For the stable cone-jet mode, a proper increase in the moving speed enables the reduction of the feature size.

Environmental factors such as temperature and humidity will also cause variations in the printing process. Sammons *et al.* have found that the increasing temperature leads to a decrease in the jetting voltage and frequency and increases the droplet diameter with respect to the ink they use[170]. Therefore, it is important to monitor environmental factors to achieve high reproducibility[158].

In addition, the surface chemistry of the substrate is closely related to the resolution of printed patterns. Printed ink tends to spread over the substrate and have a smaller contact angle if the surface is highly wettable[153]. As discussed in inkjet printing, controlling the surface chemistry by coating the substrate with a layer of hydrophobic or hydrophilic molecules can improve the resolution.

Applications in flexible technology

A wide range of materials have been demonstrated to be printable in EHD printing such as organic polymers, quantum dots, metallic materials, 2DMs, biomaterials and composites[12,171–180]. Nevertheless, the ink of EHD printing requires mobile charges, dielectric materials with electrical conductivity of ~ 10^{-13} S/m have also been demonstrated to be printable with a fine jet[181]. EHD printing possesses a high resolution up to 50 nm which is 2 orders of magnitude higher than inkjet printing. Taking into account the wide choices of ink materials, high resolution, direct and quick writing ability as well as low cost, EHD printing is a promising micro/nanomanufacturing technique for printing flexible devices. **Table 2-2** summarises most functional materials that have been

used in EHD printing for applications in flexible and wearable technologies. Four points are highlighted here. First, the number of materials that have been EHD printed on flexible materials is quite limited compared to the ones that have been printed on conventional rigid substrates. Although these materials cover conductors, semiconductors and insulators, studies on the fabrication of flexible devices using EHD printing are still insufficient. Secondly, although the resolution of EHD printing can reach 50 nm, features that have been printed onto flexible substrates are still at the microscale. Due to the insulating nature of flexible substrates, the charge accumulation issue becomes dominant, which cause the instable printing process. The residual charges on the printed droplet repulse each other when arrive at the insulating substrate, lowering the resolution of printed features[182]. Third, there is a lack of research exploring the EHD printing of biomaterials on both rigid and flexible substrates. Last, most of these applications are based on flexible electronics but not photonics. The use of EHD printing for flexible photonic devices has not been extensively explored, because photonic devices require a high uniformity of the geometry of printed features. However, the charge accumulation issue on insulating substrates limits the application of EHD printing in flexible photonics.

Table 2-2 Functional ink materials of EHD printing for flexible and wearable technologies

Classifications	Inks	Substrates	Applications	Finest feature	Reference
Metallic materials	AgNWs	PET, PDMS, paper, nature rubber latex	Heater	45 μm	183
	AgNPs	PET/PI	Electrodes/metamaterials	4.6 μm/10 μm	184,185
	Molten metals with low T_m	PDMS, PET, photo paper	Touch sensor	Sub 50 μm	186
	In_2O	PI	TFT	6 μm	187
	ZrO_2	PI	Memory	-	188
Organic polymers	PEDOT:PSS	PET	Heater	27.25 μm	164
	Polyaniline	Plastic substrate	Gas sensor	-	70
	TIPS-pentacene	PES	OFET	-	189
	Photoresist	PET	Mask for etching	5 μm	190
	Polyvinylidene fluoride	PI/ Ecoflex substrate	Mask/Strain sensor	5 μm/3 μm	191,192
	PFS-co-PVBCi (3:7)	PET	OTFT	-	193
	NOA61 UV-curable polymer	PDMS	Optical microlens	8.59 μm	194
2DMs composites	WS_2	PET	Memory	-	195
	PEDOT:PSS/Graphene/SWCNT	PDMS	Pressure sensor	-	196
	MoS_2-polyvinyl alcohol (PVA)	PET	Memory	-	197
	hBN-PVA	PET	Memory	42 μm	198
	Cellulose acetate-ibuprofen & Chinese herbs-polyvinylpyrrolidone	-	Medicine	-	199
Biomaterials	Protein	Hydrogel	Cell culture	5 μm	200

2.2.4 Direct laser writing

Direct laser writing (DLW) based on multiphoton polymerisation possesses the extraordinary advantage of being capable of printing both 2D and three-dimensional (3D) structures. In principle, an ultrafast femtosecond laser is tightly focused inside a tiny volume of a transparent material that has been pre-coated on the substrate, which leads to the absorption of two or more photons and the local polymerisation[201]. It is a direct writing process because the final structure is directly built without a following deposition/etching step but just a development step to wash away the unexposed materials.

The multiphoton absorption is defined as a nonlinear process where an atom or molecule is excited to a higher state by simultaneously absorbing the energy from more than one photon through virtual states[202]. This process requires high peak powers, thus requiring a femtosecond pulsed laser.

Based on the theory of multiphoton absorption, materials that are suitable for DLW are composed of at least a polymerisable material (e.g. monomer) which will become the final polymeric structure and a photoinitiator that will absorb the laser and provide the active species to cause the polymerisation[203]. There are two types of photoinitiators, including radical photoinitiators and cationic initiators. Radical photoinitiators such as benzophenone and its derivatives[204] take up the majority of the related research in DLW. Free radicals are generated by radical photoinitiators under the exposure to the light so that polymerisation of acrylates or vinyl ethers can be initiated[203], while cationic initiators generate a photoacid which acts as the catalyst for the polymerisation of epoxides and vinyl ethers[205]. To focus the laser inside the volume of materials while avoiding ablation, polymerisable materials should be transparent at both the laser wavelength and the two-photon absorption wavelength[206]. Organic photopolymers, SU-8, photosensitive hybrid materials and hydrogels are commonly used polymerisable materials in DLW[207–213].

Regarding the resolution of DLW, a great number of complex 3D structures in microscale built by DLW have been reported in literature[213–215]. The achievable resolution of DLW reaches sub-50 nm which is beyond the diffraction limit. Cao *et al.* have achieved dots of 40 nm and lines with the minimum linewidth of 130 nm by introducing a second laser beam with the different wavelength to enable the photoinhibiting process that is integrated with the original photoinitiating process in polymerisation[216]. One big challenge in DLW is the difficulty of accurately recognising the interface between the substrate and photosensitive material during the laser scanning, especially for the substrate with high roughness. If the exposed structure is not properly in contact with the substrate, it will lead to the discontinuity in the pattern or even worse no pattern remaining after development. Mohr-Weidenfeller *et al.* have proposed to combine the DLW with the nanopositioning and nanomeasuring machine, which results in the improvement of ultra-precise positioning and the elimination of stitching errors[217]. With the improved DLW system, a fine and continuous line with a width of 38 nm has been achieved. However, currently such high resolution has only been achieved for simple 2D structures of dots and lines. Complex structures at the nanoscale are still hard to write with DLW.

Owing to the high quality and uniformity of 3D structures written by DLW, it has been extensively used in photonic applications[218–220]. Gissibl *et al.* have demonstrated the DLW of various ultracompact multi-lens systems with outstanding optical performance and high resolution for imaging applications[221]. The feature size of the multi-lens system is about 100 μm, which helps the miniaturisation of optical elements for applications in endoscopic imaging. Dietrich *et al.* have also used DLW to build 3D optical free-form elements such as total internal reflection mirrors and beam expanders that are built at connections of different photonic platforms to greatly improve the light coupling efficiency[222] (**Figure 2-17**). These two studies are based on rigid substrates. For flexible substrates, Remmel *et al.* have used DLW to build a novel whispering gallery mode

resonator consisting of opposing half-disks with an intermediate air gap on the PDMS substrate[223]. The resonance wavelength can be tuned by varying the gap width through mechanically stretching the PDMS substrate. However, the exploration of DLW in flexible photonics is still lacking. Although the photosensitive polymer used in DLW should have the conformability with flexible substrates while stretching or bending, writing patterns on flexible polymeric substrate is still a challenge due to the high roughness and laser-induced damage to polymers.

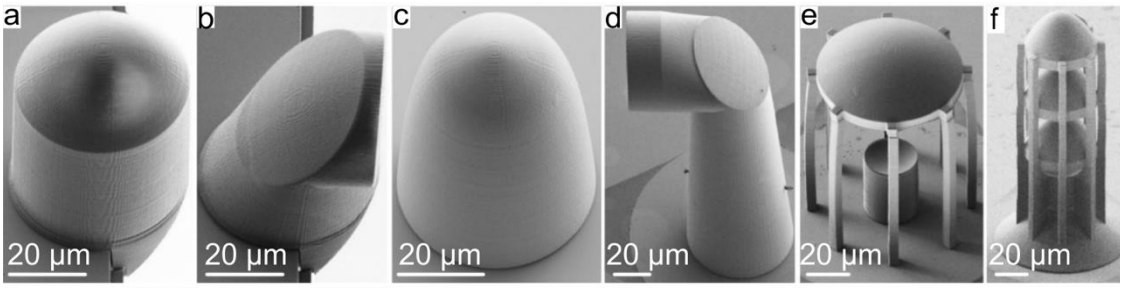


Figure 2-17 Various optical free-form elements printed by DLW: a, b Free-form lens. c, d Free-form lens with high NA. e, f Beam expander. Adapted from [222].

DLW has also been applied in flexible electronics and tissue engineering. In flexible electronics, the use of DLW is to achieve selective metallization on polymer substrates for depositing electrodes[224]. In tissue engineering, 3D biological scaffolds have been directly printed by the DLW of biodegradable biopolymers[204,208].

2.2.5 Nanoimprint lithography

Chou *et al.* have demonstrated the nanoimprint lithography with 25-nm resolution for the first time in the 1990s[225,226], which enables a new approach to replicate microscale/nanoscale patterns.

In principle, a mould with the desired pattern is pressed into a polymeric resist coated on the substrate under a proper temperature and pressure, which leaves a thickness contrast in the resist[227]. Then the pattern is transferred onto the substrate by an etching process such as reactive ion etching to remove the residual resist in the pressed area. This is a thermal nanoimprinting process (**Figure 2-18**a). The polymeric resist is heated

above its glass transition temperature under a certain pressure for a period of time[228]. The glass transition temperature activates the motion of entire chains and a viscous flow, leading to the irreversible deformation of the resist after pressing the mould into the resist. Alternatively, a transparent mould with patterns and a low-viscosity UV-curable resist are used during the embossment process with UV light irradiation (**Figure 2-18**b). UV light solidifies the resist, thus enabling a room-temperature nanoimprinting process.

The mould in nanoimprinting plays an important role in achieving uniform patterns and

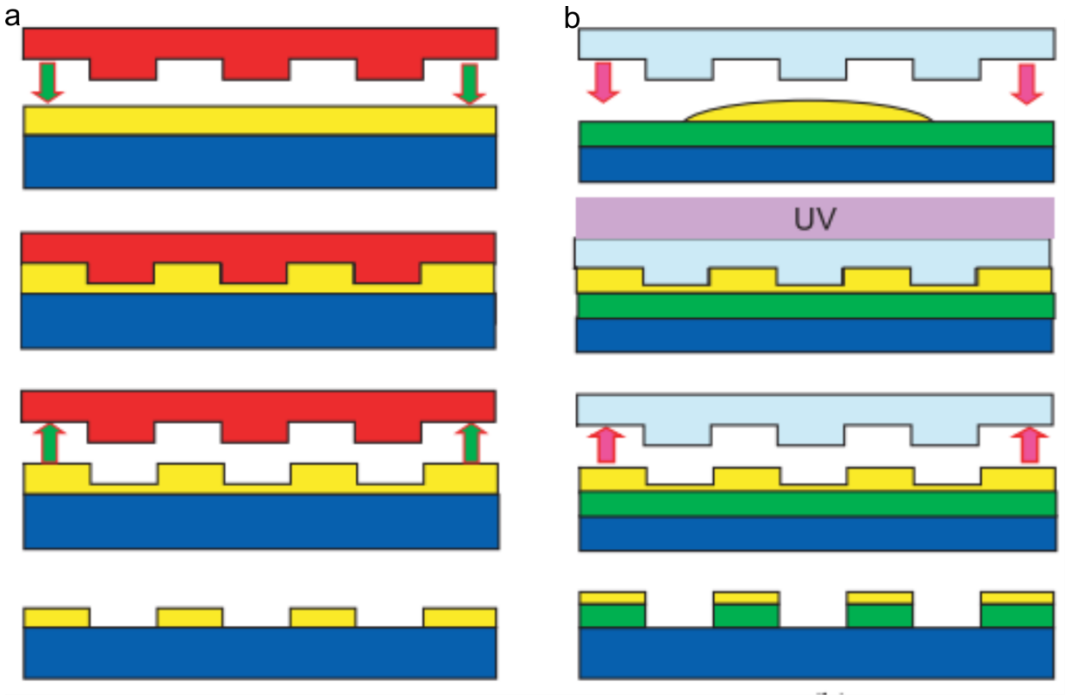


Figure 2-18 Schematic of nanoimprinting process: a. Thermal nanoimprinting. b. UV nanoimprinting. Adapted from [227].

high resolution. Conventional photolithography (for microscale features) or electron-beam lithography (for nanoscale features) are two common ways to write the predefined patterns on the mould. Si and SiO_2 are two good candidates as the mould materials due to their excellent hardness and durability[229]. One challenge of nanoimprinting is to achieve the long durability and high quality of the mould. To enhance the durability, a widely used solution is to avoid the adhesion of the resist to the mould by depositing a monolayer of fluorosilane molecules such as 1H,1H,2H,2H-perfluorodecyl-trichlorosilan on the mould surface to reduce its surface energy. To achieve high quality, the mould

should have a high aspect ratio to make sure that a clear and defectless pattern is transferred onto the substrate.

Nanoimprinting is capable of writing high-resolution patterns with a low cost and high throughput. There are numerous applications of nanoimprinting in electronics, photonics, magnetics and biology[230,231]. However, nanoimprinting faces some challenges when applied on flexible substrates. First, flexible substrates have low tolerance of high temperature and pressure during the thermal imprinting process. UV light used in UV nanoimprinting may also cause the degradation of flexible polymeric substrates. Secondly, the etching or following lift-off process may damage the flexible substrates due to the use of hazardous chemicals and gas.

Some studies have used different resist materials to reduce the damage to flexible substrates. The resist material coated on the substrate in nanoimprinting is based on polymers. This indicates that the deposition of a metal is an indirect process because patterns are created in the resist by the mould and then transferred onto the substrate, so chemicals have to be used in the lift-off step. To avoid the lift-off, Park *et al.* have proposed a direct metal deposition method by the use of Au nanoparticle solution as the resist in nanoimprinting process[232]. High-quality Au patterns with little residue are directly created on the substrate by pressing PDMS mould with a moderate temperature and low pressure. There is no need for following etching, deposition and lift-off steps. Thus, the metal deposition process has been significantly simplified. In another work conducted by Chen and co-workers, the functional material of PVDF/$BaTiO_3$ nanocomposite is also directly coated on Kapton substrate and embossed by the PDMS mould with the predefined micropillar structure[233]. The embossed micropillars in the nanocomposite are applied as self-powered flexible sensors.

In addition, variations of nanoimprinting such as roll-to-roll nanoimprinting has also been demonstrated on flexible substrates. Ahn *et al.* have proposed the continuous UV roll

nanoimprinting in which a pattern roll stamper is used for the replication of microscale/nanoscale patterns in large area on both rigid and flexible substrates[234]. With roll-to-roll nanoimprinting, patterns with feature size down to 70 nm can be continuously imprinted on flexible PET substrates[235]. Due to the continuous and large-area patterning, roll-to-roll nanoimprinting has an even lower cost and higher throughput than conventional nanoimprinting.

Another variation of nanoimprinting is to use the PDMS stamp to transfer structures between various platforms to satisfy a specific demand. Recently, Ali *et al.* have demonstrated the pick-and-place of a single nanowire with the diameter of 120–400 nm by using a polymer filament and the PDMS stamp[236]. The use of transparent PDMS stamp enables a precise way to transfer a single nanowire to the desired position, which brings more opportunities for the fabrication of electronic and photonic devices based on functional nanowires.

2.3 Chapter summary

Having discussed the common materials used in wearable and flexible technologies, it is clear that there are particular considerations of the manufacturing techniques for sensitive flexible materials due to their low resistance to hazardous chemicals, high temperature and strong irradiations.

This chapter also elaborates the state of the art of current nanomanufacturing for flexible technologies, including mechanisms, resolution, applications and cost-effectivity. Each manufacturing process consumes materials and energy, as well as releases waste that brings a negative impact on the environment. Therefore, it is important to comparing their sustainability by considering the manufacturing process based on the framework of 12 principles of green engineering developed by Anastas and Zimmerman. 12 principles of green engineering include: (1) Inherent rather than circumstantial; (2) Prevention Instead of Treatment; (3) Design for separation; (4) Maximize efficiency; (5) Output-

pulled versus input-pushed; (6) Conserve complexity; (7) Durability rather than immortality; (8) Meet need, minimize excess; (9) minimise material diversity; (10) integration material and energy flows; (11) design for commercial “afterlife”; (12) renewable rather than depleting[237].

Table 2-3 gives a brief summary of manufacturing techniques discussed in this chapter, including their cost, resolution, scalability, the use of organic solvents, applications in flexible technology and sustainability. Here, the comparison of the sustainability of manufacuturing techniques for flexible technologies is mainly based on principles (1) and (2). Principle (1) emphasizes the use of inherently non-hazardous materials and energy, while principle (2) focuses on preventing the waste at the source rather than the waste treatment[237].

Challenge

Table 2-3 shows that organic solvents are inevitably used in most of current nanomanufacturing techniques for flexible technologies, which is the major source of the hazardous waste and the low sustainability. In addition, most manufacturing techniques, except inkjet printing and EHD printing, are resist-based, which indicates the decrease of production efficiency due to the waste of resist materials. Therefore, the main problems of current manufacturing techniques are the use of hazardous organic solvents and the materials waste.

Hypothesis and objectives

To overcome both difficulties, my hypothesis is that the use of water as the solvent instead of organic solvents is one solution to developing a more sustainable nanomanufacturing technique. Furthermore, the application of additive nanomanufacturing techniques in building flexible devices helps to conserve both materials and energy. To verify both points of the hypothesis, a water-based mechanical bilayer lithography is proposed and applied to fabricate flexible devices in Chapter 4–5,

and the additive EHD printing of biomolecules is used to add bio-functionality for the electronic platform of transistors in Chapter 6.

Table 2-3 Summary of current manufacturing techniques for flexible technologies[9,12,115]

	SPL (AFM)	Inkjet printing	EHD printing	DLW	Nanoimprinting
Cost of equipment[1]	Low	Low	Low	Medium	High
Highest resolution[2]	~ 10 nm	~ 5 μm	~ 50 nm	~50 nm	~ 15 nm
Throughput[3] (μm²/hour)	1–10^5	>10^{13}	10^4–10^9	10^2–10^6	10^9–10^{13}
The use of organic solvents[4]	Yes	Except aqueous ink	Except aqueous ink	Yes	Yes
Applications in flexible technology[5]	Rare	Extensive	Extensive	Extensive	Extensive
Sustainability[6]	Low to medium	Medium to high	Medium to high	Low to medium	Medium to high

Criteria and importance of each aspect of manufacturing techniques:

[1]Cost of equipment: low is less than $100, 000; medium is from $100, 000 to $ 1 million; high is over $ 1 million. This can be used to estimate the affordability and accessibility to each technique.

[2]Highest resolution: represents the patterning capability of each technique. The value is from the investigation of the published work including both flexible and rigid substrates.

[3]Throughput: is the patterning speed of each technique. It can be used to estimate the production time for a certain number of devices.

[4]The use of organic solvents: organic solvents can be hazardous, toxic and carcinogens. Harmful organic solvents form the major composition of the manufacturing hazardous waste, leading to the damage both to the environment and staff of manufacturing companies. Therefore, it is important to understand if the manufacturing process involves any organic solvents.

[5]Applications in flexible technologies: based on the investigation of the published work related to flexible technologies.

[6]Sustainability: sustainable manufacturing technique helps to protect the environment and conserve natural resources, which improves the living quality of humans. The criteria to assess

sustainability is mainly based on the minimisation of using hazardous chemicals during the manufacturing process, which is corresponding to 2 of 12 principles of green engineering: (1) inherent rather than circumstantial; (2) prevention instead of treatment.

Chapter 3

Experimental methodology and metrology

3.1 Introduction

This chapter introduces the setups of the two fabrication techniques, mechanical lithography by AFM and EHD printing, by which photonic and electronic devices were prepared, respectively. The mechanism of how to control a commercial AFM to do mechanical lithography is elaborated, and each component used in EHD printing and the nozzle preparation are presented. The metrology methods to characterise various properties of prepared devices are also detailed, including imaging, surface topography, chemical analysis, optical characterisation and device performance measurement.

3.2 Equipment

3.2.1 Mechanical lithography by AFM

The setup used for mechanical lithography is a commercial AFM (Asylum MFP-3D). The mechanical lithography presented in this work has been carried out by maintaining a constant cantilever deflection in the contact mode of AFM. Tips used for conventional mechanical lithography have a high hardness so that they can be highly wear-resistant during patterning. To increase the hardness, tips are coated by diamond or diamond-like

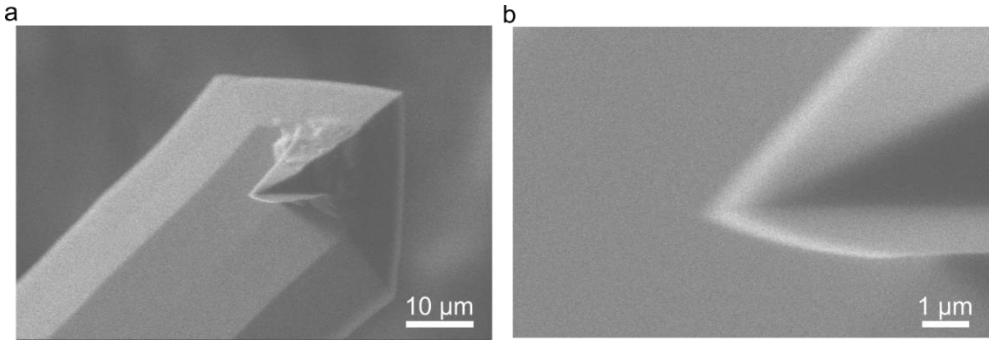


Figure 3-1 a. SEM image of a new Tap-300 G probe with the rotated tip. b. SEM image of the zoom-in view of the new tip.

carbon, which is rather expensive. To demonstrate the low requirement for the hardness of the tip and easy accessibility to the tip, no expensive and hardened tip was used. Instead, more common and cheap Tap300-G Si probes (k = 40 N/m, Budget Sensors) with rotated tips (radius of ~10 nm) were used for both imaging and patterning (**Figure 3-1**).

During the mechanical lithography process, different mechanical forces were applied on the cantilever. The application of mechanical forces is realised by calibrating two parameters which are optical lever sensitivity (OLS) and spring constant of the cantilever. OLS is the amount of signal generated by the photodiode at a given amount of cantilever deflection. With the increasing cantilever deflection, a higher amount of signal is generated by the photodiode, hence a higher OLS value. In Asylum MFP-3D AFM system, the inverse of OLS is used, which is called InvOLS. InvOLS converts the signal (volts) into cantilever deflection (meters). Thus, the deflection can be expressed by the following equation:

$$\text{Deflection} = \text{InvOLS} \times \text{Signal}$$

Equation 3-1

By calibrating the second parameter of spring constant (k), the mechanical force F applied on the cantilever can be expressed as:

$$F = k \times \text{Deflection}$$

Equation 3-2

Therefore, the relationship between the mechanical force applied on the cantilever and the input voltage (signal) during lithography process can be expressed as:

$$F = k \times \text{InvOLS} \times \text{Signal}$$

Equation 3-3

Calibrations of InvOLS and spring constant for a specific cantilever presented in this work were done by performing a thermal tune and a fitting of the force curve in contact mode. Once both calibrations were implemented, the value of the set voltage (signal) was then calculated based on Equation 3-3.

Before doing mechanical lithography, patterns were designed by AutoCAD software and loaded into the AFM. In lithography window of AFM, the calculated value of signal was input into the field of the lithography set point. This corresponded to the cantilever deflection that would be maintained during the lithography process. By setting the tip moving direction and speed, the lithography process could start.

3.2.2 EHD printing setup

Components of EHD printing system

The EHD printing experiment was carried out by using a home-built setup which was constructed by previous group members (**Figure 3-2**). The details of each component in EHD printing system are presented in **Table 3-1**.

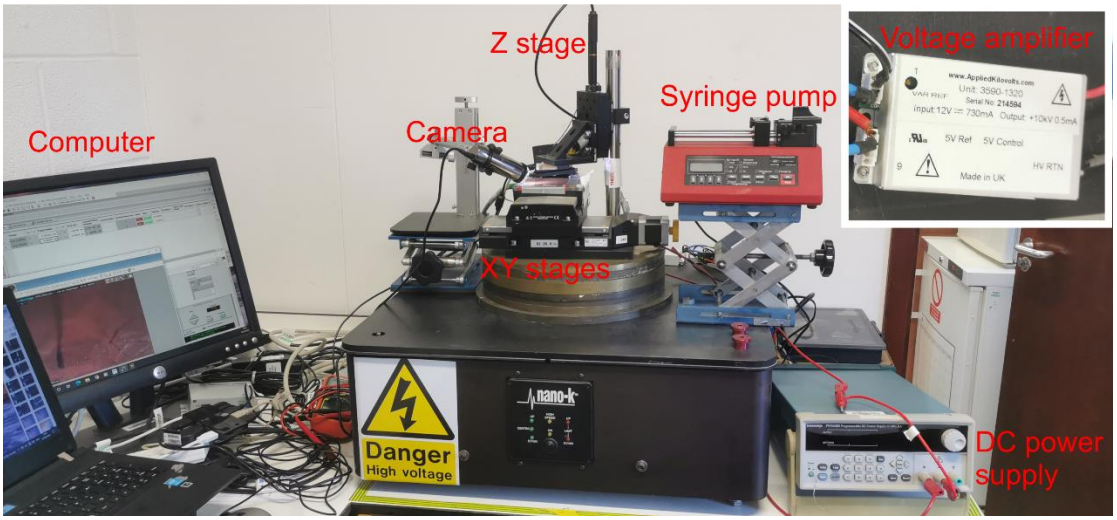


Figure 3-2 Photograph of the EHD setup, including camera, XY stages, Z stage, Syringe pump, DC power supply, voltage amplifier and computer.

Table 3-1 Details of each component in EHD printing setup

Components	Details
Tektronix PWS4205 programmable DC power supply	• Output voltage: 0–20 V • Maximum current: 5 A • Voltage output is controlled by the customised Labview programme.
Applied Kilovolts DC to DC convertor (3590-1320) (voltage amplifier)	• Output voltage: 0–10 kV • Output current: 500 µA
XY stages: Physik Instrumente L-511 High-Precision Linear Stage	• Stage is controlled by motion control software of Physike Instrumente
Z stage: Thorlabs 25 mm (0.98") Motorized Translation Stage	• Height is controlled by the customised Labview programme
Dino-Lite Edge USB microscope (AM7915MZTL)	• Dino-software is used to view/record the printing process and measure nozzle-to-substrate distance.
Syringe pump: World Precision Instruments NE-1002X	• 20 mL syringe loaded with ink is mounted on the syringe pump

Nozzle preparation

Nozzles used for the printing experiment were glass pipettes from World Precision Instruments. Various diameters of the tip from 30 µm to 1 µm were used for EHD printing experiment. Since these glass pipettes are not conductive, they were coated with an adhesive layer of 5 nm Cr and a conductive layer of 50–70 nm Au by thermal evaporation before printing. This is to ensure the application of the high electric field between the nozzle and substrate.

The Cr/Au coated tips were treated with 1H,1H,2H,2H-perfluorodecanethiol (PFDT) to make the tip surface hydrophobic. Specifically, Cr/Au coated tips were immersed into the 0.1 wt% PFDT (97% Sigma-Aldrich) in N,N-dimethylformamide (DMF) solution for 10 min[171], and then dried with a nitrogen gun. **Figure 3-3** shows that the ink accumulation on the PFDT treated tip surface is much less than the untreated one. This helps to prevent the formation of a large droplet near to the tip, hence an increase of the pattern resolution.

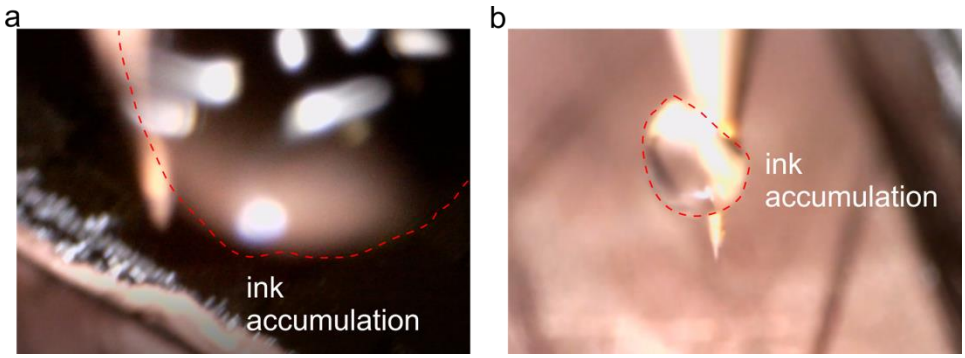


Figure 3-3 Optical images of the tips during printing of the same ink: a. A large droplet of ink accumulating near to the untreated tip. b. A smaller droplet of ink accumulating near to the PFDT treated tip.

3.3 Metrology

Many types of metrology methods were employed in this work. In addition to standard characterisation approaches such as microscopy characterisation and spectroscopic characterisation, two measurement setups of electrical measurement and photocurrent measurement were built to test the device performance.

3.3.1 Characterisation techniques

The principle and operation conditions of each characterisation approach are summarised as follows:

Microscopy characterisation:

- Optical microscopy: The principle of optical microscope is to use visible light to generate magnified images of features as fine as 1 μm via the help of various lenses

(eyepiece lens, objective lens and condenser lens). Nikon optical microscope Eclipse LV100ND and Keyence VHX-7000 Digital Microscope were used to quickly and non-destructively characterise the morphology of various features at the microscale. All optical images were taken in the bright field by using the top light without optical filters in ambient conditions.

- Fluorescence microscopy: Fluorescence microscope makes use of fluorophores which absorb photon energy at a specific wavelength and emit light at a different wavelength. The upright Zeiss LSM980 confocal fluorescence microscope was used to visualise the fluorescent secondary antibody (Invitrogen, Goat anti-Rabbit IgG-Alexa 488, stock concentration of 2 mg/mL) which was used to specifically bond with the non-fluorescent antibody of cardiac troponin I protein to confirm its presence. The laser at the wavelength of 488 nm was used to excite the secondary antibody on the specimen. Fluorescence images were captured with the 5x objective lens in ambient conditions. Parameters were set as follows:
    1) The excitation power: 5.5%.
    2) Pinhole: 4.7 µm.
    3) The detection range: 490–552 nm.
    4) The master gain: 850 V.
    5) Pixel size: 0.74 µm.
    6) 1x sampling.
    7) Pixel dwell time: 0.64 µs.
    8) Bi-directional scanning.
    9) Averaging: 4x (mean intensity) by repeating per line.
- Scanning electron microscopy (SEM): Zeiss Merlin SEM was used as the high-resolution characterisation of the surface topography and morphology at the nanoscale via the interaction between the electron beam and atoms on the sample surface. Topographic images were obtained by scanning the sample surface with a

focused electron beam and detecting the secondary electrons that are ejected from atoms of the sample surface. Due to the access limitation, SEM images were taken by group members Dr. Eugene Soh and Dr. Nikolaos Farmakidis. Parameters were set as follows for each figure:

1) **Figure 4-4**: The acceleration voltage is 10 KV and the working distance is in the range of 12.5–13 mm.
2) **Figure 4-7**, **Figure 4-9** and **Figure 4-10**a–c: The acceleration voltage is 5 KV and the working distance is in the range of 4.6–5.5 mm.
3) **Figure 4-10**d: The acceleration voltage is 10 KV and the working distance is 7.5 mm.
4) **Figure 5-1**e: The acceleration voltage is 10 KV and the working distance is 5.7 mm.
5) **Figure 5-1**f: The acceleration voltage is 10 KV and the working distance is 2.4 mm.

- Atomic force microscopy: Asylum MFP-3D AFM was used to characterise the surface topography and precisely measure the height profile with high resolution. While scanning the sample surface with a sharp tip at the nanoscale, the force interaction between the tip and sample surface leads to a deflection of the cantilever. Therefore, the sample topography can be measured via the detection of the deflection change. Tap300-G tips (BudgetSensors, 10 nm at the tip, spring constant of 40 N/m, and resonance frequency of 300 kHz) were used to scan the sample surface in the tapping mode. In the tapping mode, the cantilever is controlled to oscillate at a constant amplitude near to its resonance frequency. When the tip is in the intermittent contact with the surface, the force interaction between the tip and sample surface causes the change in the oscillation amplitude, hence giving the topography information. AFM images were processed and analysed by Gwyddion

software to do levelling, data correction and extract the height profile of the place of interest.

Spectroscopic characterisation:

- Raman spectroscopy: LabRam Aramis Raman spectrometer with 532 nm laser as the incident light was utilised to characterise the crystal structure, number of layers and strain of MoS_2. The principle of Raman spectroscopy is based on the inelastic scattering of light which is at a different wavelength from the incident light due to the interaction between light and molecular vibrations. The Raman shift is the measured energy difference between the incident light and the scattered light. The x-axis and y-axis of Raman spectrum are Raman shift and the intensity of the scattered light, respectively. The laser spot size is about 1μm × 1μm. The laser power was set as about 660 μW by adding a 10% filter in front of the laser beam. The acquisition time was set as 15 s.
- Ultraviolet–visible (UV-vis) spectroscopy: UV-vis spectrometer (Agilent Technologies Cary 8454) was used to identify the light absorption of MoS_2 dispersions, indicating the band structure of MoS_2. The principle of UV-vis spectroscopy relies on the absorption of photons in the UV or visible range by the substance in the specimen. The absorbed photon energy promotes electrons in the substance to a higher energy state. Since different bonding environments are corresponding to a specific amount of energy that can activate electrons to the higher energy state, the chemical composition and concentrate of different substances can be measured through the UV-vis spectroscopy. The spectrophotometer is a single-beam system. Therefore, a blank measurement by using the mixed solvent of water and ethanol was carried out as the reference before measuring the MoS_2 dispersion. The scanning step size of wavelengths was set as 1 nm/step.

- X-ray photoelectron spectroscopy (XPS): XPS is a surface-sensitive technique that uses a beam of x-rays to hit the sample surface and measures the kinetic energy of ejected electrons from the top 1–10 nm of the surface, hence identifying the information of elemental composition, stoichiometry and the chemical state. All elements except H and He can be detected through their characteristic photoelectron peaks shown on the XPS spectrum. XPS characterisation was carried out by Dr. Philip Holdway using Thermo Scientific K-alpha XPS. The XPS system uses monochromatic Al Kα radiation with a 50 µm spot size.

3.3.2 Electrical measurement

A home-built probe station was employed to do the electrical measurement of TFTs. As shown in **Figure 3-4**, the probe station mainly consists of a confocal microscope to image the sample, an LED light source, a movable stage where sample can be moved in XY directions and rotated by 360°, three tungsten probes (Signatone) which are connected with a semiconductor analyser (Keysight B1500A). The microscope helps to visualise the sample surface and the probe position. Tungsten probes are held by probe holders

a b

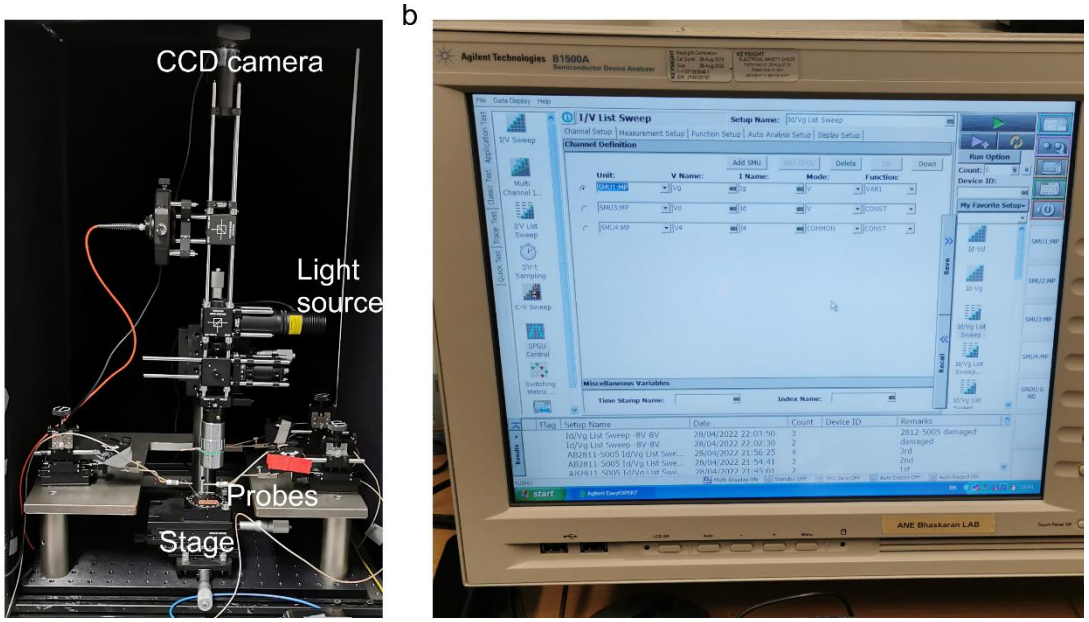


Figure 3-4 a. The photograph of the home-built probe station. b. The photograph of the semiconductor analyser.

which are capable of controlling the movement of probes in XYZ directions. By connecting three probes to source, drain and gate electrodes respectively, the output and transfer characteristics of the transistor were measured by the semiconductor analyser.

3.3.3 Photocurrent measurement

The photocurrent measurement setup was modified from the probe station. As shown in **Figure 3-5**, a 633 nm laser diode (Thorlabs, LP633-SF50, spot size ~10 μm) was integrated with the confocal microscope as the illumination source. The power of the illumination was measured by a power meter (Thorlabs PM100D) before each photocurrent measurement. Two tungsten probes were connected with a Keithley source meter 2614B which was controlled by a Labview prgramme. Photocurrent measurements under the dark and illumination were carried out using the Keithley source meter at room temperature while keeping the room light off.

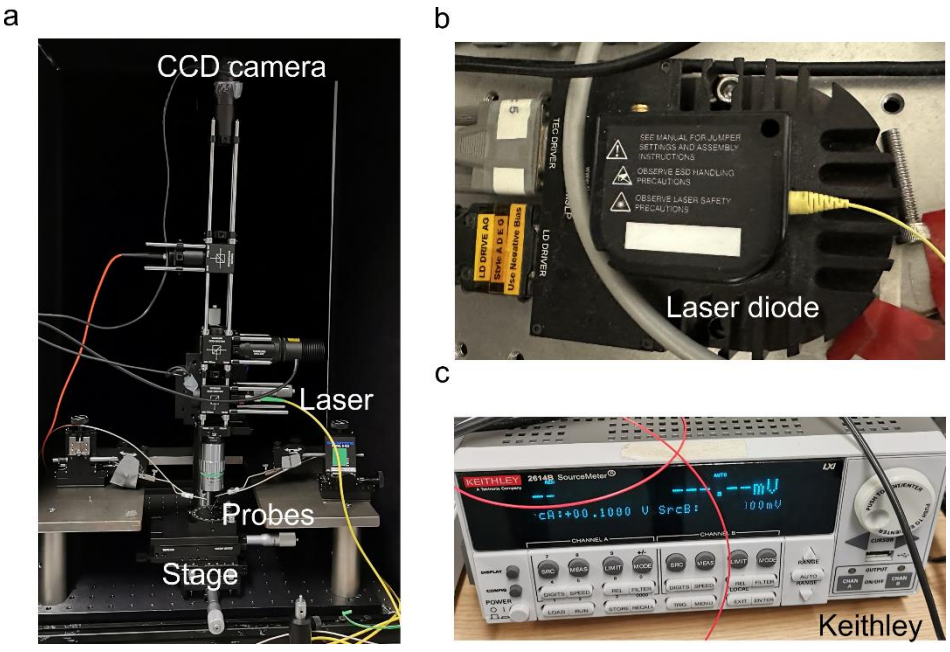


Figure 3-5 a. Probe station with laser input. b. A 633 nm laser diode. c. Keithley source meter 2614B.

Chapter 4

Water-based mechanical bilayer lithography

4.1 Introduction

Manufacturing technologies in the semiconductor industry utilise a wide range of advanced micro- and nanofabrication technologies for applications in electronics[32,100,238,239], optoelectronics[240–243], microfluidics[244–246], health care[247–250], and energy conservation[251–253]. However, over 200 high-purity organic and inorganic chemicals are used for the manufacture of semiconductor devices[254]. This presents an important challenge: that of disposing these chemical wastes properly, especially as the majority of them are harmful to human as well as the environment. Even before they are disposed of, hazardous chemicals which may contain carcinogens pose a threat to the health of workers in semiconductor factories[255–258]. Hazardous wastes also have a negative effect on our environment, potentially resulting in air, soil, and water pollution[259,260]. Thus, environmental sustainability has become a critical concern in the manufacture of high-tech semiconductor devices. Current manufacturing of high-resolution semiconductor devices primarily relies on photolithography as the patterning technique of choice. During the fabrication of these resist-based lithography techniques, development and lift-off steps utilise alkaline solutions and organic solvents as developers and strippers. These are two of the main sources of hazardous chemical waste[261,262]. The US Environmental Protection Agency developed a waste management hierarchy, which states that the most preferred approach is source reduction and reuse, followed by recycling, energy recovery, treatment and disposal[28]. Therefore, the development of a water-based manufacturing technique which limits the number of hazardous chemicals used at the source is essential to the minimisation of chemical waste. For example, Hong *et al.* have recently proposed an eco-friendly electron beam

lithography method using ice as the resist, which avoids the use of solvents during the fabrication[263].

Apart from the limitation of using hazardous chemicals, a water-based manufacturing technique which avoids radiation or electron damage could also enable a wider range of materials to be processed as functional devices, such as polymer substrates and 2DMs. Polymers are easily degraded when they are exposed to strong chemicals or radiation, and radiation damage from high-energy photons or electron beams may introduce defects in 2D materials during the fabrication process[25,114].

Without using high-energy electron-beam and photon radiation, AFM-based mechanical lithography is a relatively accessible approach to fabricate semiconductor devices in ambient conditions without the requirement of expensive cleanroom facilities. However, as it is a resist-based technique, organic solvents to remove/lift off resist are still frequently used during the fabrication process of AFM-based mechanical lithography, generating numerous hazardous waste. The use of organic solvents is also an important factor that AFM-based mechanical lithography has rarely been used to fabricate flexible devices. In addition, the difficulty to precisely keep the tip moving along the interface between the substrate surface and resist during patterning process causes the under-cutting (i.e. small forces cause the loss of pattern information) and over-cutting (i.e. large forces damage both the tip and substrate) problems. This indicates that the risk of damaging the flexible substrate by the tip exists during the fabrication process.

In this chapter, a water-based mechanical bilayer lithography process for development and lift-off has been proposed. Two layers of resist where the bottom layer of resist is water soluble are used. The goal is to enable water to act as a resist developer. While the environmental advantages of this approach are obvious in that hazardous solvents are avoided, there is also a significant functional benefit. This water-based technique protects polymer substrates from both solvent and radiation damages.

The use of bilayer resist rather than a single layer gives the advantage of the flexibility in controlling mechanical forces within a range, which improves the error tolerance. Therefore, the under-cutting and over-cutting problems can be addressed. It is no longer necessary to precisely and frequently adjust the force applied on the tip, which simplifies the patterning process. The mechanical bilayer lithography has been demonstrated to be suitable for both rigid SiO_2/Si and flexible polyethylene terephthalate (PET) substrates. It is capable of writing arbitrary patterns and reaching a resolution of 310 nm with the scope for further improvement.

4.2 **Aims of chapter**

The aim of this chapter is mainly surrounding how the water-based mechanical bilayer lithography technique is developed and its capability of writing patterns. Here is a list of aims:

- Demonstrate the water-based fabrication process of mechanical bilayer lithography.
- Explore the patterning ability of mechanical bilayer lithography including various pattern shapes and resolution.
- Demonstrate the suitability of mechanical bilayer lithography on both rigid and flexible substrates.

4.3 **Method and materials**

The fabrication process of the water-based mechanical bilayer lithography is shown in **Figure 4-1**, including the spin coating of poly(vinyl alcohol) (PVA) and poly(methyl methacrylate) (PMMA) layer, the mechanical patterning, the development in water, the deposition of metal and the lift-off in water.

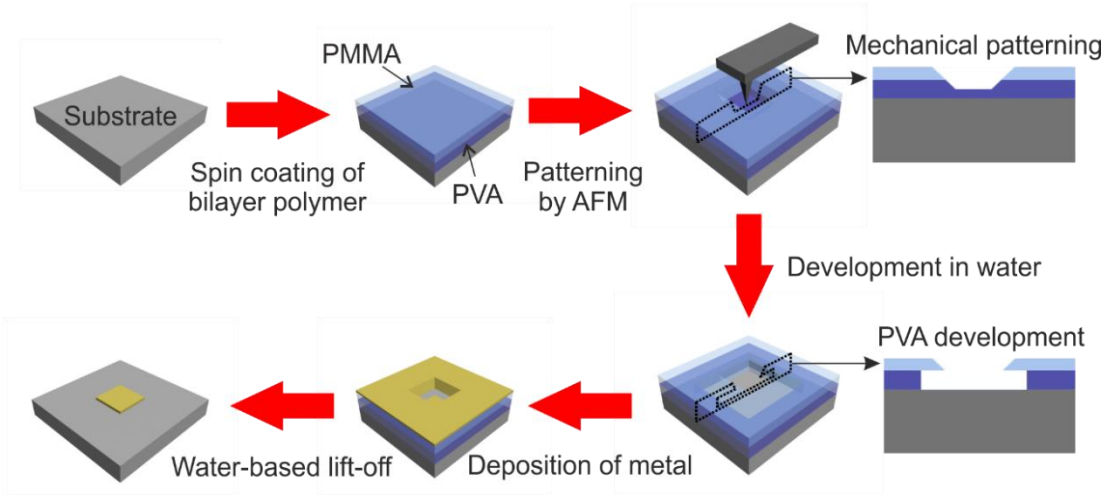


Figure 4-1 Schematic process flow of the fabrication process of water-based mechanical bilayer lithography.

4.3.1 Spin coating of PVA and PMMA Layer

For the demonstration of mechanical bilayer lithography on SiO_2/Si substrates and PET substrates, A4 PMMA (MW 495k from MicroChem) in anisole was used for spin coating. To achieve various shapes and higher resolution, A1 PMMA (MW 495k from MicroChem) in anisole was used due to its thinner thickness. PVA solution (5% w/v) was prepared by gradually dissolving PVA (Mowiol® 4-88, MW ~31000 from Sigma-Aldrich) in DI water with stirring at the temperature of 50°C overnight. A layer of PVA was spin-coated on the SiO_2/Si substrate for 30 s at 2000 rpm and heated for 10 min at 150 °C. A layer of PMMA was then spin-coated on the SiO_2/Si substrate for 60 s at 4000 rpm and heated for 10 min at 150 °C. Due to the low glass transition temperature of PET substrates, heating time and temperature after coating PMMA and PVA on PET substrates were adjusted to 70 °C and 20 min.

4.3.2 Patterning and development

All patterns were designed by AutoCAD software and loaded into an AFM (Asylum MFP-3D) before patterning. The pattering was carried out by maintaining a constant cantilever deflection. Tap300-G probes ("k = 40 N/m", Budget Sensors) with rotated tips (radius < 10 nm) were used for both AFM imaging and patterning in ambient conditions. To pattern lines with nanoscale features, the tip scanned the pattern 2–3 times. Following patterning,

DI water at a temperature of 0–5 °C was used for the development. A bottle of DI water was kept in the fridge before the development. Part of the DI water was poured into a beaker and measured the temperature using a thermometer. For development, the patterned sample was dipped into the DI water within 1 s and immediately dried with N_2 gas.

4.3.3 Deposition and lift-off

A thin film of Cr/Au was thermally evaporated at the deposition rate of 1–2 nm/s on substrates after the development. Then DI water was used for lift-off overnight.

4.4 Demonstration of fabrication process

4.4.1 Selection of bilayer resist materials

To achieve the goal of enabling water to act as a resist developer and remover, the bottom layer of resist in the bilayer structure should be able to dissolve in water. PVA was selected because it is a water-soluble synthetic polymer which is widely available and low-cost. Due to its biocompatibility, low cytotoxicity and biodegradability, it has a variety of applications in biomedicine, biomaterials, pharmacy and food industry[264]. The chemical formula of PVA is $[CH_2CH(OH)]_n$ (**Figure 4-2**). The synthesis of PVA is based on the partial/complete hydrolysis of polyvinyl acetate[265]. Its water solubility highly depends on the degree of hydrolysis. The optimum solubility is 87—89% acetate hydrolysis[266]. The PVA selected in this work has relatively low molecular weight of 31,000 and 86.7—88.7 mol% hydrolysis. Thus, it is applicable to completely dissolve in water while heating at a moderate temperature such as 50℃. PVA has good film-forming

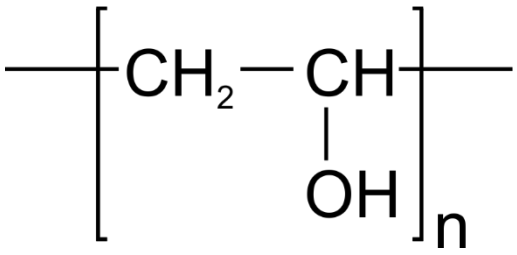


Figure 4-2 Structural formula of PVA.

property and insolubility in oil and most organic solvents[267], which enables another advantage as the bottom-layer resist of being little affected by the coating of the top layer of resist.

The material for the top layer of resist was selected as the commonly used PMMA due to its easy accessibility and good processability to form uniform films. By adjusting the concentration and molecular weight, the thickness of spin-coated PMMA can be thinned down to sub-50 nm, which helps to reduce the amount of resist residue piled up around the pattern during the tip writing. PMMA is insoluble in water so that water has little influence on it. Furthermore, PMMA has good thermal stability and biocompatibility, which enables many biomedical applications such as clinical dentistry and drug delivery[268,269].

In summary, PVA and PMMA were chosen to be spin-coated on the substrate as the bilayer structure of resist.

4.4.2 Optimisation of fabrication process

Figure 4-1 illustrates the bilayer lithography process. Two layers of resist, a top layer of PMMA and a bottom layer of PVA, were utilised. Patterns were written on the bilayer resist by applying sufficient force to penetrate through to the bottom PVA layer. It is unnecessary to remove the entire PVA layer during patterning as subsequent development using water can remove the unpenetrated PVA; this enables the process to be more tolerant in the application of force.

Flexibility to control mechanical force

As mentioned before, one advantage of this technique is the flexibility to control the mechanical force applied on the AFM tip. Single-layer resist used in conventional AFM-based mechanical lithography requires precise control of the mechanical force to avoid over-cutting and under-cutting problems. In this process, however, patterns are written in the PVA layer without the need to remove the entire PVA layer. Thus, the mechanical

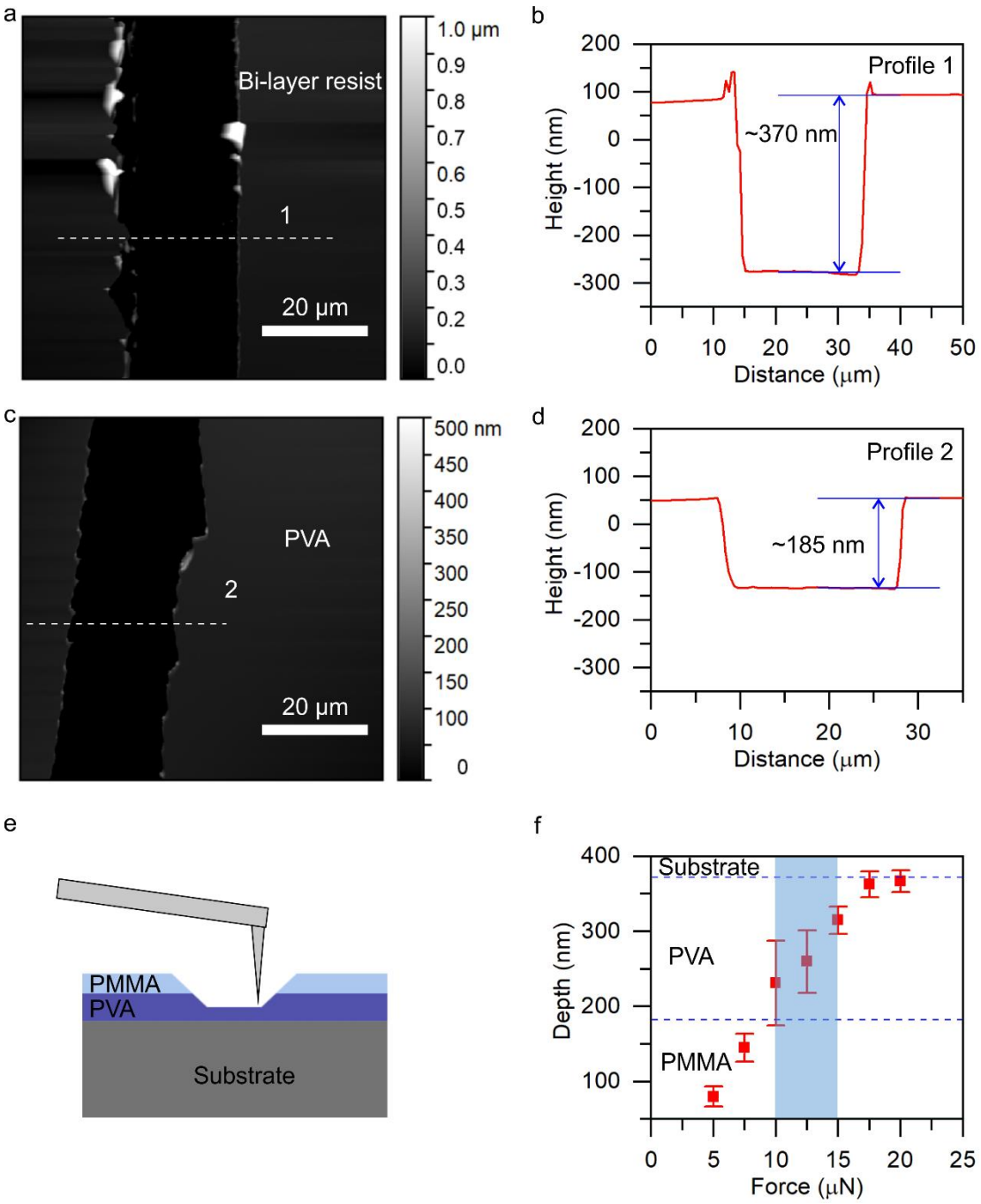


Figure 4-3 Investigation of mechanical forces that should be applied on the tip. a. AFM image of bilayer resist with a gap. b. Height profile of the dashed line 1 in a. c. AFM image of PVA with a gap. d. Height profile of the dashed line 2 in c. e. Schematic diagram of the AFM tip patterning. f. Force vs depth curve obtained by using gradually increasing mechanical forces and measuring the corresponding depth after patterning.

force applied can be flexibly selected within a range, which allows for good error tolerance.

To investigate this, the thicknesses of the A4 PMMA and PVA layers were measured by spin-coating both layers of resist and only PVA layer on different substrates, respectively.

AFM height profile results show that the thicknesses of the bilayer resist and PVA layer are 370 nm and 185 nm, respectively. This indicates that the thickness of both A4 PMMA and PVA are about 185 nm (**Figure 4-3**a-d).

With the known thickness of each layer, the gradually increasing mechanical forces from 5 µN to 20 µN were used to pattern the bilayer resist, and the corresponding depths after patterning were measured. By repeating the experiment for 3 times, the average depth with the corresponding standard deviation was calculated for each mechanical force, thus obtaining the force vs depth curve with the error bar. The force vs depth curve (**Figure 4-3**f) shows that the best mechanical forces can be selected in a relatively wide range from 10 µN to 15 µN. For forces < 10 µN, the tip does not penetrate the PMMA layer. For forces >10 µN, the tip cuts through PMMA layer and begins to mechanically pattern the PVA layer. When the mechanical force reaches 15 µN, the tip starts to interact with the SiO_2/Si substrate. Thus, for a given thickness of PMMA and PVA, the applied force can be flexibly selected (ranging from 10 µN to 15 µN in this case), allowing for robust patterning over a large area.

Instead of frequently adjusting the mechanical force applied on the tip to keep it constant in conventional AFM-based mechanical lithography, the bilayer structure simplifies the patterning process by allowing the mechanical force vary in a proper range. Compared to the phase-mode AFM-based mechanical lithography proposed by Liu *et al.* where the AFM system is modified by integrating with a piezoceramic disk to monitor the vertical position of the tip while patterning[125], this approach enables a more straightforward and affordable way to realise the same goal without the need to modify the AFM system.

In addition, the tip is controlled to mechanically pattern the PVA layer without contacting the substrate, which greatly reduces the wearing damage to the tip. **Figure 4-4**a and **Figure 4-4**b compare a new and a used tip. The used tip is still sharp, although some polymer residues remain around the tip after patterning as seen using SEM. These

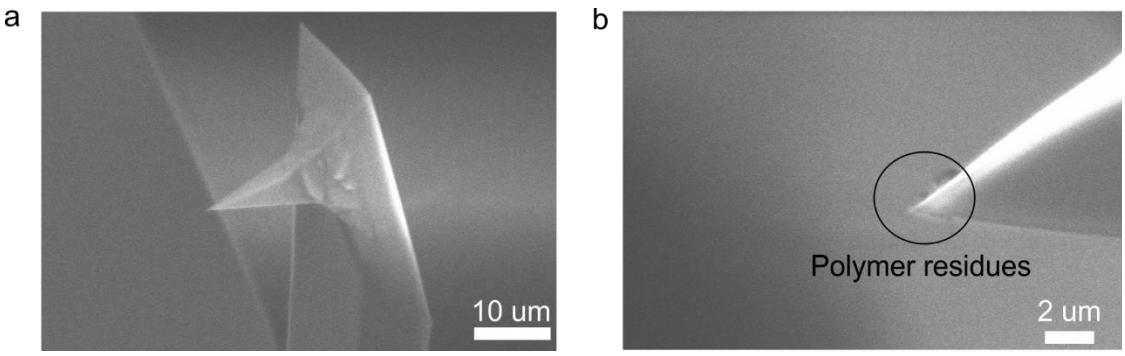


Figure 4-4 a. SEM image of a new tip. b. SEM image of a used tip.

residues are readily removed in acetone and water, and the tip can be reused to do patterning.

Development in water at the temperature of 0–5 °C

For the development, since PVA is soluble in water whereas PMMA is not, the patterned area allows the water to dissolve the remaining PVA without affecting the PMMA. However, the rate of development of PVA in room-temperature water is faster than reasonable timescales achievable. Following the mechanical patterning of an array of squares in the PVA layer, the development in water at the room temperature led to the structural collapse of the bilayer resist which is shown as purple rings in **Figure 4-5**. Even though the development time was reduced from 9 s to 2 s, structural collapse still occurred due to the excessive development of unparterned PVA layer. The excessive development of PVA leads to the weak support of PMMA, resulting in the loss of pattern information after the lift-off.

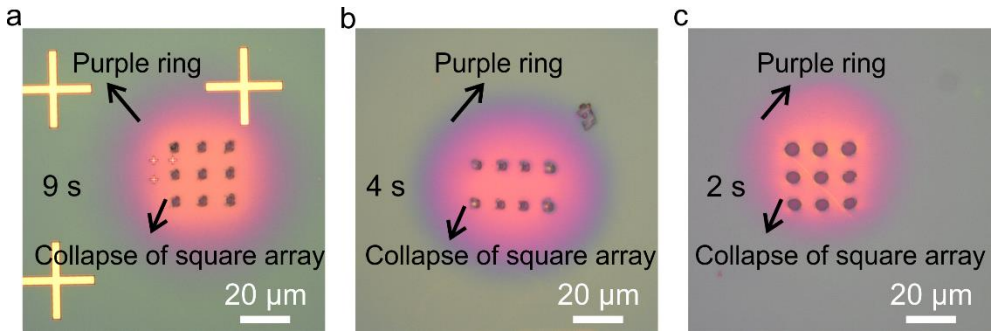


Figure 4-5 Structural collapse of the bilayer occurs during the development in room-temperature water: a. for 9 s. b. for 4 s. c. for 2 s.

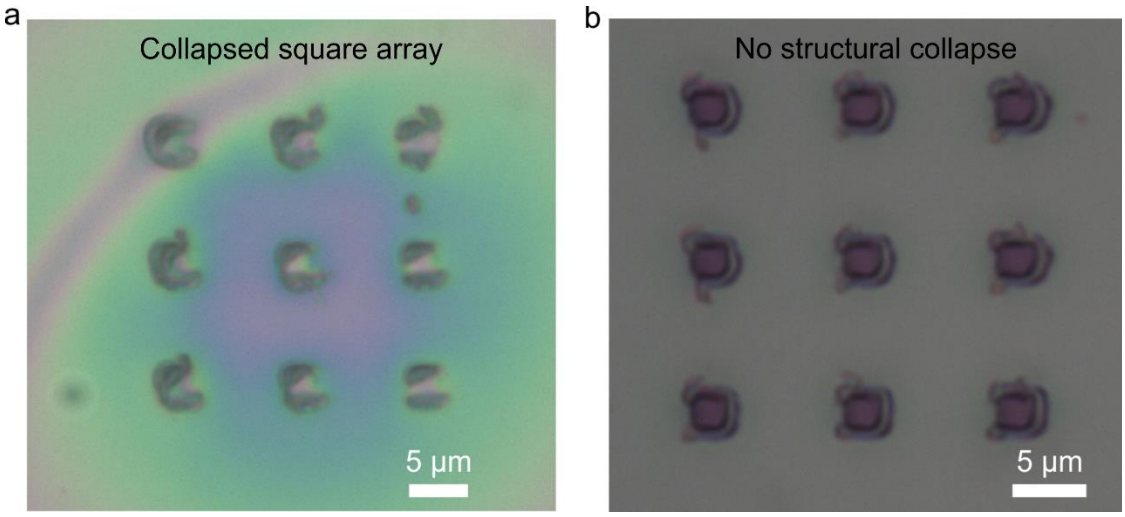


Figure 4-6 Comparison between proper development and improper development. a. Optical image of square patterns after improper development. Structural collapse occurred due to the development of unpatterned PVA. b. Optical image of square patterns after proper development.

To decrease the dissolution rate of PVA in water, cold water in the temperature range of 0–5 °C was used to avoid overdeveloping for timescales of ~1 s, followed by promptly drying the sample using nitrogen gas. Since the decrease of water temperature reduces the kinetic energy used for the dissolution reaction, this decreases the solubility of PVA in water. By this means, the problem of structural collapse was effectively addressed as demonstrated by the disappearance of purple rings (**Figure 4-6**b).

Further confirmation of the avoidance of structural collapse was done by observing the cross section of patterned bilayer structure after proper development. **Figure 4-7** confirms that PMMA overhangs above the PVA after the development of the remaining PVA on the patterned area. This validates that the low temperature decreases the

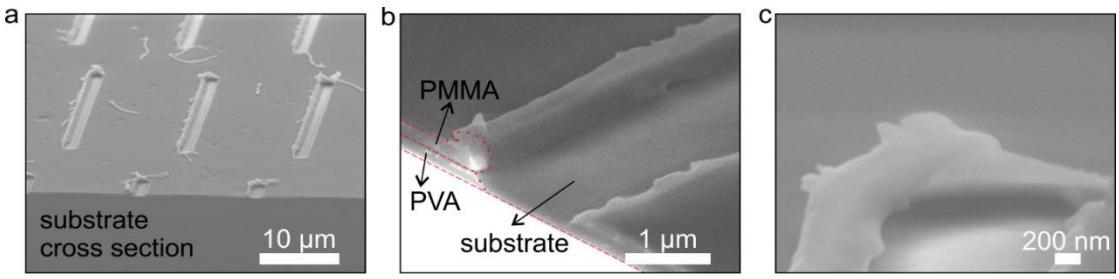


Figure 4-7 Cross section of bilayer structure after development. a. SEM image of the cross section under lower magnification. b. SEM image of the cross section under higher magnification. c. SEM image of the pattern which shows the overhanging structure.

dissolution rate of PVA in water, which enables a proper development. These parameters were tested to be suitable for developing patterns with different dimensions on both SiO_2/Si and PET substrates.

After optimising each step of the mechanical bilayer lithography process, an example is given here showing images of the pattern after going through each step (**Figure 4-8**). The demonstration was done on the rigid SiO2/Si substrate. The pattern is a combination of a 30 × 20 μm rectangle and a triangle with the longest edge being 20 μm. After mechanical patterning of the bilayer resist, much of the PVA layer remains, so the surface appears relatively rough compared to that in the unpatterned area, and the motion of the nanoscale tip in the form of straight lines from right to left is observed (**Figure 4-8**a). The removed resist is piled up on the left side of the pattern due to the preset patterning direction.

Following development in low-temperature water, the underlying substrate is exposed. The smoothness of the area following this step is shown in Figure 4 8b, which demonstrates that the roughness of the patterning is not a material issue for the lithography process. This underlines the tolerance of the lithography process to variations of the mechanical force. The metal lift-off process was then carried out. The lift-off pattern was defined by depositing 5 nm Cr and 50 nm Au via the thermal evaporation (**Figure 4-8**c), with lift-off carried out by overnight immersion in water. The metal pattern thus obtained is shown in **Figure 4-8**d, validating the mechanical bilayer lithography approach.

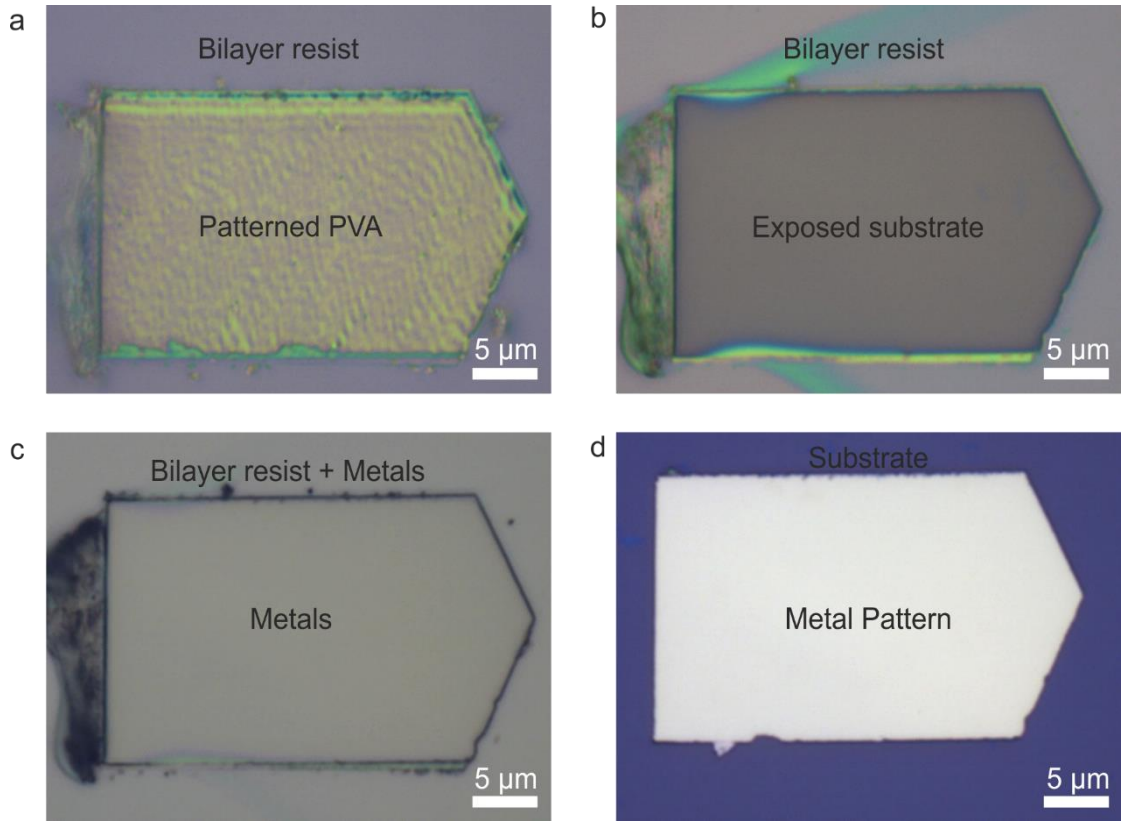


Figure 4-8 Optical images of an electrode pattern after key steps, including a. mechanical patterning of the bilayer resist, b. water-based development, c. metal deposition prior to lift-off, and d. metal electrode after lift-off.

4.5 Write patterns with high resolution and various shapes

4.5.1 High resolution

The resolution of the mechanical bilayer lithography technique has then been investigated. As PMMA overhangs above the PVA window opened after the development of the remaining PVA on the patterned area (**Figure 4-1**), the pattern written by the tip in PMMA layer actually determines the resolution of the final pattern transferred on the substrate. With the increasing thickness of PMMA layer, it is more likely to cause the structural collapse due to the heavier PMMA overhanging above the PVA after development, which may decrease the resolution. In addition, a thicker PMMA layer leads to more amount of resist residue piled up on the edge of the pattern after the tip patterning, which may cause the issue of pattern discontinuities. Therefore, a thinner PMMA layer is favourable to achieve higher resolution.

In the above-mentioned experiment for demonstrating the mechanical bilayer lithography, A4 PMMA which formed a layer with the thickness of 185 nm by spin-coating was used. Owing to the advantage of the wide adjustable range of the thickness of spin-coated PMMA resist, the concentration of PMMA was decreased to A1 to minimise the thickness of PMMA layer. By using the same spin-coating recipe as A4, the thickness of coated A1 PMMA layer was reduced to sub-50 nm.

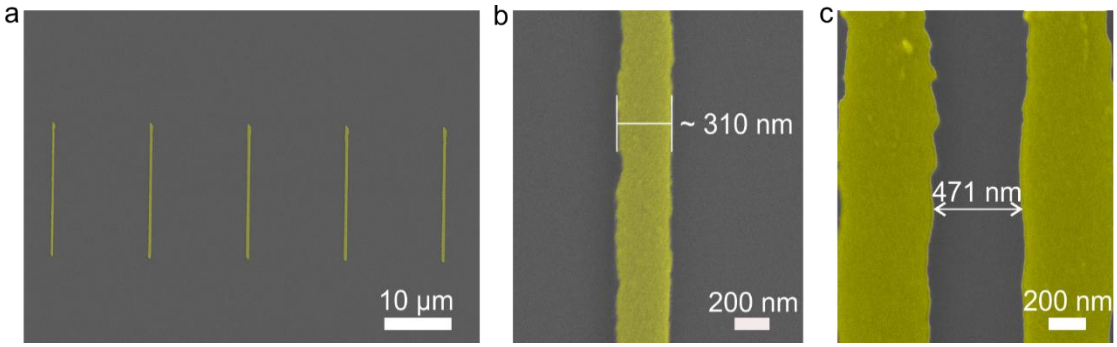


Figure 4-9 High-resolution patterns on SiO_2/Si substrates fabricated by bilayer lithography. False-coloured SEM micrographs of a. line patterns, b. highest resolution line pattern, demonstrating an achievable line width of 310 nm, c. spacing of 471 nm between two patterns.

With the thinner PMMA layer, patterns with high-resolution were written using this technique. **Figure 4-9**a shows an array of 20 µm long line patterns that was patterned onto SiO_2/Si substrates. The line width, as small as 310 nm can be achieved using this technique as shown in **Figure 4-9**b, without any observable resist residue around the line pattern. **Figure 4-9**c shows the minimum spacing between two patterns using our technique to be 471 nm, indicating excellent line-spacing capability in addition to the high resolution.

The patterning width is also determined by the tip as it acts as the tool to write patterns[270,271]. The dimension and shape of the tip significantly affect the patterning width. It is possible to further improve the resolution by using sharper tips. Although the tip used in this work has the minimum radius of about 10 nm, the pyramidal shape of tip makes its cross section greatly increase when it is farther from the minimum radius point of tip,

resulting in a wider patterning width. Thus, tips with a high aspect ratio can further increase the resolution of patterns in the mechanical bilayer lithography.

In addition to the thickness of the PMMA layer and the tip, further optimising parameters of the development time and temperature is helpful to achieve higher resolution. The development with timescale of ~ 1s in this work was done manually, which really depends on the reaction and operational speed of the person. Further optimisation can be automating the development process so that the development time can be preset to a proper value and kept constant for all experiments. Alternatively, doing development using water vapour may also solve the problem of the rapid dissolution rate of PVA, making this process more controllable. Additionally, optimising the mechanical force is also a solution to a higher resolution as it determines the vertical position of the tip while writing in the bilayer resist.

4.5.2 Various shapes

To demonstrate the adaptability of this technique to create arbitrary microscale patterns, a circle, a triangle and a ring were patterned using this technique on SiO_2/Si substrates. 5 nm Cr and 20 nm Au were subsequently deposited on the substrate, followed by lift-off. SEM images of a circle with a radius of 5 μm, an equilateral triangle with sides of 10 μm, and a ring with the two radii differing by 2 μm are shown in **Figure 4-10**a–c, respectively, demonstrating that this technique can also fabricate structures with different shapes. **Figure 4-10**d presents a further array of square patterns with an average side length of 1.8 μm, formed by the deposition of 10 nm Cr and 20 nm Au. The topography of each pattern was characterised by AFM after lift-off. The average thickness of all square patterns is around 30 nm, which is consistent with the deposition parameters (**Figure 4-10**e–f). The variation of the thickness in each pattern is within 5 nm. This indicates that bilayer lithography can achieve uniform surface topography of multiple patterns.

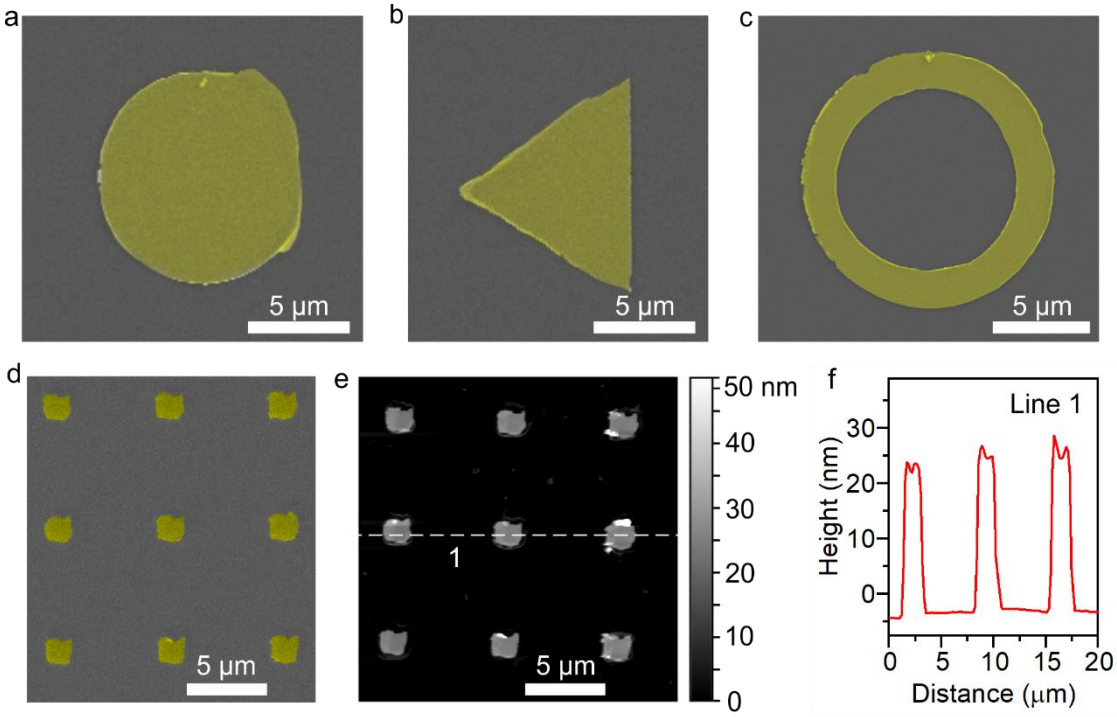


Figure 4-10 Patterns with various shapes written by mechanical bilayer lithography. False-coloured SEM micrographs of a. a circular pattern, b. a triangular pattern, and c. a ring pattern. d. SEM image of nine square patterns. e. AFM scan of these square patterns. f. Height profile of the dashed line marked in e.

4.6 Patterning on polymer substrates

The suitability of this patterning technique on flexible substrates was also investigated. Given that the mechanical bilayer lithography can accommodate changes to substrate topography, combined with the force tolerance of this technique as described previously, this technique is well suited to flexible substrates. Combined with the potential to eschew solvent use during development, it would allow one to use flexible substrates, such as PET, that are not compatible with hazardous processes.

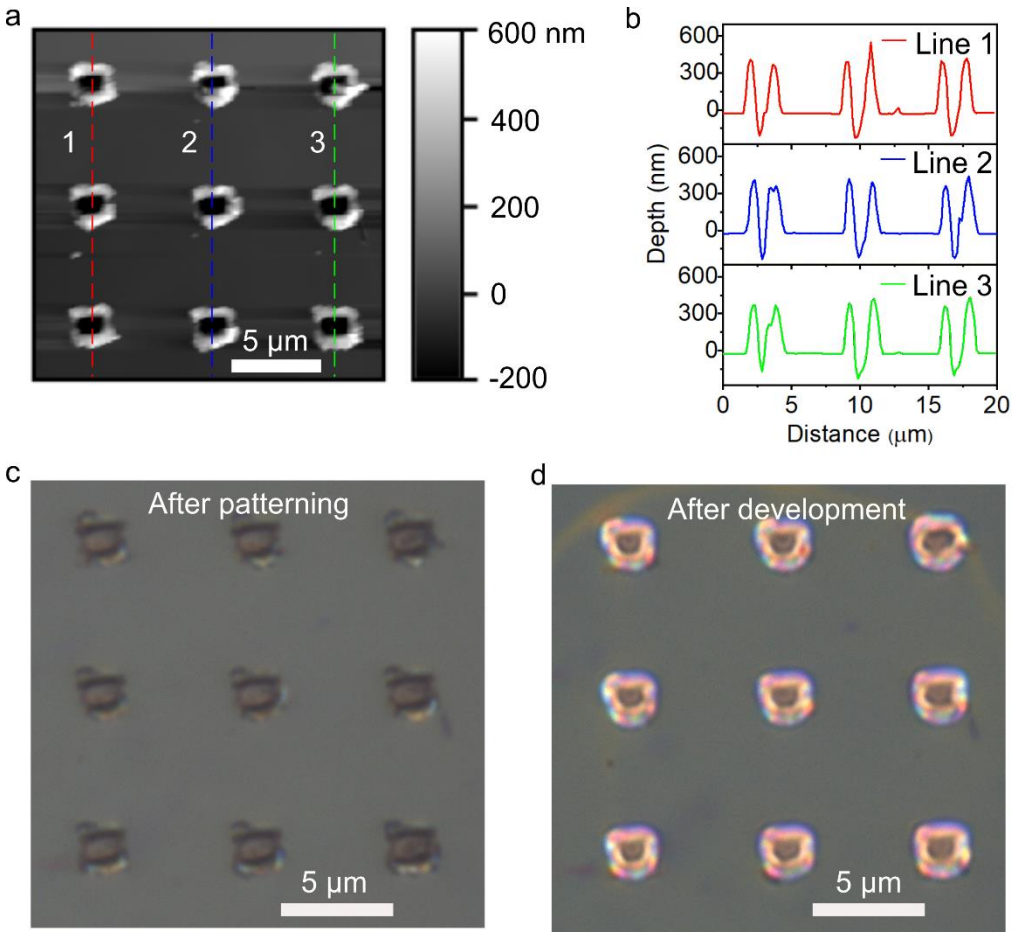


Figure 4-11 Square patterns on PET substrates at different stages of the fabrication process. a. AFM image of square patterns after patterning. b. Height profiles of the dashed lines in a. c. Optical image of square patterns after patterning. d. Optical image of square patterns after development in water.

As PET substrates are too soft to handle during the fabrication process, they were adhered on glass substrates before the spin-coating of the bilayer resist. PVA and A4 PMMA layers were spin-coated on PET substrates, and an array of square patterns was written into the bilayer (**Figure 4-11**c). To demonstrate the flexibility of controlling mechanical forces applied on the tip, mechanical forces of 10, 11, and 12 μN were applied from the left to the right column sequentially during patterning. The depth profile shows that the average depth is ~216 nm (**Figure 4-11**a, b). The measured depths prior to development do not increase with the increasing applied force, which is attributable to resist residues around the tip during patterning, leading to less precise depth profiles.

Deposition of metals on PET substrates is different from SiO_2/Si substrates because of the poor adhesion between metals and polymers caused by their low wettability[272]. To

improve their adhesion, the PET substrate was treated with O_2 plasma before the deposition of 5 nm Cr and 20 nm Au. After lift-off, all patterns were obtained even though different mechanical forces were used for each column, underlining the robustness of this technique to mechanical force.

Figure 4-12a shows the PET substrate onto which the square patterns were deposited. The height profiles indicate that the mean length of each side of the squares is 0.93 µm and the mean thickness of each pattern is 25 nm, which is in agreement with the deposition parameters (**Figure 4-12**b, c). The thickness at the edge of each pattern is slightly higher than 25 nm because of the high roughness of PET substrates, which results in a worse lift-off than that on the smoother SiO_2/Si substrates; this could be improved in future experiments via the use of ultrasmooth substrates. Regardless, the technique works very well on flexible substrates.

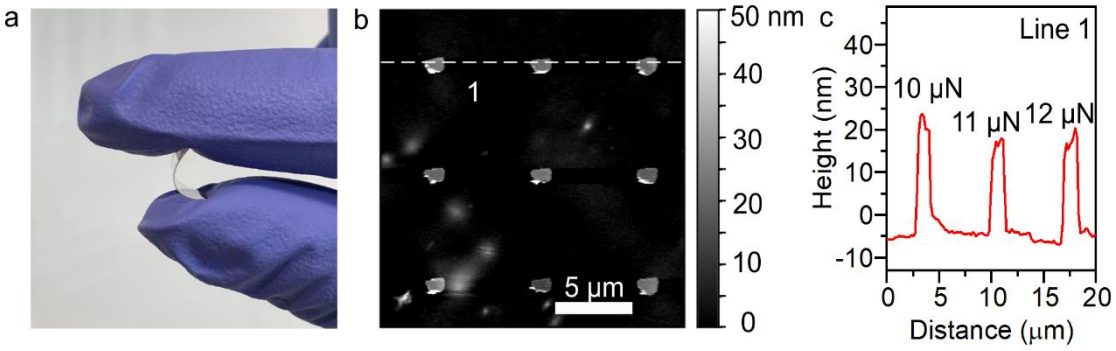


Figure 4-12 Square patterns on PET substrates. a. A photo of a PET substrate with square patterns of Cr and Au. b. AFM scan of these square patterns on the PET substrate. c. Height profile of the dashed line marked in b.

4.7 **Limitation**

In spite of the advantages of the flexibility in the application of mechanical force and the water-based process which is compatible with flexible substrates and minimises the use of hazardous chemicals, this technique still has one limitation of the low throughput. The AFM system used in this work allows a maximum speed of writing patterns at 20 µm/s which is relatively slow compared to other patterning techniques, resulting in the time-consuming drawback as well as a low throughput. The reason for the disadvantage of

low scalability is that the design of AFM system and the tip are mainly for the purpose of imaging the surface topography with high resolution. The slow scanning speed of the tip is required by the interaction between the tip and substrate surface for characterising the surface topography.

The limitation of the low throughput also exists in other SPL techniques. There are some feasible solutions that have been proposed to address the limited throughput. A high-speed AFM system has been developed recently and has the capability of imaging the surface topography at an enhanced speed, which may improve the pattern writing speed as well[273,274]. Another effective solution to improving the throughput is patterning in parallel by using functional probe arrays[275]. Salaita *et al.* have demonstrated to write the same nanoscale structures in parallel with the 55000 cantilever array, which significantly saves fabrication time[276]. The parallelization with proper spacing between two adjacent probes ensures the independent patterning with no interrupt between each probe. As the resolution is determined by the geometry of the tip, the use of probe arrays can still keep the fine feature size while enhancing the throughput.

The mechanism of the parallelization can also be applied into the mechanical bilayer lithography technique to improve the throughput. The use of parallel probe arrays can enable large-area patterning compared to the current maximum patterning area of 90 × 90 μm by a single tip in this work. Since it has already been demonstrated to fabricate and image nanostructures with arbitrary shapes by integrating 5 probe arrays with the commercial AFM system[277], the compatibility of such probe arrays with the commercial AFM system will be even higher in the future. Furthermore, the independent control of each probe by separate actuator will make the patterning process more effective as each probe may accomplish different patterning jobs simultaneously.

4.8 Sustainability analysis

The mechanical bilayer lithography technique employs water as the developer and remover. The replacement of organic solvents with the safe solvent of water promotes the sustainability of this technique according to the first piece of 12 principles of green engineering “inherent rather than circumstantial”. The use of non-hazardous materials decreases the harm of their corresponding waste to both the environment and human. To fabricate a 10 cm × 10 cm layer using this technique, about 200 mL water is needed for the development and lift-off in total. The used water can be recovered and reused for the next time. Compared with using high-energy electron beam or photons as the patterning tool in conventional lithography techniques, the employment of the tip to write patterns in ambient conditions lowers the energy cost. However, the development in cold water at the temperature of 0–5 ℃ consumes more energy, which can be potentially improved by replacing cold water with water vapour.

4.9 Conclusions

In summary, a water-based mechanical lithography approach that exploits a bilayer resist structure consisting of the water-soluble PVA and water-insoluble PMMA has been demonstrated. The use of water for development and lift-off helps to minimise the hazardous chemical waste at the source, leading to a more sustainable technique. Crucially, this also adds process functionality because the technique enables protection of polymer substrates from solvent-based damage.

The water-based fabrication approach is suitable for patterning on both SiO_2/Si and PET substrates. This technique can achieve arbitrary patterns with a demonstrated line resolution down to 310 nm. There is significant scope to improve this using sharper probes, and further optimisation of parameters such as the thickness of PMMA layer, tip geometry, tip material, development time, water temperature, and mechanical force would significantly improve achievable resolution and quality. Further investigation into

the highest achievable aspect ratio is required to understand the potential applicability of this technique.

The limitation of low throughput in this technique can be effectively addressed by employing functional probe arrays. This solution enables a highly efficient way to simultaneously pattern many same structures in large area while keeping a high resolution.

4.10 Author contributions

I carried out most of the experimental work. The initial concept of the bilayer resist was conceived by Dr. Ben Porter. He also did initial experimental work to demonstrate the feasibility of the bilayer structure. SEM characterisation was done with the help of Dr. Eugene Soh and Dr. Nikolaos Farmakidis.

Chapter 5

Fabrication of flexible MoS_2 photodetectors

5.1 Introduction

Transition metal dichalcogenides (TMDs) are one important group of the 2DMs family which have outstanding electrical and optical properties that have attracted great interest from the scientific community. The thickness-dependent band gap of TMDs and weak screening effect have enabled a wide range of applications in electronics (e.g. FETs and memristors)[278–280], optoelectronics (e.g. LEDs and photodetectors)[281–283], sensors[284–286] and energy storage[287,288].

Many studies have reported the distinct impacts of strong radiation and chemical doping on TMDs. However, both are being used in conventional fabrication process (e.g. photolithography or electron-beam lithography) of TMDs-based devices based on rigid substrates. The construction of functional structure based on TMDs on flexible polymeric substrates is more complicated due to the low chemical resistance and radiation-induced degradation of polymeric substrates. Although some polymeric substrates with relatively higher chemical resistance can be processed by photolithography, there still exist an adverse effect on the device performance. Indeed, the common fabrication approach for flexible TMDs-based devices is by transferring prefabricated devices on rigid substrates to flexible polymeric substrates to avoid such damage.

The water-based mechanical bilayer lithography technique has been demonstrated in the previous chapter. Since this technique minimises the use of organic solvents and requires no photon or electron-beam radiation, it is expected that devices fabricated by this method should outperform their counterparts fabricated by conventional lithography techniques.

In this chapter, the further demonstration of using this technique to fabricate a flexible MoS_2 photodetector has been described. To build the flexible MoS_2 photodetector, two low-cost approaches have been explored to prepare MoS_2, including liquid exfoliation and mechanical exfoliation. The liquid-exfoliated MoS_2 dispersion was employed as the ink material for EHD printing. The preparation and printability of MoS_2 ink which avoids using toxic solvents have been demonstrated. However, the flake size of MoS_2 prepared by this method is too small, which is not suitable to fabricate a photodetector. Therefore, mechanically exfoliated MoS_2 has been prepared for the fabrication of the photodetector by mechanical bilayer lithography. The fabricated flexible MoS_2 photodetector shows photoresponsivity of 29 mA/W and photoswitching speed of 42 ms under a laser illumination of 633 nm wavelength, showcasing the applicability of this technique to making functional devices.

5.2 Background

5.2.1 Radiation effects and chemical doping of TMDs

Currently the fabrication of TMDs-based functional devices mainly relies on photolithography and electron-beam lithography. The fabrication process exploits high-energy electron-beam or photon radiation, which brings negative effects on the performance of TMDs-based functional devices by the creation of defects in both TMDs and substrates. Defects created in the substrate is attributed to the ionization of atoms under the exposure of strong radiation[113]. Silicon chips with the dielectric layer of SiO_2 are widely used as substrates in the semiconductor industry. However, SiO_2 can be ionized to trap holes at the interface with TMDs, leading to a shift of the threshold voltage in the corresponding transistor[114]. Furthermore, the radiation effect can cause an increase in the number of chalcogenide vacancies such as sulfur vacancies in MoS_2 and WS_2, which creates more trapping states within the band gap of TMDs and results in the decrease in the carrier mobility.

In addition to radiation effects, the commonly used organic solvents during the fabrication process of TMDs-based devices can also affect the electrical and optical properties of TMDs via the doping effect. Choi *et al.* have studied the chemical doping effects of various solvents on the change in carrier density of monolayer MoS_2 and WSe_2. Depending on the relative difference in electronegativity between organic solvents and TMDs, the immersion in different solvents results in either the photoluminescence (PL) enhancement or quenching due to the charge transfer between the solvent and TMDs[112]. For example, if the chemical that interacts with n-type monolayer MoS_2 is electron-withdrawing, the charge transfer from MoS_2 to the chemical will lead to an increase in the exciton formation, thus showing an enhanced PL intensity[289].

Therefore, the monitor of radiation effects and chemical doping during the fabrication process are critical to construct TMDs-based functional devices with superior performance.

5.2.2 Exfoliation of MoS_2

MoS_2 is a typical semiconducting TMDs material and suitable for electronic and photonic applications due to its thickness dependent bandgap, the transition from indirect band gap to direct band gap at monolayer thickness and a large on/off current ratio[290].

Compared to MoS_2 thin films grown by chemical vapor deposition which requires specific equipment to control various parameters such as temperature and flow rate, exfoliation of bulk MoS_2 enables a simple and low-cost approach to prepare MoS_2 thin films. Exfoliation method can be divided into mechanical exfoliation and liquid exfoliation. Due to the weak van der Waals interaction between each layer of MoS_2, a bulk crystal can be mechanically exfoliated through scotch tape peeling into MoS_2 thin films and even single-layer or few-layer MoS_2[290]. With no chemicals involved in the preparation process, the strong covalent bond within each layer of MoS_2 enables a good conservation of the lateral structure after exfoliation, hence a high-quality thin film. It is a rapid and effective

method which has greatly reduced the time and cost for the preparation of MoS_2, but the thickness of the exfoliated MoS_2 thin film varies in a wide range. Therefore, the yield of MoS_2 thin films with the specific thickness is rather small, leading to a low scalability.

Liquid exfoliation has been developed to address the low yield of mechanical exfoliation. The most common method of the liquid exfoliation of MoS_2 is employing bath/probe sonication to exfoliate MoS_2 powder dispersed in a proper solvent with a certain concentration. A good solvent in liquid exfoliation is important. It is studied that the liquid exfoliation of MoS_2 is more prone to occur when the surface energy of solvent is close to that of MoS_2, because this corresponds to a small net energetic cost [291–293]. The surface energy of MoS_2 is about 46.5 mJ/m^2 [294]. N-methyl-2-pyrrolidone (NMP) with surface energy of 40 mJ/m^2 is a widely used solvent to exfoliate MoS_2 due to the matched surface energy[295]. Therefore, the use of NMP with no assist of surfactant can obtain few-layer to monolayer MoS_2 dispersions with a high concentration after exfoliation[296]. Other solvents such as dimethyl sulfoxide (DMSO) and dimethylformamide (DMF) have also been found to be suitable for liquid exfoliation of MoS_2[291]. However, such organic solvents have relatively high boiling point, leading to the difficulty to fully remove the solvent after exfoliation[297]. Furthermore, electrical and optical properties of MoS_2 may be changed due to the chemical doping by these strong solvents. Their toxicity makes the corresponding chemical waste have an adverse impact on the environment. Therefore, such liquid exfoliation methods employing strong organic solvents are less sustainable for long term.

Alternatively, less hazardous solvents such as ethanol and isopropyl alcohol (IPA) are also used for liquid exfoliation of MoS_2. They have lower boiling point and no remaining residue. They are usually used in the form of a mixture with water due to the challenge of dispersing MoS_2 in pure ethanol/IPA or pure water. Zhou and coworkers have demonstrated that the use of a mixture of 45 vol% ethanol/water as the solvent can achieve 2–4 nm MoS_2 nanosheets[298]. Such solvent-mixture strategy enables a more

cost-effective and sustainable approach to exfoliate MoS_2 into few-layer nanosheets. However, MoS_2 can still be doped, resulting in the property change.

Currently, the liquid exfoliation of MoS_2 gives more opportunities to fabricate functional devices. The liquid-exfoliated MoS_2 has been used as the ink material in direct printing techniques such as inkjet printing and aerosol printing[15,299–301], but the exploration of the use of such exfoliated MoS_2 is still lacking. Thus, more investigation into the application of exfoliated MoS_2 in EHD printing is needed.

5.3 Aims of chapter

The main aims of this chapter are building a flexible MoS_2 photodetector by using the mechanical bilayer lithography and comparing the device with its counterpart fabricated by conventional photolithography. Here is a list of aims:

- Prepare MoS_2 thin films by exploring two approaches which are EHD printing of liquid exfoliated MoS_2 and mechanical exfoliation of bulk MoS_2.
- Demonstrate the applicability of mechanical bilayer lithography to fabricate functional devices by building a flexible MoS_2 photodetector.
- Compare the performance of the device fabricated by mechanical bilayer lithography with its counterpart fabricated by conventional photolithography.

5.4 Methods and materials

5.4.1 EHD printing of liquid exfoliated MoS_2

Liquid exfoliation of MoS_2

30 mg MoS_2 powder (~6 μm, Sigma-Aldrich) was added into 10 mL of a mixture of 45 vol% ethanol/water. The dispersion was sonicated in a bath sonicator for 5 days, and then was centrifuged at 8000 rpm for 20 min to remove aggregates and unexfoliated MoS_2.

EHD printing of MoS_2 ink

30 Gauge dispensing capillaries with the inner diameter of 150 μm (Adhesive Dispensing Ltd) were used for EHD printing. The applied voltage and distance between the nozzle and the substrate were set to 1 kV and 250 μm, respectively. The velocity of the stage varied from 5 mm/s to 8 mm/s.

5.4.2 Mechanical exfoliation of MoS_2

A bulk MoS_2 crystal (Ossila) was mechanically exfoliated into a thin film of MoS_2 by Scotch-tape cleavage approach. The exfoliated thin film was subsequently transferred onto the PET substrate using PDMS stamp.

5.4.3 Characterisation of MoS_2

Liquid Exfoliated MoS_2

SEM was used to characterise the flake size of MoS_2 before and after sonication. The liquid exfoliated MoS_2 dispersion was characterised by UV-vis spectroscopy. Raman spectroscopy and AFM were used to characterise the thickness of EHD printed MoS_2.

Mechanical Exfoliated MoS_2

Optical microscope, Raman spectroscopy and AFM were used to characterise the topography and thickness of exfoliated MoS_2 transferred on PET substrates.

5.4.4 Fabrication of flexible MoS_2 photodetectors

Water-based mechanical bilayer lithography

A1 PMMA (MW 495k from MicroChem) in anisole was used to pattern electrodes on PET substrate for the MoS_2 photodetector. Other fabrication parameters are consistent with details shown in chapter 4.

Photolithography

Microposit S1813 photoresist was spin-coated on PET substrate at 3000 rpm for 1 min, followed by the heating at 115 ℃ for 1 min. Mask aligner (SUSS Micro Tec MKB4) was used for patterning electrodes. After exposure, the sample was developed in MF319 for

1 min. A thin layer of Cr/Au was thermally evaporated on the substrate after the development. Acetone was then used as the remover to lift-off the remaining photoresist.

5.4.5 Device measurement

A home-built photocurrent measurement setup (**Figure 3-5**) was used to test the flexible photodetector. I-V curves of the photodetector in dark and under illumination at the wavelength of 633 nm were measured. The photocurrent under different illumination powers, photoresponsivity as well as the photoresponse time of the photodetector were also measured and analysed.

5.5 Preparation of MoS_2

Two approaches have been explored to prepare MoS_2 thin films including EHD printing of liquid exfoliated MoS_2 and dry transfer of the mechanically exfoliated MoS_2. The average thickness of printed flakes is about 3.8 nm, and the average lateral width and length are 63 nm and 65 nm, respectively. Building two electrodes for the photodetector on such a small $MoS2_2$ flake is difficult because the line-spacing capability of mechanical bilayer lithography beyond the flake lateral dimension. In comparison, the lateral dimension of dry transferred MoS_2 flakes varies from a few tens of micrometer to several micrometers. The thickness also varies from monolayer to sub-100 nm. Due to the bigger flake size and less chemical influence, the mechanically exfoliated MoS_2 thin film was eventually used to fabricate the flexible photodetector.

5.5.1 EHD printing of liquid exfoliated MoS_2

The bulk MoS_2 used for liquid exfoliation is black powder (**Figure 5-1**a). Its dispersion before sonication looks very dark (**Figure 5-1**b). The SEM image shows the lateral size of MoS_2 flake is up to 2 μm before sonication (**Figure 5-1**e). After 5 days' sonication, the colour of MoS_2 dispersion becomes lighter than before, which indicates the presence of exfoliated MoS_2 (**Figure 5-1**c). The further centrifuge makes the colour of the supernatant dispersion even lighter, confirming the removal of thick flakes as well as

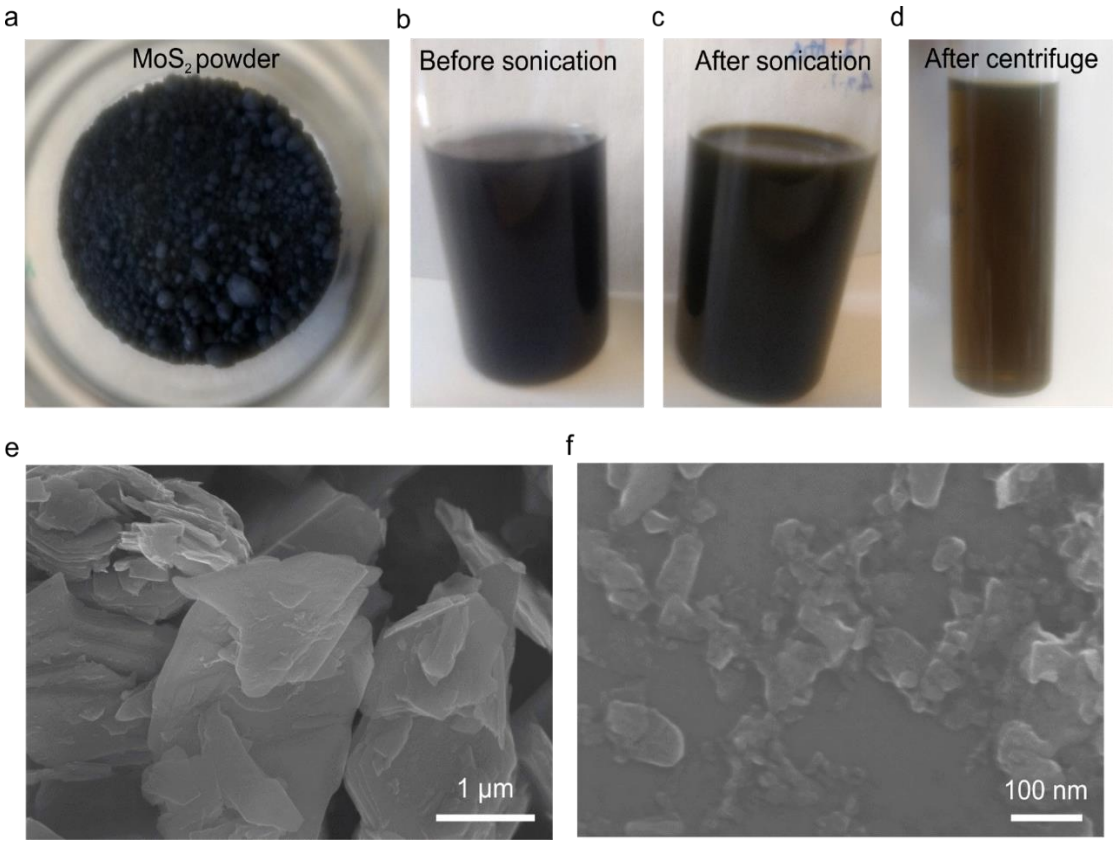


Figure 5-1 Photographs of a. Bulk MoS_2 powder, b. MoS_2 dispersions before sonication, c. MoS_2 dispersion after sonication, d. MoS_2 dispersion after centrifuge. e. SEM image of MoS_2 dispersion before sonication. f. SEM image of exfoliated MoS_2.

unexfoliated MoS_2 (**Figure 5-1**d). The SEM image shows that the average lateral size of exfoliated MoS_2 is 100 nm or less, which is about one order of magnitude smaller than that before sonication (**Figure 5-1**f).

The light absorption spectrum through UV-vis spectroscopy showing the optical properties of MoS_2 dispersions after exfoliation can be observed in **Figure 5-2**a. The characteristic A peak and B peak are located at 616 nm and 678 nm, respectively. The two peaks confirm the presence of MoS_2 nanosheets in the ethanol/water mixture. The Raman spectrum (**Figure 5-2**b) of exfoliated MoS_2 shows that the E_{2g}^1 and A_{1g} modes are around 383.1 cm^{-1} and 407.4 cm^{-1}. The energy difference of 24.3 cm^{-1} between two modes indicates more than 4 layers of exfoliated MoS_2 nanosheets. As the laser spot size of the Raman spectroscopy is about 1 μm but the flake size is just 100 nm or less, the measured spectrum may be the sum of spectra from multiple MoS_2 nanosheets. As the Raman signal from the thicker-layer nanosheet is much stronger than that from the

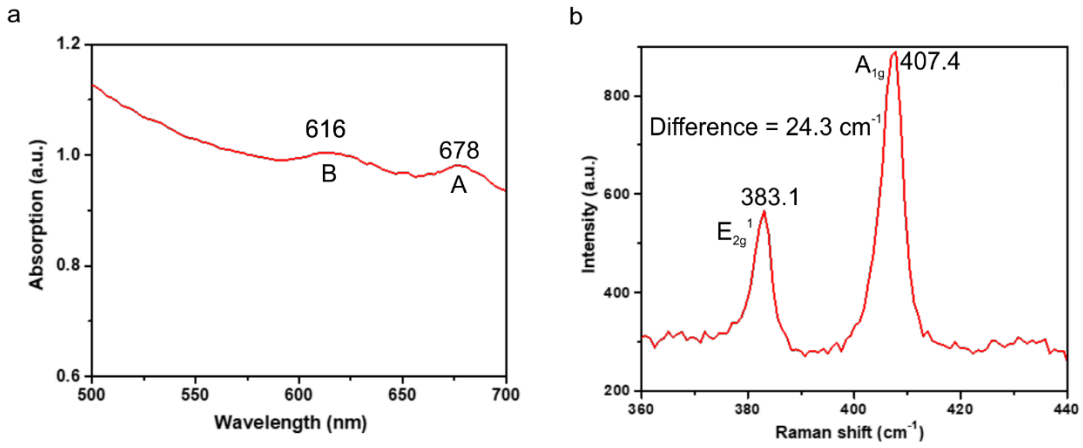


Figure 5-2 a. UV-vis spectrum of exfoliated MoS_2 dispersions. b. Raman spectrum of exfoliated MoS_2 nanosheets.

thinner-layer nanosheet, the measured spectrum tends to present dominant signal of the thick-layer MoS_2 nanosheets rather than the thinner ones. This results cannot exclude the possibility of the existence of less than 4 layers of MoS_2 nanosheets.

The exfoliated MoS_2 dispersion was subsequently used as the ink in EHD printing. Without adding a back pressure, the MoS_2 dispersion was printed out into lines when the tip-substrate distance, voltage and stage velocity were 250 μm, 1 kV and 5 mm/s, respectively (**Figure 5-3**a). Therefore, the printability of MoS_2 dispersion has been demonstrated. The linewidth is bigger than the inner diameter of capillary and not so consistent between each part in one line because of the low viscosity of MoS_2 dispersion in the mixture of ethanol/water. The quick flow rate of ink makes the jet unstable, leading to rough lines.

In order to print finer lines, the stage velocity was varied from 5 mm/s to 8 mm/s, provided that the nozzle diameter, ink properties, the applied voltage and the distance between the nozzle and substrate were fixed. Optical images of printed lines under different speeds are presented in **Figure 5-3**a–d. As the stage velocity increases to 8 mm/s, there are more discontinuities in the line. Only at the speed of 5 mm/s, a continuous line could be printed. At a higher moving speed, the feeding speed of the ink that has been printed out is slower than the moving speed, resulting in a more discontinuous line.

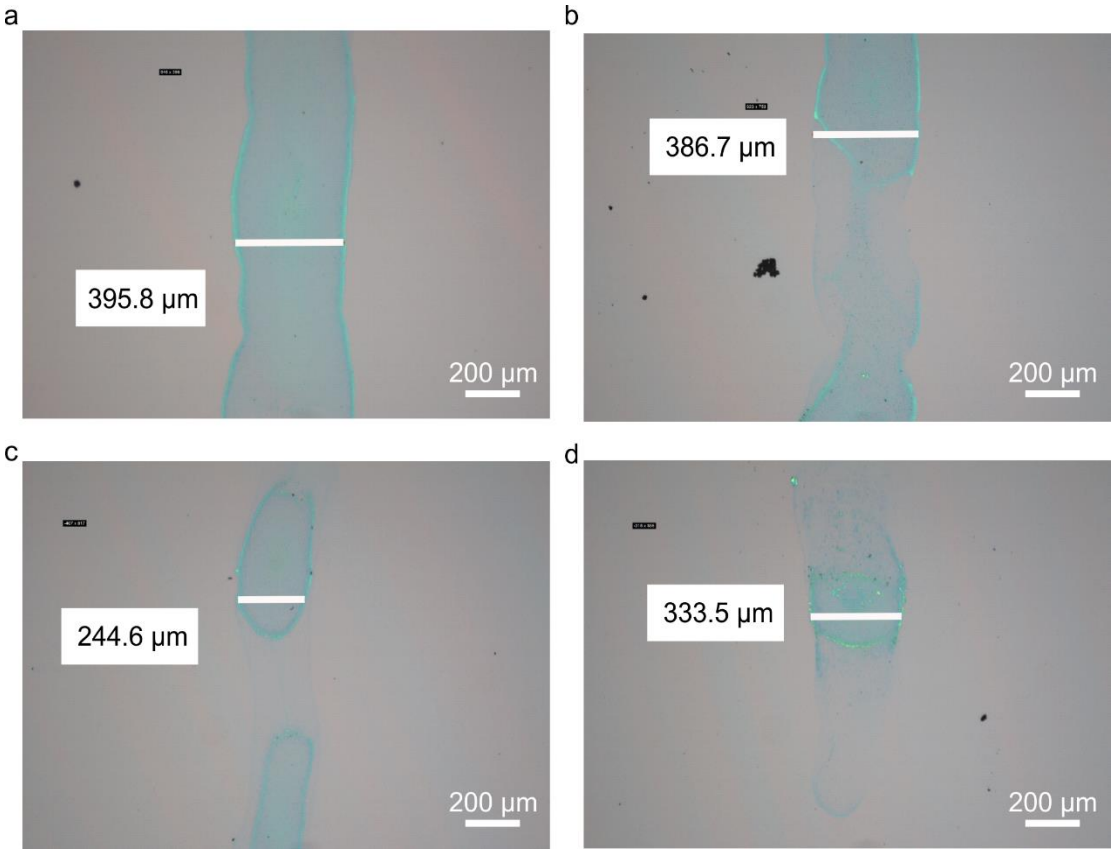


Figure 5-3 Optical images of EHD printed lines at different velocities of the stage: a. 5 mm/s, b. 6 mm/s, c. 7 mm/s, d. 8 mm/s.

As the most uniform line was corresponding to 5 mm/s, further characterisations were based on this velocity. The morphology of printed MoS_2 nanosheets was characterised by AFM. **Figure 5-4**a shows that most printed MoS_2 nanosheets are widely distributed despite several aggregated clusters. It can be observed that a continuous thin film is not formed due to the disconnected nanosheets. Statistical analysis of the three dimensions of MoS_2 nanosheets was carried out based on information of 50 nanosheets obtained by AFM characterisation. The width of these nanosheets varies from 20 nm to 220 nm with the average value of 63 nm (**Figure 5-4**b), while their length covers a broader range from 20 nm to 300 nm with the average value of 65 nm (**Figure 5-4**c). The thickness of these nanosheets is 1–12 nm, ranging from monolayer to multi-layer (**Figure 5-4**d). The average thickness is 3.8 nm corresponding to 4–5 layers of MoS_2. The statistical results indicate that the lateral dimension of printed MoS_2 nanosheets is quite small despite the

more consistent thickness with each nanosheet. The too small lateral dimension makes these nanosheets not suitable for fabricating photodetectors.

Raman spectroscopy was carried out to further confirm the presence of MoS_2 and the thickness. It can be found that the E_{2g}^1 and A_{1g} modes are located at 381.3 cm^{-1} and 406.1 cm^{-1} (**Figure 5-5**). The energy difference of 24.8 cm^{-1} between two modes

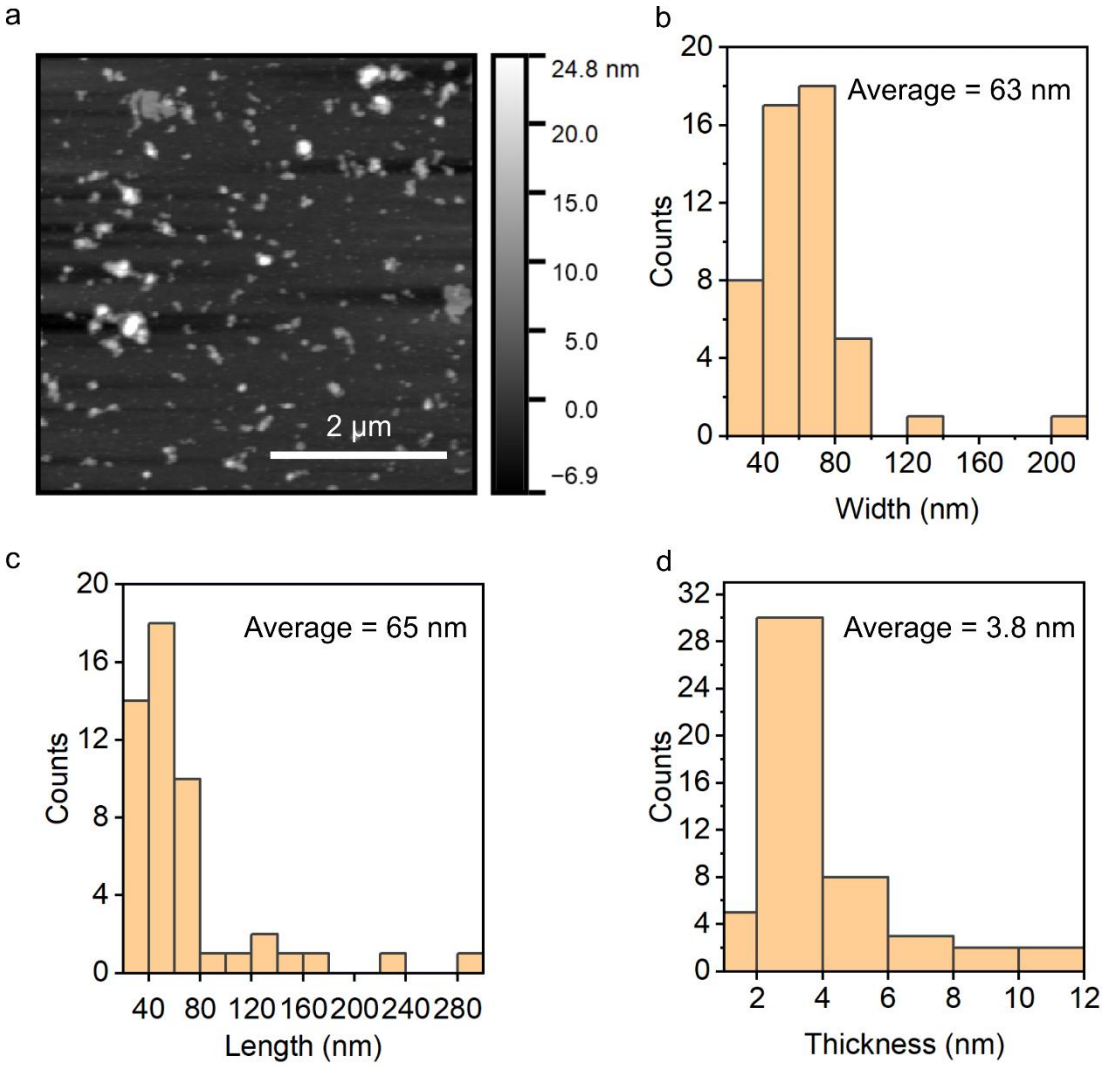


Figure 5-4 a. AFM image of the printed MoS_2 nanosheets. Statistical analysis of three dimensions of printed nanosheets: b. width, c. length, d. thickness.

indicates more than 4 layers of MoS_2, which is consistent with the Raman results of the exfoliated MoS_2[302]. The thickness indicated by Raman results also agrees with the statistical analysis of the thickness of MoS_2 nanosheets, because the statistical result

shows that among 50 measured nanosheets, the majority of them (38 nanosheets) have the thickness ranging from 2 nm to 6 nm, corresponding to 3–8 layers.

5.5.2 Mechanical exfoliation of MoS_2

As the average lateral size of printed MoS_2 nanosheets is too small, it is advantageous

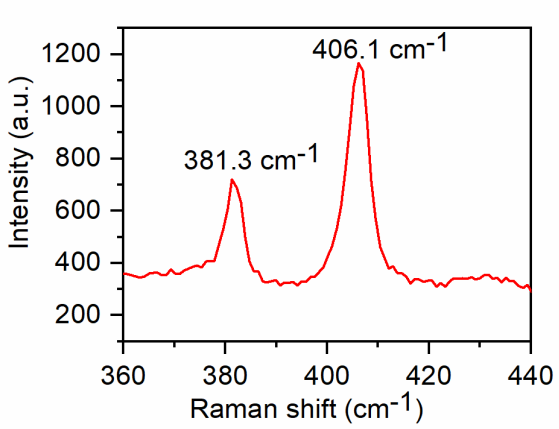


Figure 5-5 Raman spectrum of printed MoS_2

to use the method of mechanical exfoliation by peeling off bulk crystal into thin films and transferring exfoliated thin films on PET substrates by PDMS stamps. In spite of a big difference of the thickness between each flake, the lateral flake size is rather big. Furthermore, the preparation process involving no chemicals makes itself more suitable for the fabrication of the photodetector.

The exfoliated multilayer film for the photodetector is presented in **Figure 5-6**a. The thin film is similar to a rectangle with the width of about 6 µm and length of 55 µm. Raman spectrum (**Figure 5-6**b) shows that the energy difference between $E_{2g}{}^1$ mode (381.98 cm^{-1}) and A_{1g} mode (407.56 cm^{-1}) is 25.58 cm^{-1}, indicating multilayer MoS_2. This has been confirmed by AFM scanning of the thin film. The height profile presents that the thickness of the thin film is about 78 nm (**Figure 5-6**d). This MoS_2 thin film was then used for the fabrication of the flexible photodetector by the mechanical bilayer lithography.

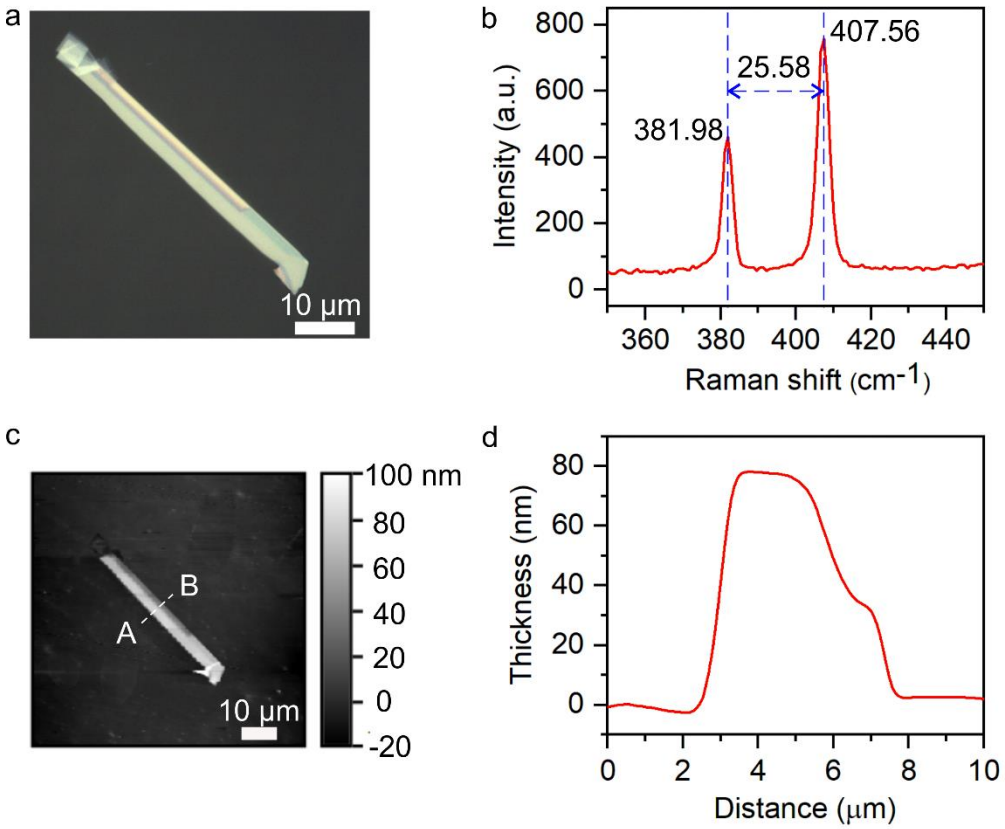


Figure 5-6 MoS_2 thin film transferred onto the PET substrate. a. Optical image of MoS_2 thin film transferred on the PET substrate before patterning. b. Raman spectroscopy of MoS_2 thin film on the PET substrate. c. AFM image of MoS_2 thin film on the PET substrate. d. Height profile of the dashed line AB in c.

5.6 Flexible MoS_2 photodetectors

To further explore practical applications of water-based mechanical bilayer lithography, this technique was used to fabricate a flexible MoS_2 photodetector on the PET substrate. As a comparison, a similar flexible photodetector was also fabricated by conventional photolithography. Both techniques were used to pattern Au electrodes on the MoS_2 thin film that was pre-transferred on the PET substrate.

5.6.1 Fabrication by mechanical lithography

The fabricated flexible MoS_2 photodetector device (**Figure 5-7**a, b) was characterised by measuring the current (I) through MoS_2 channel under the dark and 633 nm laser source with different illumination powers ranging from 10 μW to 35 μW. The current (I) shows a linear relationship with small voltages (V) supplied to photodetector, indicating an ohmic response (**Figure 5-7**c). The device also demonstrates a clear response to a

633 nm laser. As can be seen from **Figure 5-7**d, the photocurrent at V = 1 V exhibits a sublinear increase with increasing incident power.

The photoresponsivity is defined as

$$R = \frac{I_{ph}}{P_{light}}$$

Equation 5-1

where I_{ph} is the photocurrent and P_{light} is the incident light power. **Figure 5-7**e shows the photoresponsivity under various incident light powers from 10 μW to 35 μW acquired at the supplied voltage of V = 1 V. The photoresponsivity and incident light power exhibit negative correlation, because at higher illumination power the increasing photo-generated carriers lead to the saturation of trap states. The highest photoresponsivity measured was 29 mA/W at an incident light power of 10 μW.

The time-resolved photoresponse was further investigated by switching the illumination on and off. The current through MoS_2 channel jumps to a high value when the illumination is turned on, and recovers immediately to near the dark current level when the illumination is turned off (**Figure 5-7**f). The calculated response time of the MoS_2 photodetector is about 42 ms, which compares favourably with values from other reports[241,303,304]. This is attributed to the reduction of surface trap states on the MoS_2 channel, further demonstrating the advantages of using the environmental-friendly bilayer lithography method. It can be noted that an overall trend of increasing current in the dark current during the measurement mainly due to the laser-induced heating effects[146]. As the thermal conductivity of PET is very low (about 0.15 W m^{-1} K^{-1}) compared to that of other silicon substrates such as SiO_2 (about 1.3 W m^{-1} K^{-1}), the heating effects become more prominent for MoS_2 photodetectors on PET substrates[146].

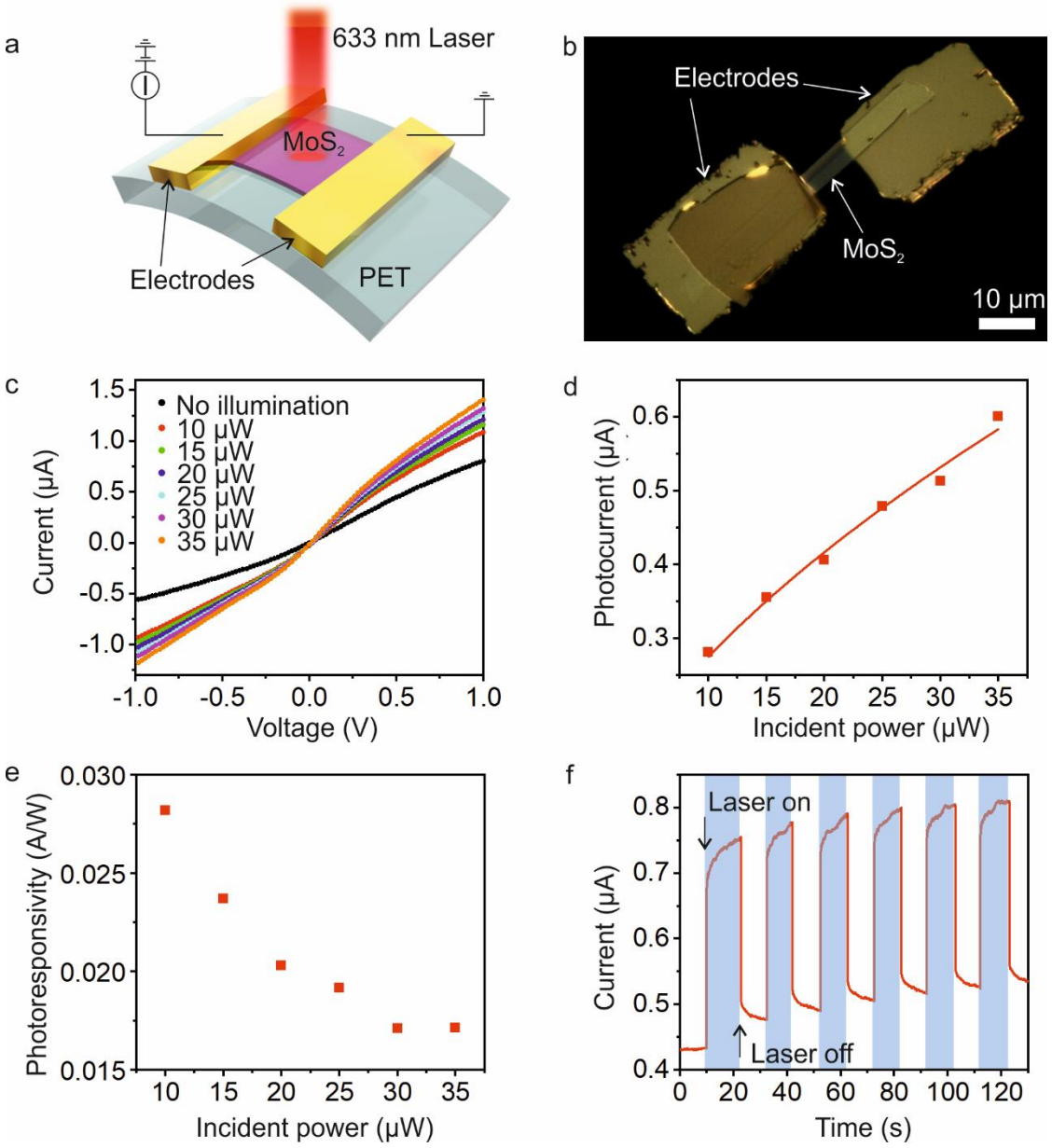


Figure 5-7 Flexible MoS_2 photodetector device. a. Schematic diagram of the flexible MoS_2 photodetector. b. Optical image of the flexible MoS_2 photodetector. c. I-V curve of the photodetector in the dark and under different illumination powers. d. Photocurrent of the photodetector under different illumination powers for V = 1 V. e. Photoresponsivity of the MoS_2 photodetector. f. Time-resolved photoresponse of the photodetector for V = 0.5 V and an illumination power of 38 μW. The calculated response time is 42 ms.

5.6.2 Fabrication by photolithography

To further confirm the advantage of the flexible MoS_2 photodetector fabricated by the water-based mechanical bilayer lithography, conventional photolithography was used to fabricate a similar flexible photodetector as the use of organic solvents and photon radiation may have an adverse impact on both MoS_2 and the PET substrate.

The flexible photodetector fabricated by photolithography is presented in **Figure 5-8**a. It is impossible to obtain two exactly the same MoS_2 thin films by mechanical exfoliation. However, the thickness of the selected MoS_2 thin film for photolithography is about 70 nm which is quite similar to the one (78 nm) used in mechanical bilayer lithography (**Figure 5-8**b, c). The distance of about 10 µm between two patterned electrodes was kept consistent in both fabrication techniques.

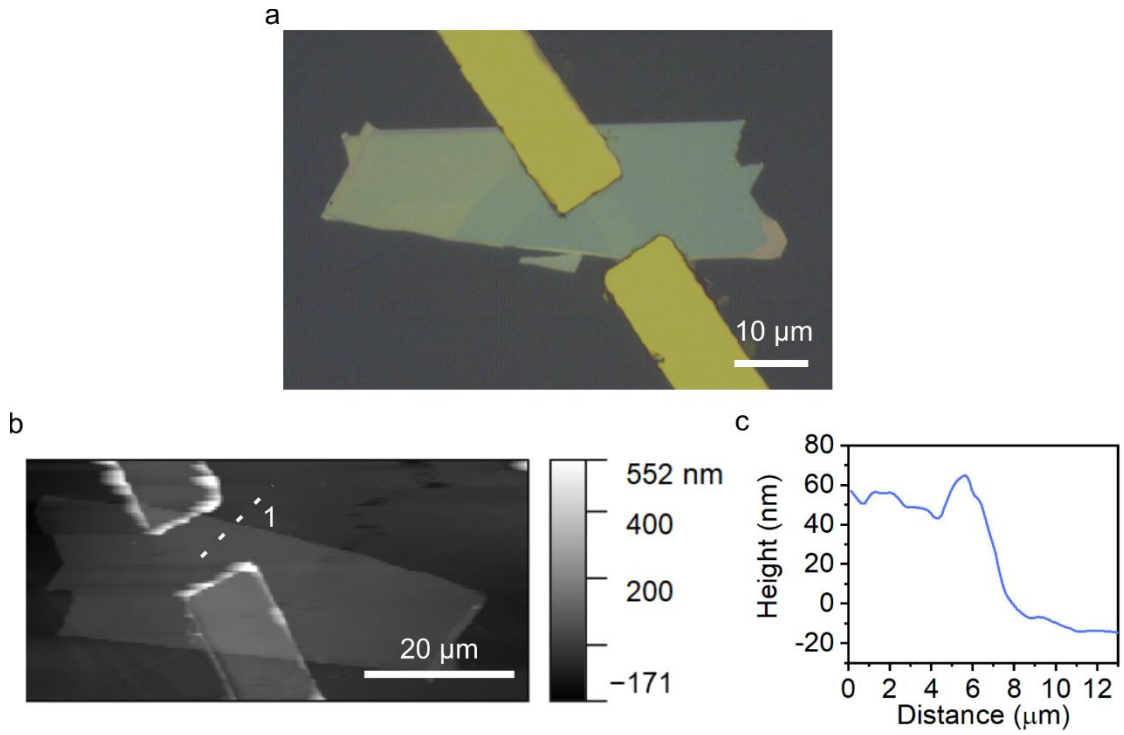


Figure 5-8 a. Optical image of the flexible MoS_2 photodetector fabricated by photolithography. b. AFM image of the flexible MoS_2 photodetector fabricated by photolithography. c. Height profile of the dashed line 1 in b.

Similar photocurrent measurement was carried out to characterise the flexible MoS_2 photodetector fabricated by photolithography. Under the dark and illumination with different powers ranging from 10 µW to 35 µW, similar ohmic response can be observed through the linear relationship between the MoS_2 channel current and small bias voltages applied to photodetector (**Figure 5-9**a). The photocurrent shows a sublinear increase with increasing incident power at V = 1 V (**Figure 5-9**b)

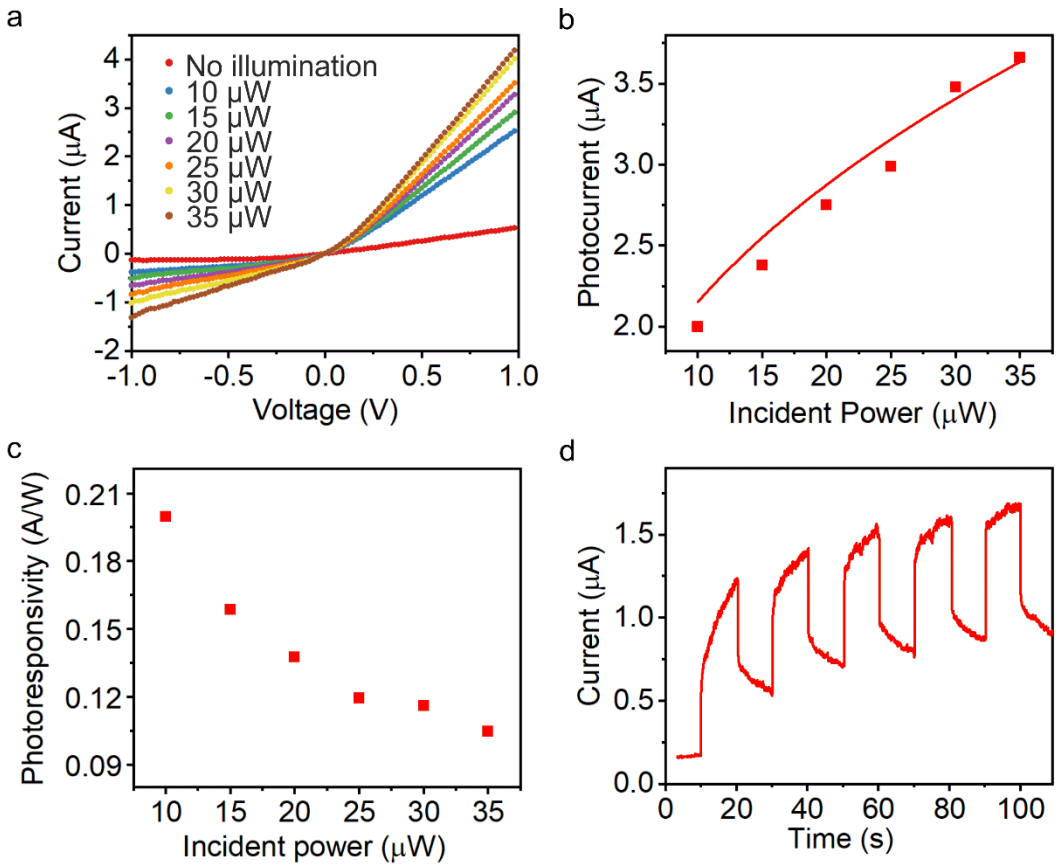


Figure 5-9 A comparison of photoresponse of the MoS_2 photodetector fabricated by photolithography. a. I-V curve of the photodetector in dark and under different illumination powers. b. Photocurrent of the photodetector under different illumination powers for V = 1 V. c. Photoresponsivity of the MoS_2 photodetector. d. Time-resolved photoresponse of the photodetector for V = 0.5 V and an illumination power of 38 μW. The calculated response time is 348 ms.

Similar to the previous photodetector, the photoresponsivity is negatively correlated with the incident light power. Under V = 1 V, the maximum photoresponsivity measured was 200 mA/W at an incident light power of 10 μW. Through the time resolved photocurrent curve under V = 0.5 V, the response time can be calculated as 348 ms.

The comparison of the performance of two photodetectors fabricated by photolithography and mechanical bilayer lithography respectively is presented in **Table 5-1**. The gain (G) of the photodetector is defined as[305,306]:

$$G = \frac{\tau}{\tau_T}$$

Equation 5-2

Where τ is the photogenerated carrier lifetime (i.e. excess minority carrier lifetime) and τ_T is the carrier transit time (i.e. the time requires for electron crossing the MoS_2 channel). Here, the carrier transit time τ_T can be expressed by:

$$\tau_T = \frac{L^2}{\mu V}$$

Equation 5-3

Where L, μ and V are the length of the channel, charge carrier mobility and the bias voltage applied to the channel, respectively. In addition, the photoresponsivity (R) of the photodetector is related to the gain and can be expressed by:

$$R = \frac{\eta G e}{h\nu}$$

Equation 5-4

Where η, e, h and ν refer to the absorbance, the elementary charge unit, Planck's constant and the frequency of light source, respectively[307]. Through Equation 5-4, the gain of each fabricated photodetector in this work can be calculated if η is assumed to be 1 in both cases. Also, the photogenerated carrier lifetime τ governs the response time of the photodetector. By replacing τ with the response time measured, the electron transit time in MoS_2 can be estimated.

Based on the above-mentioned equations, the properties of two photodetectors are summarised and compared in **Table 5-1**. It can be noted that the electron transit time of both photodetectors is very similar, indicating that the electron mobility in both devices is about the same. This excludes the possibility that different electron mobilities in two devices lead to different gains and photoresponsivity. With the constant carrier transit time, the higher the gain/responsivity, the longer the photogenerated carrier lifetime, hence, the longer response time. This is consistent with the high gain/responsivity but slow response speed of the photodetector fabricated by photolithography. The main

reason for its higher responsivity and slower response speed is the more trap states induced by defects and impurities. Under illumination on MoS_2, the trap state near to the valence band traps holes, which leads to longer carrier lifetime and higher concentration of electron carriers. The increased number of electrons makes the photodetector more conductive, leading to a higher photocurrent and photoresponsivity. However, the trap effect also lowers the electron-hole recombination rate, leading to a slower response speed.

The comparison between two photodetectors fabricated by two approaches further demonstrate that the water-based mechanical bilayer lithography is more suitable for patterning sensitive TMDs and polymer substrates by minimising the radiation and chemical damages. Further verification of the comparison of defects induced by mechanical bilayer lithography and photolithography can be done by characterising MoS_2 via XPS and transmission electron microscopy before and after each fabrication process.

Table 5-1 The comparison of properties of two flexible MoS_2 photodetectors fabricated by photolithography and mechanical bilayer lithography

	Photodetector (photolithography)	**Photodetector (mechanical bilayer lithography)**
Photoresponsivity (V = 1 V, P = 10 μW)	200 mA/W	29 mA/W
Photoresponsivity (V = 0.5 V, P = 10 μW)	159 mA/W	18 mA/W
Reponse time (V = 0.5 V)	348 ms	42 ms
Gain (V = 0.5 V)	0.309	0.035
Electron transit time τ_T	1.13 s	1.2 s

5.7 **Conclusion**

The printability of liquid exfoliated MoS_2 dispersions in the mixture of ethanol/water has been demonstrated in EHD printing. The printed MoS_2 nanosheets have the average width, length and thickness of 63 nm, 65 nm and 3.8 nm, respectively. However, due to the small lateral dimensions of these disconnected nanosheets, they are not suitable for the fabrication of photodetectors.

To fabricate the flexible photodetector, the mechanically exfoliated MoS_2 was used because this preparation method involves no chemical which may negatively influence the properties of MoS_2. The applicability of the water-based mechanical bilayer lithography has been demonstrated by fabricating a flexible MoS_2 photodetector on the PET substrate using this technique. The faster response time of this device over the counterpart fabricated by conventional photolithography has demonstrated the advantage of the water-based process, because the radiation-free and chemical-minimised fabrication process induces less defects and impurities in MoS_2 as well as polymer substrates.

5.8 **Author contributions**

The liquid exfoliation was done together with Dr. Sridevi Siddarama. The photocurrent measurement setup was built with the help of Dr. Nikolaos Farmakidis and Dr. Seongdong Lim. I carried out all experiment work, including exfoliation of MoS_2, fabrication of photodetectors as well as device measurement.

Chapter 6

Modifications of thin-film transistors by electrohydrodynamic printing

6.1 Introduction

Apart from 2DMs and polymers, biomolecules and biomaterials (e.g. proteins, DNA and silk) also have great potential in flexible technologies especially for biosensing. However, most of them may be soluble in water, and they have very low tolerance to most chemicals. Therefore, conventional resist-based techniques or the proposed mechanical bilayer lithography are not suitable for them. To find a solution, this chapter explores more possibilities of integrating the direct EHD printing technique with sensitive biomolecules.

Biomolecules such as protein, DNA and peptide play an essential role in biosensors due to their selective binding to the specific biomarker. By the mechanism of antigen-antibody reaction, the presence of a specific biomarker can be detected. Such biomolecules are widely used to functionalise electronic and photonic devices which will show characteristic signal changes if the specific biomarker is detected. One common platform of electronic devices that can be functionalised by biomaterials is TFTs. By functionalising the semiconductor channel of TFTs, the transfer characteristic is expected to show a shift in the threshold voltage upon the presence of the specific biomarker.

The conventional functionalisation approach of TFTs is drop casting. **Figure 6-1** shows the schematic of drop casting process. The solution containing biomolecules is dropped onto the TFT sample, and then the sample with biomolecules is kept in a humid environment for a period of time to ensure the immobilization. Although the drop casting

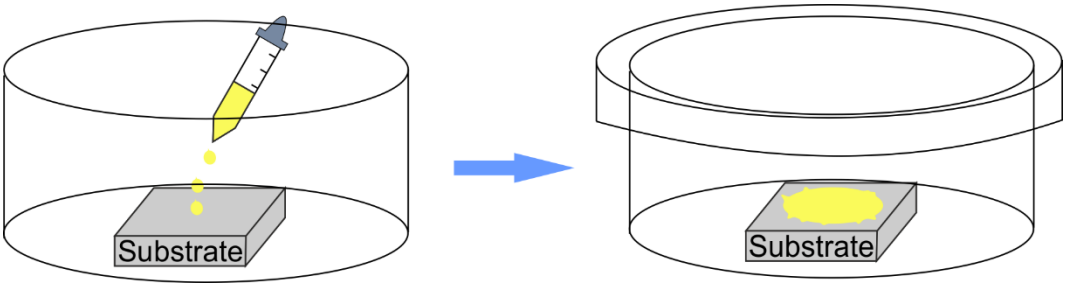


Figure 6-1 Schematic of drop casting functionalisation.

approach is very easy and straightforward, there is a disadvantage of the solution spreading over the sample surface. If there is an array of TFTs on a single chip that are expected to be functionalised by different biomolecules, this method is not applicable for the localised functionalisation of a specific TFT.

To achieve localised functionalisation, microfluidics can be a solution as the microfluidic channel minimises the contact area between the TFT device and the biomolecular solution. The contact area is defined by the design of microfluidic channels. The localised functionalisation of adjacent devices by different biomolecules still requires complex design of the microfluidic channel, because each biomolecule should be contained in a separate channel and there should not be overlapping between each channel. Thus, the design and fabrication of such complex microfluidic channels may be a big challenge. Inputting each biomolecule into a separate channel requires more materials for the preparation of each biomolecular solution, leading to an increase in the fabrication cost.

In this work, EHD printing of biomolecules is proposed to realise the on-demand localised functionalisation in a simple and low-cost way. Compared to drop casting, the use of high electric field allows only a small amount of materials to be ejected onto the specific area on the substrate, which minimises the waste of materials. The direct and rapid printing process is more promising for multiple-functionalisation on a single chip with an array of TFTs. If a row of TFTs is functionalised differently by EHD printing to detect various biomolecules, only a simple microfluidic channel will be needed for the

solution which contains various biomolecules flowing through each TFT, and multiple-sensing can be achieved simultaneously by the lab-on-chip device.

This work is in collaboration with PragmatIC Semiconductor Ltd which have a unique and scalable technology platform to manufacture ultra-low-cost flexible integrated circuits (FlexICS). In the collaboration, PragmatIC is mainly responsible for fabricating TFTs by making use of their advantageous manufacturing technology, while we are in charge of modifying these TFTs by the on-demand EHD printing of the antibody of cardiac troponin I (cTnl) protein towards biosensing applications. cTnl protein is a biomarker of the myocardial damage. The normal range in the body serum is below 0.04 ng/mL. If the concentration is higher than this value, it may indicate heart attack. The mortality rate of acute myocardial damage is as high as 34%–42%, and most deaths occur before hospital admission[308]. Therefore, monitoring the concentration of cTnl protein in the body serum is an effective way to diagnose the disease at the early stage so that proper and prompt treatment can be given to the patient.

6.2 Layout of TFTs from PragmatIC

As shown in **Figure 6-2**, the TFTs provided by PragmatIC had a bottom-gate top-contact architecture with amorphous indium gallium zinc oxide (a-IGZO) as the semiconducting material. On one single chip, there are many TFTs placed in an array. TFTs are with various dimensions (width × length) of IGZO channel, including 50 µm × 2 µm, 50 µm × 3 µm, 50 µm × 5 µm and 50 µm × 10 µm. Rigid substrates of Si/SiO_2 were used as the first trial to demonstrate the applicability of the on-demand modification through EHD printing of biomolecules, after which it can be extended to flexible substrates.

IGZO TFTs with n-type functionalities have been widely used and even been commercialized in displays due to the relatively high electron mobility and low-temperature processability that is compatible with flexible substrates[309,310]. It has already been demonstrated that the IGZO channel can be covalently functionalised by

organofunctional alkoxysilane molecules such as (3-Aminopropyl)triethoxysilane (APTES) which can help immobilize biomolecules for biosensing glucose, protein and DNA[311–314]. Thus, APTES is also used in this work to locally functionalise the IGZO channel through the on-demand EHD printing. This establishes the basis for the covalent immobilization of the biomolecules on the IGZO surface through the amino-silanization.

6.3 **Aims of chapter**

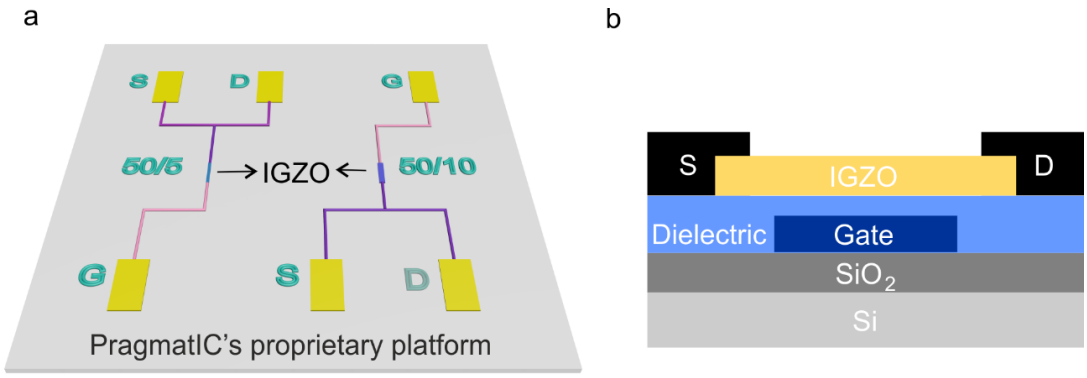


Figure 6-2 Schematic of TFTs provided by PragmatIC. a. The top-view of the TFT array. b. The cross-section of each component layer of TFTs, including Si/SiO_2 substrate, the dielectric layer, the bottom gate electrode, IGZO semiconductor channel and source/drain electrodes.

The aim of this chapter is mainly the modification of TFTs by on-demand EHD printing of the antibody of cTnI. By building a structure on the IGZO channel through EHD printing shown in **Figure 6-3**, including APTES as an amino-silane linker which helps the immobilization of biomolecules and the antibody of cTnI, the modified TFT is expected to show a characteristic response to cTnI protein.

Here is a list of aims:

- Examine the electrical properties of bare TFTs and optimise the measurement conditions to avoid external influences.
- Covalently and locally functionalise TFTs by EHD printing of APTES which acts as the linker between IGZO and biomolecules, and further functionalise TFTs by EHD printing of the antibody of cTnI with the help of EDC and NHS molecules.

- Demonstrate the functionalisation effect by measuring the change in electrical properties of modified TFTs.
- Characterise the electrical response of the modified TFT to the presence of cTnI.

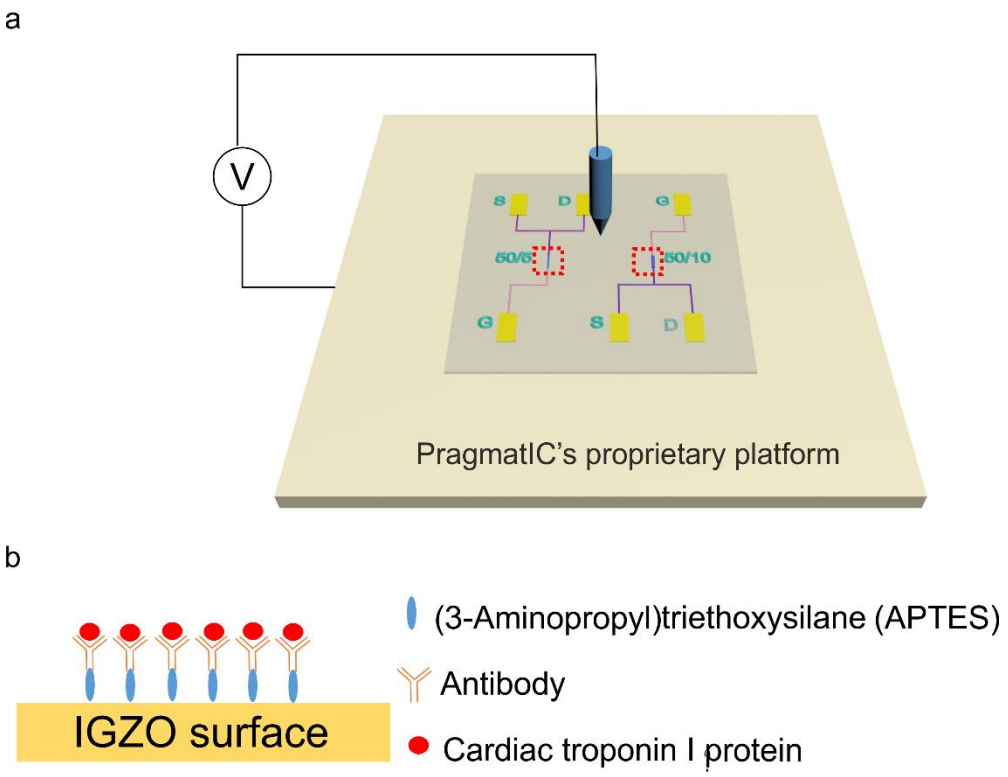


Figure 6-3 a. Modification of the IGZO surface (red rectangular area) through on-demand EHD printing. b. the structure to be built by EHD printing on the IGZO surface, including APTES as the amino-silane linker and the antibody of cTnI.

6.4 Method and materials

6.4.1 Modification with APTES

APTES (Sigma-Aldrich) was dissolved in IPA with the volume concentration of 5%. Before EHD printing, APTES solution was sonicated for 20 min to make sure that APTES molecules are fully and uniformly dispersed in IPA.

After sonication, APTES solution was loaded into glass capillaries (with the inner diameter of 5 µm) that were coated with Au conductive layer and pre-treated by PFDT. The EHD printing of APTES in IPA was carried out without the use of syringe pump. The tip-substrate distance was controlled at 100–200 µm. The voltage applied between the capillary and substrate was 1 kV to 2 kV. The moving speed of stage was controlled at

20 mm/s. APTES was printed as line patterns which past the IGZO channel of each device.

After printing, the TFT sample was kept in a humid environment overnight to ensure the effective growth of APTES molecules on the IGZO surface, and then rinsed with IPA and DI water.

6.4.2 Modification with the antibody

Cardiac Troponin I Polyclonal Antibody (Invitrogen, Rabbit/IgG, 1 mg/mL) was diluted in phosphate buffer solution (PBS, Sigma-Aldrich pH = 7.4) with the final concentration of 1 µg/mL. The mixed solution of 10 mM EDC and 20 mM NHS were prepared in PBS (pH = 7.4).

The mixture of EDC, NHS and antibody was printed together. Before each EHD printing, 45 % (v/v) EDC and NHS mixture in PBS, 45 % (v/v) diluted antibody in PBS and 10% (v/v) glycerol (Sigma-Aldrich) were mixed together and loaded into the syringe which was connected to the capillary.

The EHD printing of EDC, NHS and antibody was done with the help of a back pressure added by the syringe pump. The added back pressure was 15 µL/min. The Au coated capillaries (with the inner diameter of 30 µm) were pre-treated by PFDT. The distance between the capillary tip and substrate was controlled at 100 µm–150 µm. The applied voltage between the capillary and substrate was about 400 V. After the EHD printing of the mixture of EDC, NHS and antibody, the sample was kept in a humid environment for 2 h to allow sufficient incubation, and then cleaned with PBS and DI water.

6.4.3 Preparation of cardiac troponin I protein

Recombinant Human Cardiac Troponin I protein (Abcam) were diluted into various concentrations in 0.1 mM PBS (pH = 7.4). To detect whether the modified device had response to this protein or not, the diluted solution was drop casted onto the modified

sample surface and incubated for 30 min. Then the electrical measurement of TFTs was carried out right after the incubation of cTnl protein.

6.4.4 Fabrication of microfluidic channels

The SU-8 mould of microfluidic channels was fabricated by photolithography using photoresist SU-8 2025 and hard baked to harden the mould surface. PDMS was prepared by fully mixing SYLGARD™ 184 silicone elastomer and the curing agent with 10:1 ratio and pouring the mixture into the mould. After degassing to get rid of air bubbles in PDMS mixture, the mixture was cured at 75℃ for 1 h. Then PDMS patterned with microfluidic channels were peeled off and cut into pieces with a proper size. Inlet and outlet of the microfluidic channel were punched and connected to external tubes.

6.4.5 Electrical measurement of TFTs

The probe station and the semiconductor analyser (**Figure 3-4**) were used to measure the electrical properties of TFTs in the dark condition at each stage of modification. The characterisation of TFTs mainly includes the transfer characteristic (I_{ds} vs. V_g curve) and output characteristic (I_{ds} vs. V_{ds} curve).

6.4.6 Fluorescence microscope imaging

The chip with the printed line of APTES was incubated with the above-mentioned mixture of EDC, NHS, glycerol and cTnl antibody for 1 hour at room temperature, washed with PBS, DI water and dried by N_2. It was subsequently incubated with the secondary antibody (Invitrogen, Goat anti-Rabbit IgG-Alexa 488, stock concentration of 2 mg/mL) at a dilution of 1:1000 for 30 min at room temperature, washed with PBS, DI water and dried by N_2. Then a Zeiss LSM980 microscope was used for fluorescence microscope imaging.

6.5 Characteristics of bare TFTs

Since the functionalisation effect and biosensing response are expected to be detected through the change of characteristics of TFTs, external factors that may cause the characteristic results confusion were explored and optimised at the initial stage.

The first external factor is the visible light during the electrical measurement. While measuring the electrical properties of bare TFTs, it has been found that TFTs are very sensitive to visible light although the band gap of IGZO is sitting in UV range. **Figure 6-4** shows that the threshold voltage (V_{th}) shifts negatively under the illumination compared to that under the dark condition. Studies have reported that the negative shift of V_{th} under the illumination is due to the ionization of oxygen vacancies[315,316]. Upon the presence of visible light and negative gate voltage (V_g), the ionized oxygen vacancies (V_O^{2+}) are created, which induces an increase in the number of free electrons thus negative shift of V_{th}[316]. To avoid the influence of illumination, all following results are based on the dark condition.

The second factor is the hysteresis effect of TFTs. It is difficult to completely eliminate

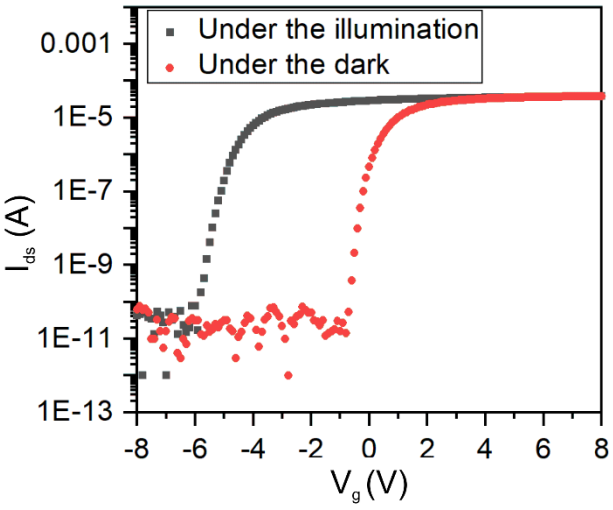


Figure 6-4 The comparison of the transfer characteristic of the TFT between under illumination and under dark conditions.

the hysteresis effect while measuring the transfer characteristic of TFTs. Instead, two measuring approaches have been explored to minimise such effect. The first measuring approach is sweeping the gate voltage from the negative to the positive and backwards

to the negative (non-symmetrical approach) with the sweeping speed of 20 ms per 0.1 V. The second measuring method is symmetrically scanning the gate voltage along 0 V (e.g. 0 V, −1 V, 1 V, −2 V, 2 V…) with the scan speed of 20 ms per 0.1 V. Both methods were used to measure the transfer characteristic of the bare TFT. The measured results of both methods are quite similar because the bare TFT shows a small hysteresis effect of about 0.2 V (**Figure 6-5**).

However, the modification of TFTs with APTES molecules strengthens the hysteresis

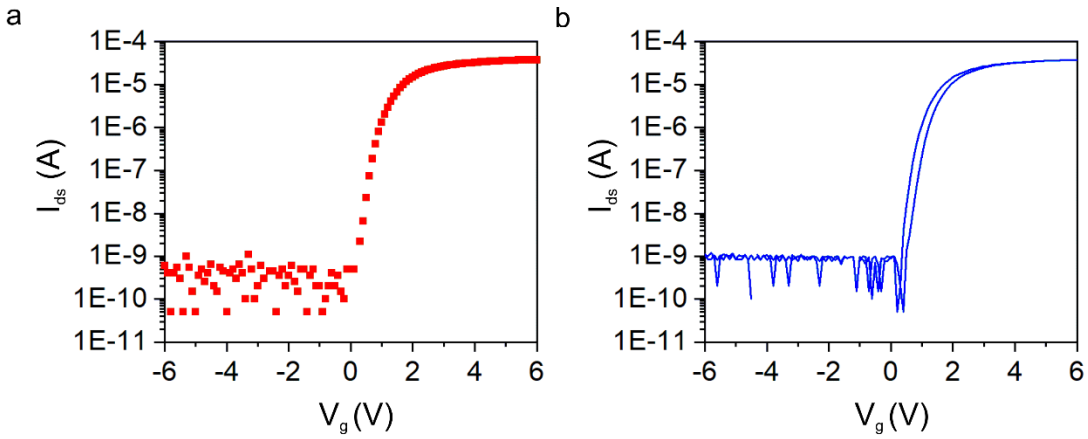


Figure 6-5 Comparison of the transfer characteristic of the bare TFT measured by two methods: a. the symmetrical scanning approach. b. non-symmetrical scanning approach.

effect. This leads to an obvious difference of the transfer curves measured by the two approaches. The transfer curve of the TFT modified with APTES measured by non-symmetrical way shows a larger hysteresis effect of 1.8 V compared to 0.2 V of the bare TFT (**Figure 6-6**). The larger hysteresis makes the non-symmetrical measuring method less advantageous as it may adversely influence the judgement of the V_{th} shift, while the symmetrical voltage approach can effectively eliminate the accumulation of free carriers induced by the ionization of oxygen vacancies, leading to more reliable results.

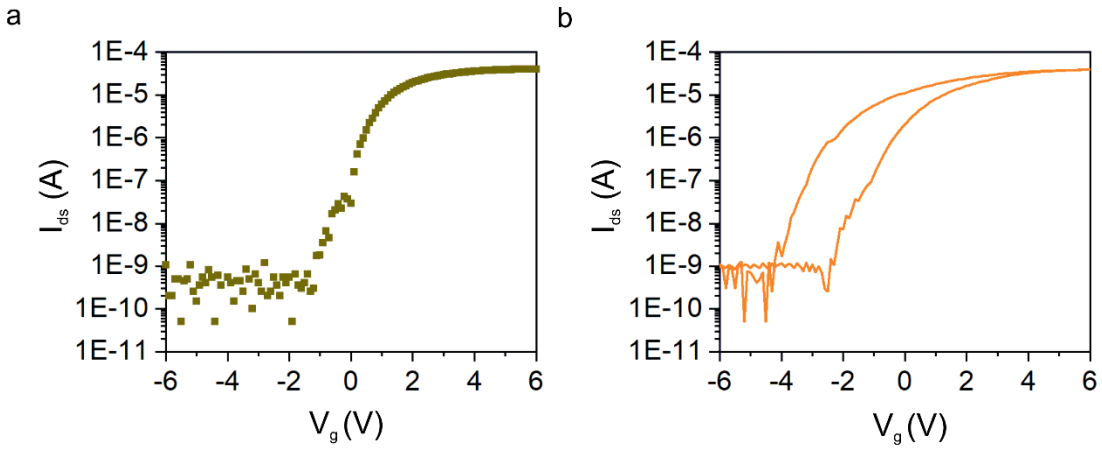


Figure 6-6 Comparison of the transfer characteristic of the TFT modified with APTES measured by two methods: a. the symmetrical scanning approach. b. non-symmetrical scanning approach.

After the optimisation of the electrical measurement conditions, the output characteristics and transfer characteristics of a bare TFT are shown in **Figure 6-7**. For the output characteristics of a 50 µm × 5 µm TFT with V_g varied from 2 V to 4 V, the drain-source voltage (V_{ds}) shows a good linear relationship with the drain-source current (I_{ds}) while V_{ds} is small, indicating a good ohmic contact between the semiconductor channel and electrodes (**Figure 6-7**b). At a higher V_{ds}, the output curve shows a good pinch-off behavior with the I_{ds} saturation. The transfer characteristic at the fixed V_{ds} = 0.5 V displays a typical n-type behavior that the device is gradually switched on while increasing the V_g (**Figure 6-7**c). The I_{on}/I_{off} ratio is 1.93 × 10^5. The calculated subthreshold swing is 156 mV dec^{-1}. By plotting the square root of I_{ds} ($I_{ds}^{0.5}$) as a function of V_g (**Figure 6-7**d), the threshold voltage can be calculated by the linear extrapolation method in the saturation region as 1.76 V[317].

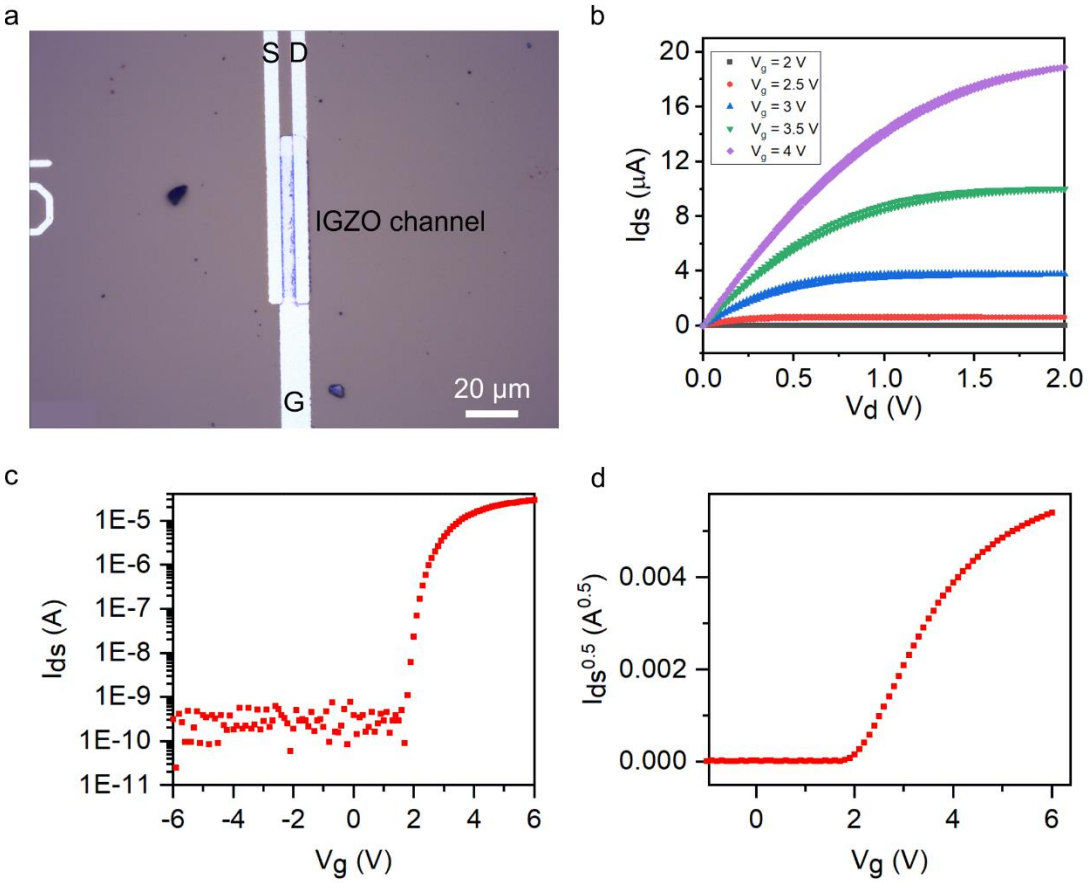


Figure 6-7 a. The microscope image of a 50 μm × 5 μm TFT. b. The output characteristics of the TFT with V_g varied from 2 V to 4 V. c. The transfer characteristic of the TFT at the V_{ds} = 0.5 V. d. The $I_{ds}^{0.5}$- V_g curve at the V_{ds} = 0.5 V.

6.6 Modification

The IGZO channel was modified with APTES and the mixture of EDC, NHS and cTnI antibody by EHD printing, sequentially. After each modification, the transfer characteristic of the TFT was tested to confirm the functionalisation effect.

6.6.1 Modification by APTES

After EHD printing of APTES on the IGZO channel, a layer of aminosilane formed on the IGZO surface (**Figure 6-8**a). This was confirmed by examining the presence of amino groups by XPS (**Figure 6-8**b). The N 1s spectra of the IGZO channel with or without APTES were measured. It can be noted that there was no obvious N 1s peak before IGZO was modified with APTES, while the pronounced N 1s peak at around 401

eV appeared after IGZO was modified with APTES (**Figure 6-8**b). This comparison confirms the silinalization of APTES on IGZO surface.

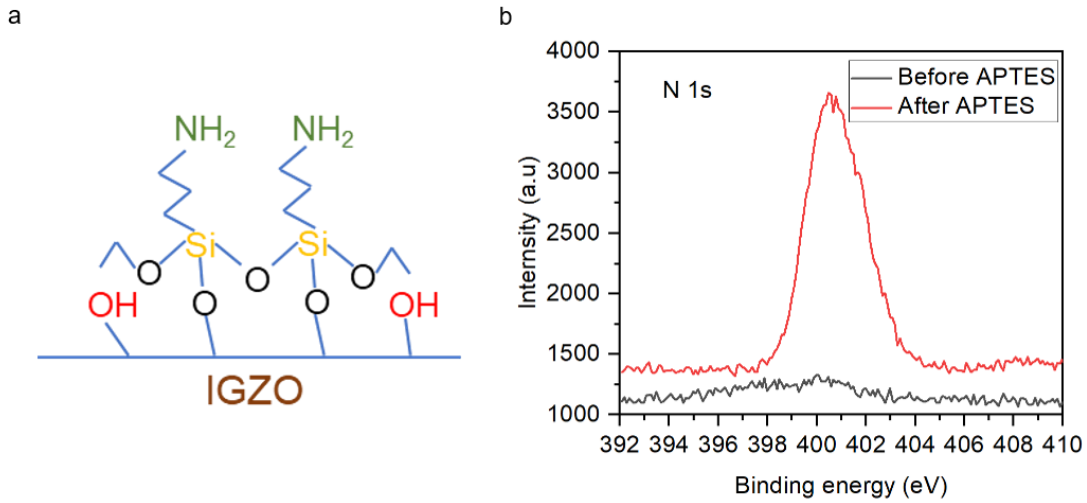


Figure 6-8 a. Schematic of the modification of IGZO surface with APTES molecules. b. N 1s XPS spectra of IGZO surface with or without the modification of APTES.

Figure 6-9a shows that the printed APTES line is with the linewidth of about 115 μm and covers the IGZO channel. The transfer curves of this device were measured before and after modification with APTES molecules. Compared to the transfer curves of the device before printing APTES, the V_{th} shifts negatively after printing APTES molecules (**Figure 6-9**b). The reason is that positively charged APTES molecules induce an increase in the number of free electrons in IGZO channel, thus a negative shift of V_{th}.

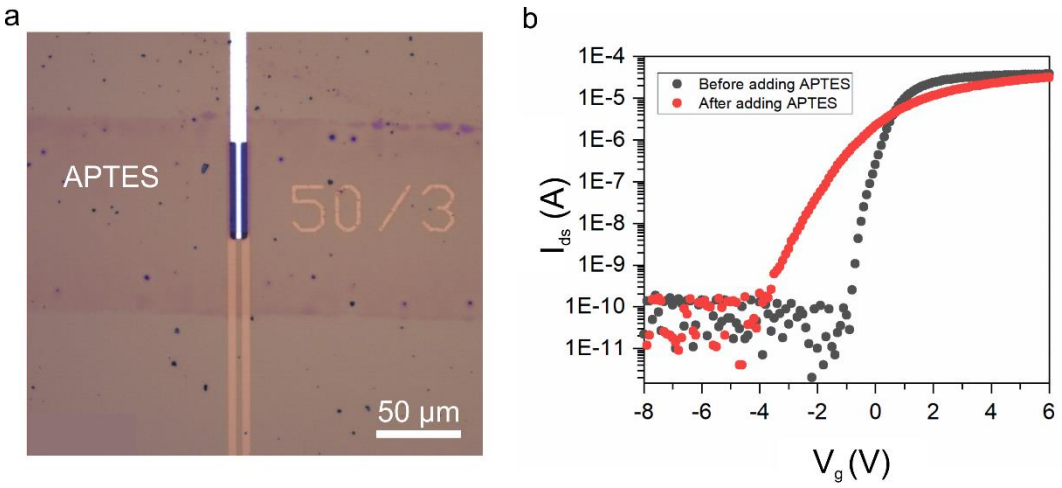


Figure 6-9 a. Optical image of the IGZO channel modified with APTES. b. Comparison of transfer curves of the TFT before and after printing APTES.

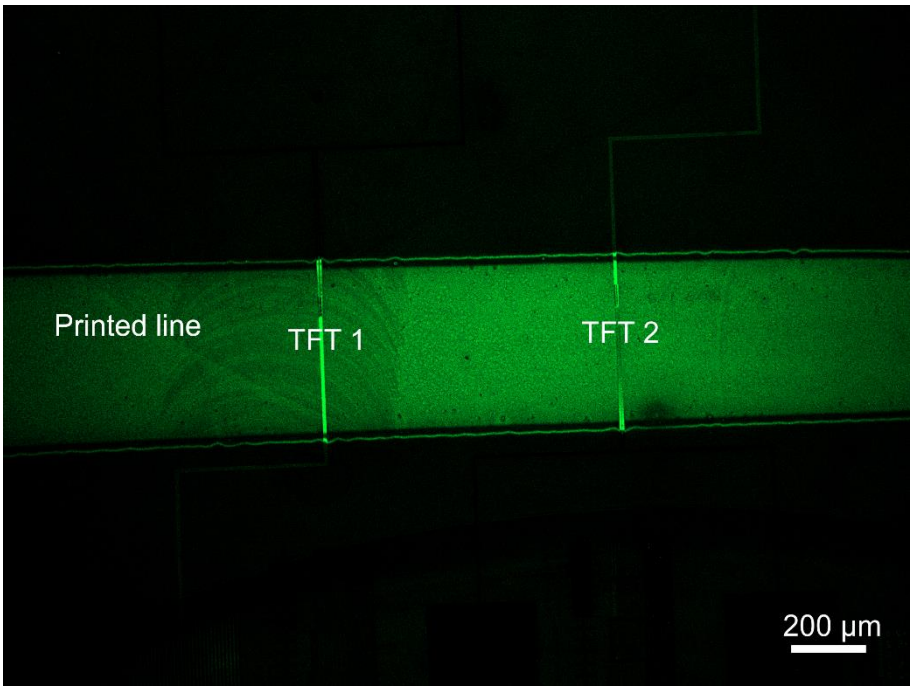


Figure 6-10 Fluorescence microscope image of the sample with the printed line of APTES. Before imaging, the sample was incubated with a mixture of nonflorescent cTnI antibody and a mixture of fluorescent secondary antibody (Goat anti-Rabbit IgG-Alexa 488) in sequence.

The covalent functionalisation of IGZO surface with APTES molecules enables the growth of amino groups so that APTES can act as a linker between the metal oxide surface and biomolecules. To verify the localised functionalisation, the chip with the printed line pattern of APTES was incubated with a mixture of nonflorescent cTnI antibody and a mixture of fluorescent secondary antibody in sequence. The fluorescence microscope image in **Figure 6-10** presents a very strong fluorescence signal in the area of the line pattern, forming a distinct contrast from the rest area. This indicates that the cTnI antibody only binds to such local area modified with APTES molecules. Thus, the localised functionalisation by EHD printing has been demonstrated.

6.6.2 Modification with the cTnI antibody

The solution of cTnI antibody was mixed with EDC and NHS molecules right before printing. In the mixture, EDC molecules react with carboxylic acid groups to form an active O-acylisourea intermediate while NHS molecules stabilize the intermediate[318]. The initial trial of printing such mixture failed due to the damage to the IGZO channel

induced by the electrical breakdown at the high voltage during the printing process. To avoid using the high voltage, the syringe pump was used to give a back pressure while the pulling process of ink, and glycerol was added into the mixture of EDC, NHS and antibody to increase the viscosity of the ink. It can also reduce the evaporation rate to prevent the nozzle clogging problem. **Figure 6-11**a shows the fluent printing process of the improved antibody mixture. It can be printed either as a continuous line or a dot by a good control of the on/off of the DC power supply. Hence, the EHD printing of the antibody of cTnI has been demonstrated. The printed dot which just covers the IGZO channel of the TFT also proves that it is feasible to use EHD printing to achieve on-demand modification of a specific TFT without influencing the adjacent TFTs (**Figure 6-11**b).

As shown in **Figure 6-12**a, the transfer curves of the device before and after modified

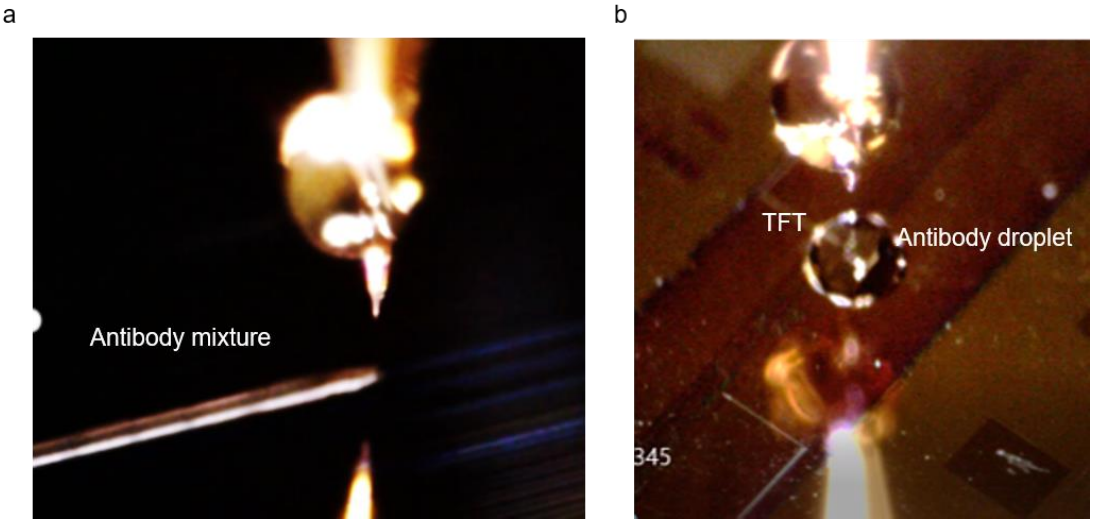


Figure 6-11 a. The EHD printing process of the improved cTnI antibody mixture into a continuous line. b. The printed dot of cTnI antibody which just covers the IGZO channel.

with APTES and the cTnI antibody were measured to confirm the functionalisation effect. To further investigate if the functionalised device exhibits response to cTnI protein, the modified device was treated with cTnI protein which was diluted in PBS with different final concentrations for 30 min to allow the sufficient reaction between cTnI and cTnI

antibody on the IGZO surface. Subsequently, the transfer curve was measured again to indicate the potential response.

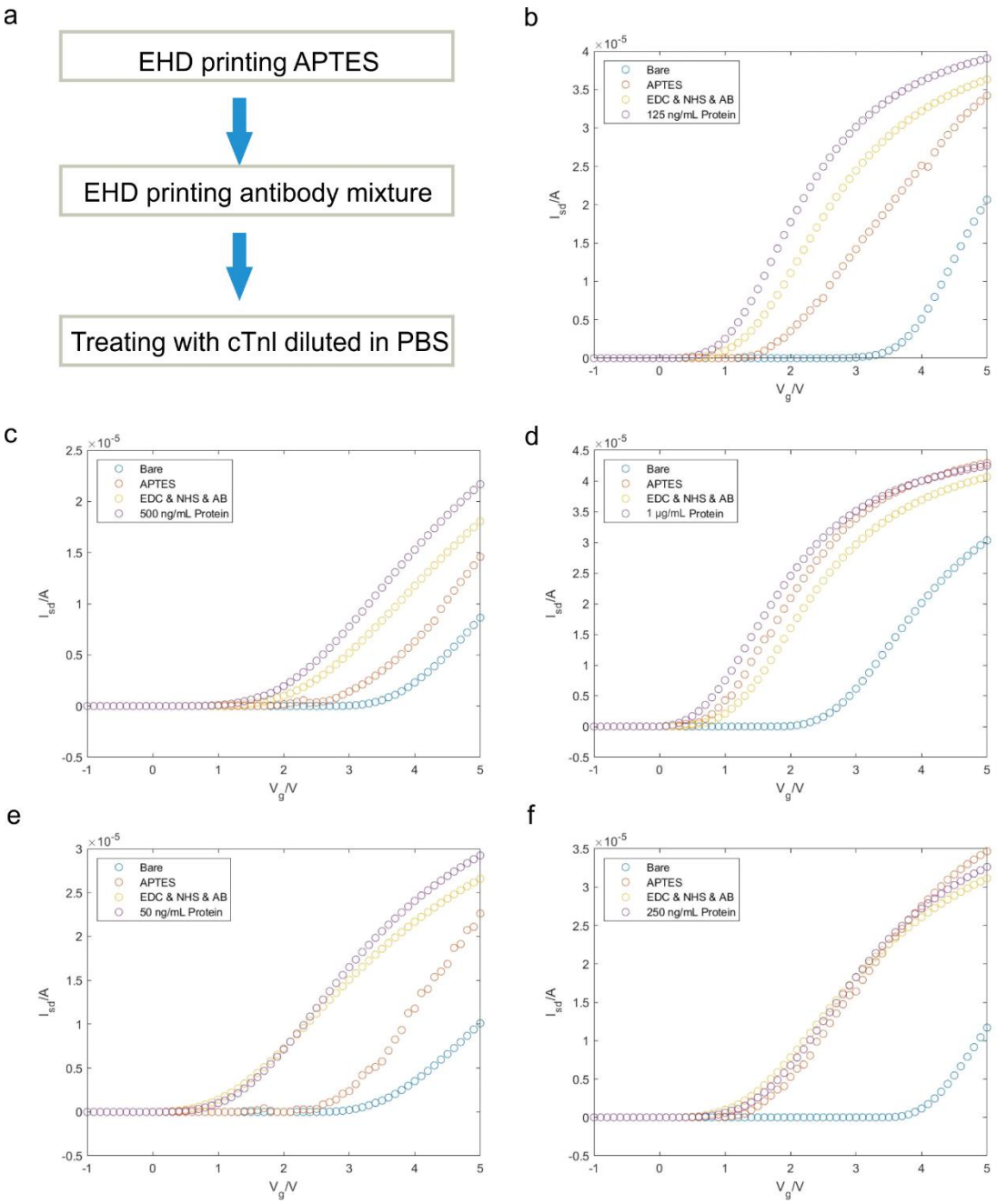


Figure 6-12 a. Modification and sensing procedures. b–f. The transfer characteristics of TFTs before/after modified with APTES and antibody mixture, as well as after sensing cTnI protein with different concentrations: b. 125 ng/mL, c. 500 ng/mL, d. 1 μg/mL, e. 50 ng/mL, f. 250 ng/mL.

Figure 6-12b–f shows the functionalisation effect and the sensing response to cTnI with concentrations varied from 50 ng/mL, 125 ng/mL, 250 ng/mL, 500 ng/mL to 1 μg/mL.

Compared to the threshold voltage in the transfer curve of the bare TFT, the threshold voltage shifts negatively after the modification with APTES, which is consistent with the previous result. The modification with the cTnI antibody further makes the threshold voltage shift negatively compared to that after modification with APTES. Therefore, the negative shift of threshold voltage has demonstrated the overall functionalisation effect of APTES and the cTnI antibody mixture.

In terms of the sensing response, results of TFTs treated with cTnI with concentrations of 125 ng/mL, 500 ng/mL to 1 μg/mL show that the presence of cTnI leads to the negative shift of threshold voltage compared to that after modification with cTnI antibody (**Figure 6-12**b–d). These results are consistent with the expectation. The isoelectronic point of cTnI is 9.87 which is greater than the pH value of 7.4 in PBS, indicating that the cTnI biomolecules are positively charged. Therefore, the positive charged biomolecules induce more numbers of free electrons in IGZO channel, leading to the negative shift of threshold voltage. Despite this, other sensing results were also obtained. **Figure 6-12**e and **Figure 6-12**f show that there is little change of threshold voltage while treating TFTs with cTnI with concentrations of 50 ng/mL and 250 ng/mL. This is attributed to the drop casting way of treating TFTs with cTnI. The droplet area of cTnI on the TFT surface is much larger than the area of IGZO channel, which results in the uneven distribution of cTnI over the IGZO channel due to the coffee ring effect. This may lead to the insufficient reaction between cTnI antibody and cTnI, hence little change of transfer curve after the treatment with cTnI.

6.7 **Integration with microfluidic channels**

To get more accurate sensing response, microfluidics was integrated with the modified TFT to confine the contact area between cTnI antibody immobilized on IGZO channel and cTnI solution. In this case, it is possible to realise active biosensing that the real-time change in electrical properties of the TFT can be measured while cTnI solution is flowing through the microfluidic channel. As the TFT has been completely functionalised

before integrating with microfluidics, its channel design was quite simple. The depth of the microfluidic channel is about 40 µm while the width is either 50 µm or 100 µm. Since source/drain electrodes and gate electrode sit on both sides of IGZO channel, windows were opened to expose electrodes to the air so that probes can reach electrode pads for electrical measurement (**Figure 6-13**a). However, the distance between the microfluidic channel and electrode window is quite narrow. It is quite challenging to use a knife blade to cut the electrode window without damaging the channel. To solve this problem, a puncher with 8 mm diameter was eventually used because it is easier to locate the position and can finish cutting in one punching process.

The conventional method of adhering a PDMS cell on a chip is treating the chip surface with O_2 plasma right before the adhering or heating the chip and PDMS after attaching them together. However, both methods are not suitable for this case due to the sensitive cTnI antibody immobilized on the chip. Without the enhancement of the adhesion between the PDMS cell and the chip, leakage occurs while inputting cTnI solution into the channel. To overcome this difficulty, SS4120 primer was used to improve the adhesion[319]. A thin layer of SS4120 primer was spin-coated on a clean silicon chip. The PDMS cell was placed on the chip coated with the layer of SS4120 primer and then transferred onto the TFT chip with the good alignment between the IGZO channel and

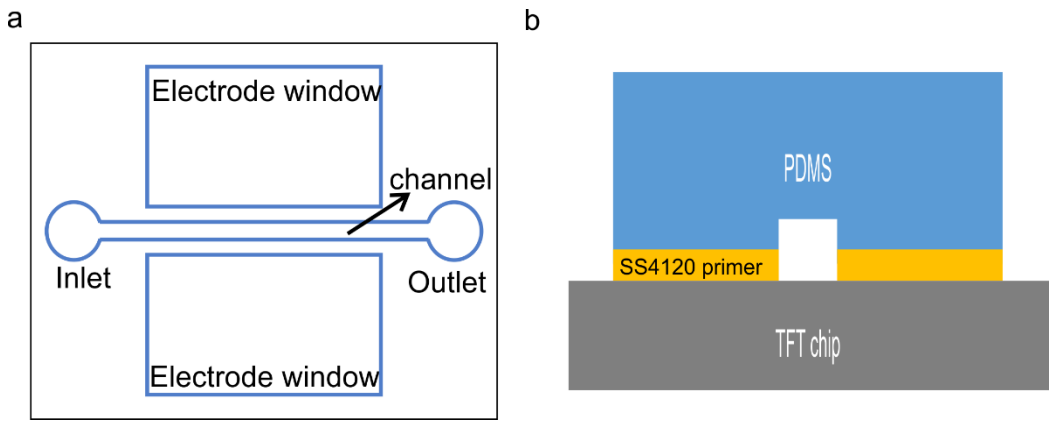


Figure 6-13 a. Schematic of the microfluidic channel design. b. Schematic of the structure of a PDMS cell attaching on a TFT chip with enhanced adhesion by SS4120 primer.

microfluidic channel (**Figure 6-13**b). The drying time of this primer is about 30 min. It effectively avoids the occurrence of leakage while the solution flowing through the microfluidic channel.

After solving the cutting and leakage issues, the PDMS cell whose microfluidic channel is aligned with the IGZO channel was tightly adhered on the TFT chip (**Figure 6-14**a). A syringe pump was used to input the DI water into the channel to test any potential leakage. It turned out that the DI water successfully flew through the microfluidic channel without leaking, indicating a good sealing between the PDMS cell and chip (**Figure 6-14**b).

6.8 Device limitation for biosensing

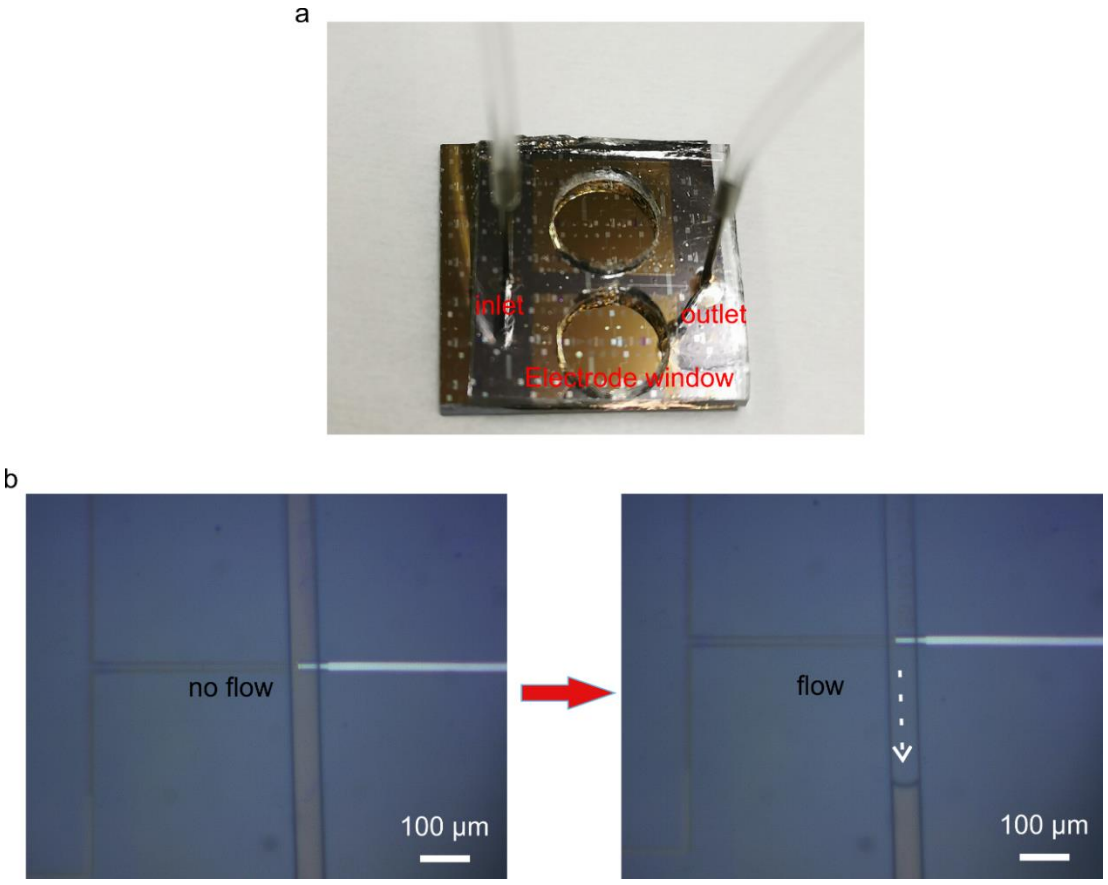


Figure 6-14 a. Photograph of the PDMS cell adhered on the TFT chip. b. Optical images of the DI water flowing through the microfluidic channel.

The device which was pre-modified with APTES and cTnI antibody was used to integrate with the microfluidic channel. **Figure 6-15**a shows the well-aligned microfluidic channel

on top of the IGZO channel. PBS was input into the channel and stayed for 30 min (**Figure 6-15**b). The transfer characteristics of the TFT were measured before and after inputting PBS to compare the change. Before PBS was input into the microfluidic channel, the transfer curve presented a normal behavior of n-type transistor under the fixed V_{ds} of 0.1V (**Figure 6-15**e). However, no transfer characteristic was observed while the microfluidic channel was filled with PBS. Instead, there was nearly no current while sweeping V_g and keeping V_{ds} at 0.1V (**Figure 6-15**f). Meanwhile the damage of source and drain electrodes was observed shown in **Figure 6-15**c. If repeating the I_{ds} vs. V_g measurement, more severe damage of source and drain electrodes could also be observed (**Figure 6-15**d). The reason for such damage is the strong electrochemical reaction between source/drain electrodes and the analyte solution even though the V_{ds} is kept at a very low value of 0.1 V. This indicates that the current TFT structure is not suitable for active sensing biomolecules while in the liquid PBS environment. Therefore, further biosensing experiment had to be paused. To avoid the direct contact between the electrode and the analyte solution, the effective solution is passivating source, drain and gate electrodes. This has been placed into the future work, and so is the active sensing of cTnl protein by integrating with microfluidics.

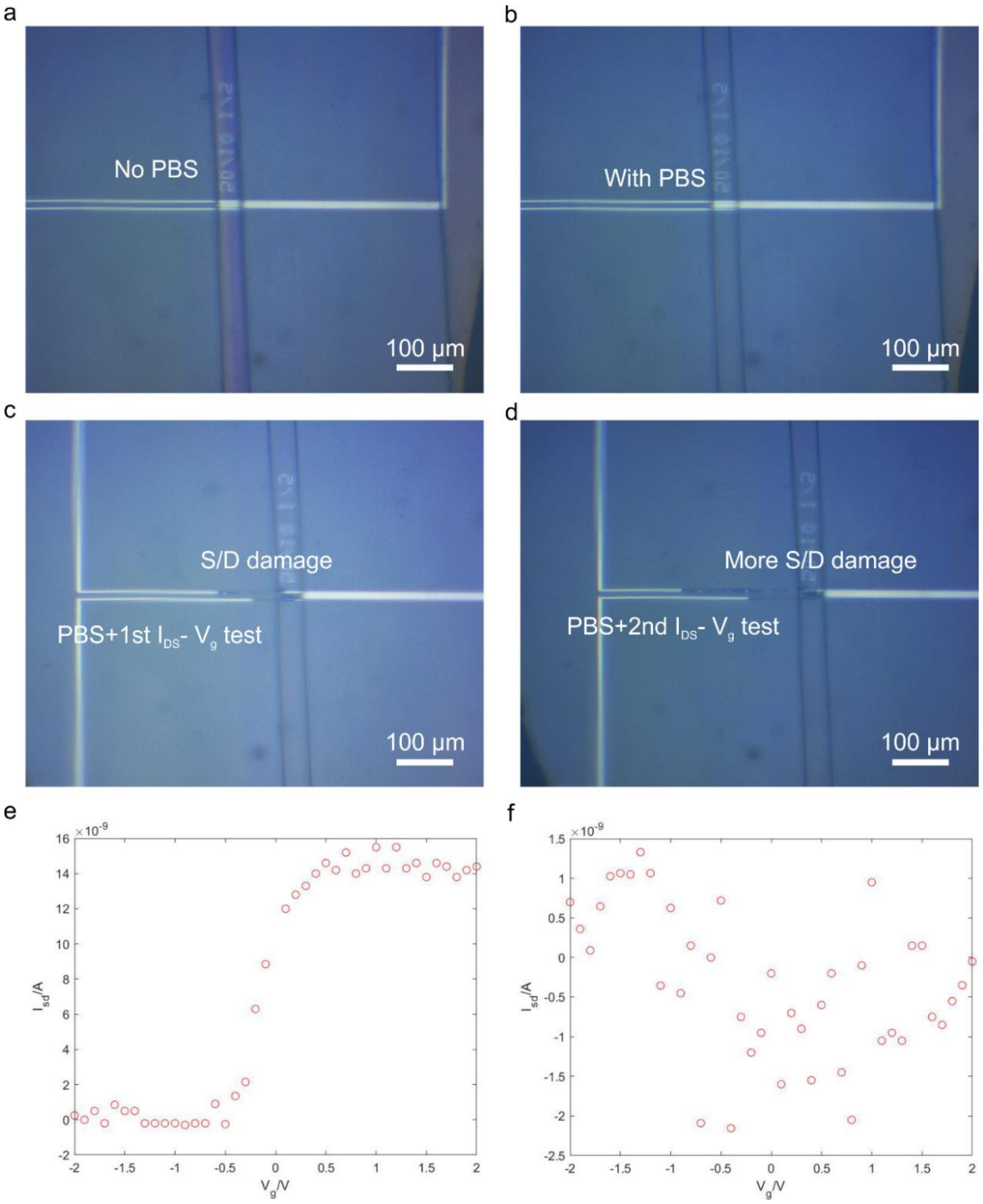


Figure 6-15 a–d. Optical images of the IGZO channel attached with the microfluidic channel while: a. no PBS is input. b. PBS is input. c. PBS is input and the completion of the first I_{ds} vs. V_g measurement. d. PBS is input and the completion of the second I_{ds} vs. V_g measurement. e–f. The I_{ds} vs. V_g curve under the fixed V_{ds} of 0.1 V: e. before PBS is input into the channel. f. after PBS is input into the channel.

6.9 Conclusions

In this chapter, a novel and low-cost method of using EHD printing to realise the localised functionalisation of TFTs has been demonstrated. The advantage of EHD printing is the

significant decrease in the functionalisation area so that the specific device can be locally modified.

Chips with an array of various TFTs used in the work were fabricated by our collaborators at PragmatIC. Two steps have been developed to achieve the localised functionalisation of TFTs. Firstly, the EHD printing of APTES has been demonstrated to be capable of providing amino groups for the semiconductor IGZO channel of TFT. This enables the immobilization of biomolecules. The printability of the mixture of cTnl antibody in EHD printing has also been proved. The printing of antibody is to enable the specific binding between cTnl antibody and cTnl protein. In this case, the modified TFT can have response to the presence of cTnl protein. The functionalisation effect and response have been read out by measuring the change of transfer characteristics of TFTs. Results show that the EHD printing of APTES and the mixture of cTnl can cause the negative shift of the threshold voltage, which confirms the functionalisation effect. After treating the modified TFT with cTnl protein for 30 min, the majority of TFTs show response of the negative shift of threshold voltage, which is consistent with the theoretical expectation. However, meanwhile the little shift of threshold voltage has also been noted due to the treatment with cTnl protein by drop casting. This leads to the uneven distribution of cTnl protein over the chip due to the coffee ring effect. Thus, there is a possibility that the modified TFT cannot directly react with cTnl protein and show no obvious response.

To confine the direct contact area between the IGZO channel of TFT and cTnl solution, the PDMS cell with the microfluidic channel has been fabricated and adhered onto the TFT chip. However, due to the strong electrochemical reaction between the exposed electrode and PBS, the active detection of cTnl by the modified TFT with the microfluidic channel cannot be carried on. The passivation of electrodes is needed to continue the following experiment.

6.10 Author contributions

TFTs were fabricated by collaborators Dr. Feras Alkhalil and Dr. Satyajit Das from PragmatIC Semiconductor Ltd. I conceived the concept of the localised functionalisation of TFTs using EHD printing and carried out most experimental work. Handling biomolecules was instructed by Dr. Sridevi Siddarama and Dr. Mengyun Wang. The fabrication of microfluidic channels using PDMS was with the help of Dr. Nikolaos Farmakidis.

Chapter 7

Conclusions and future work

7.1 Conclusions

This work was motivated by a lack of nanomanufacturing techniques for sensitive and flexible materials as well as the urgency to minimise the use of harsh chemicals during the manufacturing process. The goals were to develop a novel and sustainable nanomanufacturing technique for the construction of flexible devices and meanwhile explore more possibilities in the additive EHD printing technique to integrate with sensitive flexible materials. Sensitive materials including polymers, 2DMs and biomolecules have been used in this work to verify the suitability of proposed nanomaufacturing techniques.

In chapter 1, the importance of nanomanufacturing techniques for the development of nanotechnology was illustrated. Without nanomanufacturing, the invention of functional devices based on nanotechnology is not achievable. Meanwhile, prioritizing the sustainability in developing novel nanomanufacturing techniques should be emphathised. Therefore, with the emerging flexible technology, the development of nanomanufacturing techniques for flexible materials should not only consider the poor chemical resistance and low thermal/mechanical stability of flexible materials but also maximise the sustainability level.

In Chapter 2, properties and applications of functional flexible materials (i.e. polymers, biomaterials and nanomaterials) and the state-of-the-art nanomanufacturing techniques for flexible technology including SPL, inkjet printing, EHD printing, DLW and nanoimprinting were detailed. The low processability of such flexible materials requires the avoidance of using hazardous chemicals and strong radiation during the

manufacturing process. However, currently it is inevitable to use organic solvents in most nanomanufacturing techniques for flexible technology. Thus, it leads to strict restrictions on the selection of functional materials, and the sustainability remains insufficient.

To improve the sustainability of manufacturing process and applicability on sensitive materials for flexible technology, an environmental-friendly water-based mechanical lithography technique for processing polymers and 2DMs was proposed in Chapter 4. By making use of the bilayer structure where the bottom layer of PVA is soluble in water but the top-layer of PMMA not, only water was used for the implement of development and lift-off during the fabrication process. This minimises the production of chemical waste at the source, hence an increase in the sustainability. The suitability of this technique on both rigid SiO_2/Si substrates and soft PET substrates was demonstrated, which enables a wider selection range of materials. This technique is able to write arbitrary patterns with the highest resolution of 310 nm. The resolution can be further improved through optimising the geometry/material of the tip, the thickness of PMMA layer, the mechanical force and development parameters. The limitation of low throughput of this technique can be addressed by employing an array of parallel probes to simultaneously write patterns with no overlapping between each other.

In Chapter 5, applications of this water-based mechanical lithography technique were explored by demonstrating the fabrication of a flexible MoS_2 photodetector. This also proved the suitability of this technique on sensitive 2DMs. Due to the no involvement of chemicals, mechanical exfoliation method was selected to prepare MoS_2 thin films with a proper microscale lateral dimension. As a comparison, the conventional photolithography was used to fabricate a counterpart flexible MoS_2 photodetector. Comparison between the device performance of both devices shows that the photodetector fabricated by the water-based lithography exhibits a faster response time

of 42 ms. This is attributed to less defects and impurities induced in the water-based fabrication process without using hazardous chemicals.

In Chapter 6, the integration of the cost-effective EHD printing with cTnl antibody was demonstrated to enhance the bio-functionality of TFTs provided by our collaborator PragmatIC Semiconductor Ltd. The utilisation of EHD printing enables the localised functionalisation of a specific TFT in an array, which greatly reduces the volume of materials needed. The IGZO semiconductor channel of TFTs was firstly functionalised by EHD printing of APTES molecules to provide organofunctional amino groups. Subsequently, the mixture of cTnl antibody was printed on the IGZO surface, which enables the specific reaction between cTnl antibody and cTnl protein. The negative shift of threshold voltage of the modified TFT confirms the functionalisation effect of APTES and cTnl antibody. After treating the modified TFT chip by drop casting, the device shows a response to the presence of cTnl protein with the negative shift of the threshold voltage. To achieve active detection of cTnl protein, PDMS cells with microfluidic channels were fabricated and integrated with modified TFTs. The microfluidic channel confines the direct contact area between the IGZO channel and cTnl protein solution. However, due to the strong electrochemical reaction between the electrode and analyte, further optimisation of the TFT structure by passivating each electrode is required to achieve active detection of cTnl protein.

7.2 **Future work**

Following the current achievement made in the thesis, more work can be accomplished in the future. This section presents the future work in terms of each chapter from Chapter 4–6.

The development of the water-based mechanical bilayer lithography provides more selections of sensitive materials that have potential applications in flexible technology in Chapter 4. This technique can be further improved with aspects to the resolution and the

quality of patterns. Apart from optimising the geometry of the tip, the PMMA thickness and the applied mechanical force, automating the development process is another effective approach to improve this technique. This could make the water development process more controllable, resulting in patterns with the consistent dimension. Replacing the liquid water by water vapour can also enhance the controllability of the development process by decreasing the dissolving rate of PVA in water.

In addition, the throughput of this technique can be improved by integrating an array of probes with the commercial AFM system. This enables the ability to simultaneously write the same patterns in parallel, leading to an increase in the fabrication effectivity. By connecting each probe with a separate actuator, its writing capability can be even extended to write various patterns independently and simultaneously.

In chapter 5, a demonstrator of applying the water-based mechanical lithography on fabricating a flexible MoS_2 photodetector was presented. More applications in flexible technology which require the use of sensitive materials are to be explored. For example, this technique can be applied to water-insoluble biomaterials such as polyactic acid and chitosan for the fabrication of implantable electronics. Water-insoluble biomaterials have outstanding biocompatibility but poor chemical resistance, which is a challenge for building functional and implantable devices. Nevertheless, the water-based technique gives the opportunity to include these materials in the implantable electronics for health monitoring.

In Chapter 6, passivating each electrode of TFTs needs to be done to achieve the active detection of cTnl. SU-8 can be a promising passivation material due to its excellent mechanical and chemical resistance. SU-8 as a negative photoresist can be patterned by photolithography to insulate all electrodes near to the semiconductor channel while opening a small window of the semiconductor channel. The patterned SU-8 can be used as a passivation layer through the hardening at the temperature of 150 ℃. One main

difficulty of handling SU-8 is that it often cracks during soft baking, hard baking or hardening process, leading to the bad passivation of electrodes. Therefore, the heating temperature should be gradually increasing at the increasing rate of 5–10 ℃/min to avoid cracking. Another potential problem is the poor adhesion between the TFT sample and SU-8, which can cause the leakage of PBS solution to electrodes. Thus, the electrochemical reaction cannot be prevented. Alternatively, a passivation layer of SiO_2 can be employed to insulate electrodes. SiO_2 can be deposited by sputtering. The thickness of the SiO_2 layer should be properly adjusted (about 100 nm) to ensure electrodes are fully insulated while the lift-off of the unpatterned SiO_2 is still feasible.

Once the passivation of electrodes is solved, the active detection of cTnI protein can be carried out by integrating the microfluidic channel with the TFT devices whose electrodes are completely insulated. With the gradually increasing concentration of cTnI protein diluted in PBS flowing through the channel, the modified TFT is expected to show a continuous shift of the threshold voltage. The sensitivity can be explored by decreasing the concentration of cTnI protein diluted in PBS until there is no change of the threshold voltage. Meanwhile, the selectivity can be confirmed by inputting the solution of a different biomolecule to the microfluidic channel. Once the active detection of cTnI protein is demonstrated to be feasible, the EHD printing can be applied to achieving multiple-functionalisation of TFTs on a single chip. Therefore, it is possible to detect multiple biomolecules simultaneously with just one biosensing platform, which can reduce the cost and time to diagnose multiple diseases.

Furthermore, the current structure of TFTs is based on rigid substrates. PragmatIC Semiconductor Ltd also have the manufacturing technology to fabricate this structure on flexible substrates. Thus, the localised functionalisation of EHD printing can be applied to TFTs on flexible substrates.

Publications and Conferences

List of publications

Work presented in this thesis

- **Y. Shu**, B.F. Porter, E.J.H. Soh, N. Farmakidis, S. Lim, Y. Lu, J.H. Warner, and H Bhaskaran. Nanoscale Bilayer Mechanical Lithography Using Water as Developer. Nano Letters 21, 3827-3834 (2021).

Collaborative Work outside this thesis

- T. Chen, Y. Lu, Y. Sheng, **Y. Shu**, X. Li, R.-J. Chang, H. Bhaskaran and J. H. Warner. Ultrathin All-2D Lateral Graphene/GaS/Graphene UV Photodetectors by Direct CVD Growth. ACS Applied Materials & Interfaces 11, 48172-48178 (2019).
- Y. Lu, J. Chen, T. Chen, **Y. Shu**, R.-J. Chang, Y. Sheng, V. Shautsova, N. Mkhize, P. Holdway, H. Bhaskaran and J.H. Warner. Controlling Defects in Continuous 2D GaS Films for High-Performance Wavelength-Tunable UV-Discriminating Photodetectors. Advanced Materials 32, 1906958 (2020).
- L. Hou, W. Xu, Q. Zhang, V. Shautsova, J. Chen, **Y. Shu**, X. Li, H. Bhaskaran and J.H. Warner. Ultrathin Lateral 2D Photodetectors Using Transition-Metal Dichalcogenides $PtSe_2$–WS_2–$PtSe_2$ by Direct Laser Patterning. ACS Applied Electronic Materials 4, 1029-1038 (2022)
- S. Aggarwal, T. Milne, N. Farmakidis, J. Feldmann, X. Li, **Y. Shu**, Z. Cheng, M. Salinga, W.H.P. Pernice and H. Bhaskaran. Antimony as a Programmable Element in Integrated Nanophotonics. Nano Letters 22, 3532-3538 (2022).

Conferences attended

- Y. Shu, B.F. Porter, E.J.H. Soh and H. Bhaskaran. Bilayer Lithography in Atomic Force Microscope. Microscience Microscopy Congress, 1—4 July, 2019, Manchester, United Kingdom.
- Y. Shu, B.F. Porter, E.J.H. Soh, N. Farmakidis, S. Lim, Y. Lu, J.H. Warner, and H Bhaskaran. Chemical-Free Atomic Force Microscope Mechanical Bilayer Lithography—A Water Based Process to Fabricate Advanced Flexible Devices. Virtual Materials Research Society Spring/Fall Meeting & Exhibit, 27 November—4 December, 2020.
- Y. Shu, S. Das, F. Alkhalil and H. Bhaskaran. On-Demand Modification of TFTs for Label-Free Biosensing. Materials Research Society Spring Meeting & Exhibit, 8—13 May, 2022, Honolulu, Hawaii.

Reference

1. Tan, Z.-K. *et al.* Bright light-emitting diodes based on organometal halide perovskite. *Nature Nanotechnology* **9**, 687–692 (2014).
2. Han, T.-H. *et al.* A roadmap for the commercialization of perovskite light emitters. *Nature Reviews Materials* (2022). doi:10.1038/s41578-022-00459-4
3. Park, J. S., Maeng, W.-J., Kim, H.-S. & Park, J.-S. Review of recent developments in amorphous oxide semiconductor thin-film transistor devices. *Thin Solid Films* **520**, 1679–1693 (2012).
4. Mosciatti, T. *et al.* A multifunctional polymer-graphene transport regimes. *ACS Nano* **9**, 2357–2367 (2015).
5. Lee, S. K. *et al.* All graphene-based thin film transistors on flexible plastic substrates. *Nano Letters* **12**, 3472–3476 (2012).
6. Hou, J., Inganas, O., Friend, R. H. & Gao, F. Organic solar cells based on non-fullerene acceptors. *Nature Materials* **17**, 119–128 (2018).
7. Green, M. A., Ho-Baillie, A. & Snaith, H. J. The emergence of perovskite solar cells. *Nature Photonics* **8**, 506–514 (2014).
8. O'Brien, J. L. Optical quantum computing. *Science* **318**, 1567–1570 (2007).
9. Imboden, M. & Bishop, D. Top-down nanomanufacturing. *Physics Today* **67**, 45–50 (2014).
10. Liddle, J. A. & Gallatin, G. M. Nanomanufacturing: a perspective. *ACS Nano* **10**, 2995–3014 (2016).
11. Manfrinato, V. R. *et al.* Resolution limits of electron-beam lithography toward the atomic scale. *Nano Letters* **13**, 1555–1558 (2013).
12. Engstrom, D. S., Porter, B., Pacios, M. & Bhaskaran, H. Additive nanomanufacturing - a review. *Journal of Materials Research* **29**, 1792–1816 (2014).
13. Chung, S., Cho, K. & Lee, T. Recent progress in inkjet-printed thin-film transistors.

Advanced Science **6**, (2019).

14. McManus, D. *et al.* Water-based and biocompatible 2D crystal inks for all-inkjet-printed heterostructures. *Nature Nanotechnology* **12**, 343–350 (2017).
15. Li, J., Lemme, M. C. & Östling, M. Inkjet printing of 2D layered materials. *ChemPhysChem* **15**, 3427–3434 (2014).
16. Li, X. *et al.* Inkjet bioprinting of biomaterials. *Chemical Reviews* **120**, 10793–10833 (2020).
17. Seekaew, Y. *et al.* Low-cost and flexible printed graphene-PEDOT:PSS gas sensor for ammonia detection. *Organic Electronics* **15**, 2971–2981 (2014).
18. Singh, R., Singh, E. & Nalwa, H. S. Inkjet printed nanomaterial based flexible radio frequency identification (RFID) tag sensors for the internet of nano things. *RSC Advances* **7**, 48597–48630 (2017).
19. Nayak, L., Mohanty, S., Nayak, S. K. & Ramadoss, A. A review on inkjet printing of nanoparticle inks for flexible electronics. *Journal of Materials Chemistry C* **7**, 8771–8795 (2019).
20. Society, R. & Sciences, P. Disintegration of water drops in an electric field. *Proceedings of the Royal Society of London. Series A* **280**, 383–397 (1964).
21. Park, J. U. *et al.* High-resolution electrohydrodynamic jet printing. *Nature Materials* **6**, 782–789 (2007).
22. Choi, M. *et al.* Full-color active-matrix organic light-emitting diode display on human skin based on a large-Area MoS_2 backplane. *Science Advances* **6**, 1–7 (2020).
23. Koh, A. *et al.* A soft, wearable microfluidic device for the capture, storage, and colorimetric sensing of sweat. *Science Translational Medicine* **8**, 1–14 (2016).
24. Macdonald, W. A. Latest advances in substrates for flexible electronics. *Journal of the Society for Information Display* **15**, 1075–1083 (2007).
25. Göpferich, A. Mechanisms of polymer degradation and erosion. *The Biomaterials:*

Silver Jubilee Compendium **17**, 117–128 (1996).

26. Zhou, H. *et al.* Transfer printing and its applications in flexible electronic devices. *Nanomaterials* **9**, 1–28 (2019).
27. Kuehr, R., Velasquez, G. T. & Williams, E. Computers and the environment—an introduction to understanding and managing their impacts. in *Computers and the environment: understanding and managing their impacts* (Springer, 2003). doi:10.1007/978-94-010-0033-8_1
28. Shen, C. W., Tran, P. P. & Ly, P. T. M. Chemical waste management in the U.S. semiconductor industry. *Sustainability* **10**, 1–14 (2018).
29. Klauk, H. Organic thin-film transistors. *Chemical Society Reviews* **39**, 2643–2666 (2010).
30. Myny, K. The development of flexible integrated circuits based on thin-film transistors. *Nature Electronics* **1**, 30–39 (2018).
31. Peng, W. & Wu, H. Flexible and stretchable photonic sensors based on modulation of light transmission. *Advanced Optical Materials* **7**, 1900329 (2019).
32. Wang, C. *et al.* Advanced carbon for flexible and wearable electronics. *Advanced Materials* **31**, 1801072 (2019).
33. Wang, W., Jia, Y., Li, H., Jiang, M. & Zhang, Z. Mechanical simulation of foldable organic light-emitting diode display supporting layer. *Journal of the Society for Information Display* **29**, 723–730 (2021).
34. Yan, C. *et al.* Stretchable and wearable electrochromic devices. *ACS Nano* **8**, 316–322 (2014).
35. Pagliaro, M., Ciriminna, R. & Palmisano, G. Flexible solar cells. *ChemSusChem* **1**, 880–891 (2008).
36. Cheng, Y., Pascoe, A., Huang, F. & Peng, Y. Print flexible solar cells. *Nature* **539**, 488–489 (2016).
37. *Flexible electronics: materials and applications*. (Springer, 2009).

doi:10.1007/978-0-387-74363-9_4

38. Shakeri, A., Khan, S. & Didar, T. F. Conventional and emerging strategies for the fabrication and functionalization of PDMS-based microfluidic devices. *Lab on a Chip* **21**, 3053–3075 (2021).
39. Geiger, S. *et al.* Flexible and stretchable photonics: the next stretch of opportunities. *ACS Photonics* **7**, 2618–2635 (2020).
40. Weidling, A. M., Turkani, V. S., Akhavan, V., Schroder, K. A. & Swisher, S. L. Large-area photonic lift-off process for flexible thin-film transistors. *npj Flexible Electronics* **6**, 14 (2022).
41. Mark, J. E. *Polymer data handbook (2nd edition)*. (Oxford University Press, 2009). doi:10.1021/ja907879q
42. Khan, S., Lorenzelli, L. & Dahiya, R. S. Technologies for printing sensors and electronics over large flexible substrates: A review. *IEEE Sensors Journal* **15**, 3164–3185 (2015).
43. Demirel, B., Yaraş, A. & Elçiçek, H. Crystallization behavior of PET Materials. *BAÜ Fen Bil. Enst. Dergisi Cilt* **13**, 26–35 (2011).
44. Zardetto, V., Brown, T. M., Reale, A. & Di Carlo, A. Substrates for flexible electronics: A practical investigation on the electrical, film flexibility, optical, temperature, and solvent resistance properties. *Journal of Polymer Science, Part B: Polymer Physics* **49**, 638–648 (2011).
45. Izdihar, K. *et al.* Structural, mechanical, and dielectric properties of polydimethylsiloxane and silicone elastomer for the fabrication of clinical-grade kidney phantom. *Applied Sciences* **11**, 1172 (2021).
46. Miranda, I. *et al.* Properties and applications of PDMS for biomedical engineering: A review. *Journal of Functional Biomaterials* **13**, 2 (2022).
47. Teo, A. J. T. *et al.* Polymeric biomaterials for medical implants and devices. *ACS Biomaterials Science and Engineering* **2**, 454–472 (2016).

48. Wang, Z., Volinsky, A. A. & Gallant, N. D. Crosslinking effect on polydimethylsiloxane elastic modulus measured by custom-built compression instrument. *Journal of Applied Polymer Science* **131**, 41050 (2014).

49. Alvaredo-Atienza, Á., Chen, L., San-Miguel, V., Ridruejo, Á. & Fernández-Blázquez, J. P. Fabrication and characterization of PEEK/PEI multilayer composites. *Polymers* **12**, 2765 (2020).

50. Kwak, K., Cho, K. & Kim, S. Stable bending performance of flexible organic light-emitting diodes using IZO anodes. *Scientific Reports* **3**, 1–7 (2013).

51. Cao, K., Zhang, M. & Liu, G. The effect of end group and molecular weight on the yellowness of polyetherimide. *Macromolecular Rapid Communications* **39**, 1800045 (2018).

52. Vosgueritchian, M., Lipomi, D. J. & Bao, Z. Highly conductive and transparent PEDOT:PSS films with a fluorosurfactant for stretchable and flexible transparent electrodes. *Advanced Functional Materials* **22**, 421–428 (2012).

53. Cai, G. *et al.* Highly stable transparent conductive silver grid/PEDOT:PSS electrodes for integrated bifunctional flexible electrochromic supercapacitors. *Advanced Energy Materials* **6**, 1501882 (2016).

54. Fu, Y. *et al.* Highly sensitive detection of protein biomarkers with organic electrochemical transistors. *Advanced Materials* **29**, 1703787 (2017).

55. Roh, E., Hwang, B., Kim, D., Kim, B. & Lee, N. Stretchable, transparent, ultrasensitive, and patchable strain sensor for human-machine interfaces comprising a nanohybrid of carbon nanotubes and conductive elastomers. *ACS Nano* **9**, 6252–6261 (2015).

56. Hwang, B. U. *et al.* Transparent stretchable self-powered patchable sensor platform with ultrasensitive recognition of human activities. *ACS Nano* **9**, 8801–8810 (2015).

57. Wang, Y. *et al.* A highly stretchable, transparent, and conductive polymer.

Science Advances **3**, e1602076 (2017).

58. Nardes, A. M. *et al.* Microscopic understanding of the anisotropic conductivity of PEDOT:PSS thin films. *Advanced Materials* **19**, 1196–1200 (2007).
59. Lipomi, D. J., Lee, J. A., Vosgueritchian, M., Tee, B. C. & Bolander, J. A. Electronic properties of transparent conductive films of PEDOT:PSS on stretchable substrates. *Chemistry of Materials* **24**, 373–382 (2012).
60. Worfolk, B. J. *et al.* Ultrahigh electrical conductivity in solution-sheared polymeric transparent films. *Proceedings of the National Academy of Sciences of the United States of America* **112**, 14138–14143 (2015).
61. Huang, D. *et al.* Perovskite solar cells with a DMSO-treated PEDOT:PSS hole transport layer exhibit higher photovoltaic performance and enhanced durability. *Nanoscale* **9**, 4236–4243 (2017).
62. Xia, Y., Sun, K. & Ouyang, J. Solution-processed metallic conducting polymer films as transparent electrode of optoelectronic devices. *Advanced Materials* **24**, 2436–2440 (2012).
63. Kim, N. *et al.* Highly conductive PEDOT:PSS nanofibrils induced by solution-processed crystallization. *Advanced Materials* **26**, 2268–2272 (2014).
64. Döbbelin, M. *et al.* Influence of ionic liquids on the electrical conductivity and morphology of PEDOT:PSS films. *Chemistry of Materials* **19**, 2147–2149 (2007).
65. Fan, X. *et al.* PEDOT:PSS for flexible and stretchable electronics: modifications, strategies, and applications. *Advanced Science* **6**, 1900813 (2019).
66. Han, W. *et al.* Recent progress of inverted perovskite solar cells with a modified PEDOT:PSS hole transport layer. *ACS Applied Materials and Interfaces* **12**, 49297–49322 (2020).
67. Lu, J. *et al.* Ultrathin PEDOT:PSS enables colorful and efficient perovskite light-emitting diodes. *Advanced Science* **7**, 2000689 (2020).
68. Lin, P. & Yan, F. Organic thin-film transistors for chemical and biological sensing.

Advanced Materials **24**, 34–51 (2012).

69. Ganji, M. *et al.* Development and translation of PEDOT:PSS microelectrodes for intraoperative monitoring. *Advanced Functional Materials* **28**, 1700232 (2018).
70. Mkhize, N., Murugappan, K., Castell, M. R. & Bhaskaran, H. Electrohydrodynamic jet printed conducting polymer for enhanced chemiresistive gas sensors. *Journal of Materials Chemistry C* **9**, 4591–4596 (2021).
71. Nezakati, T., Seifalian, A., Tan, A. & Seifalian, A. M. Conductive polymers: opportunities and challenges in biomedical applications. *Chemical Reviews* **118**, 6766–6843 (2018).
72. Kalirajan, C., Dukle, A., Nathanael, A. J., Oh, T.-H. & Manivasagam, G. A critical review on polymeric biomaterials for biomedical applications. *Polymers* **13**, 3015 (2021).
73. Sun, Q. *et al.* Functional biomaterials towards flexible electronics and sensors. *Biosensors and Bioelectronic* **119**, 237–251 (2018).
74. Wang, Z. *et al.* Recent advances in natural functional biopolymers and their applications of electronic skins and flexible strain sensors. *Polymers* **13**, 1–18 (2021).
75. Pandey, A., Negi, S. & Soccol, C. R. *Current developments in biotechnology and bioengineering: production, isolation and purification of industrial products*. (Elsevier, 2016).
76. Omenetto, F. G. & Kaplan, D. L. A new route for silk. *Nature Photonics* **2**, 641–643 (2008).
77. Kundu, B., Rajkhowa, R., Kundu, S. C. & Wang, X. Silk fibroin biomaterials for tissue regenerations. *Advanced Drug Delivery Reviews* **65**, 457–470 (2013).
78. Mannoor, M. S. *et al.* Graphene-based wireless bacteria detection on tooth enamel. *Nature Communications* **3**, 1–9 (2012).
79. Kim, D. H. *et al.* Silicon electronics on silk as a path to bioresorbable, implantable

devices. *Applied Physics Letters* **95**, 93–96 (2009).

80. Kim, D. H. *et al.* Dissolvable films of silk fibroin for ultrathin conformal bio-integrated electronics. *Nature Materials* **9**, 511–517 (2010).
81. Jeon, J. W. *et al.* Pyroprotein-based electronic textiles with high stability. *Advanced Materials* **29**, 1605479 (2017).
82. Lu, Z., Zhang, H., Mao, C. & Li, C. M. Silk fabric-based wearable thermoelectric generator for energy harvesting from the human body. *Applied Energy* **164**, 57–63 (2016).
83. Liu, Y. *et al.* Flexible, highly sensitive pressure sensor with a wide range based on graphene-silk network structure. *Applied Physics Letters* **110**, 123508 (2017).
84. Choi, A. Y., Lee, C. J., Park, J., Kim, D. & Kim, Y. T. Corrugated textile based triboelectric generator for wearable energy harvesting. *Scientific Reports* **7**, 45583 (2017).
85. Liang, B. *et al.* Fabrication and application of flexible graphene silk composite film electrodes decorated with spiky Pt nanospheres. *Nanoscale* **6**, 4264–4274 (2014).
86. Wang, C. H., Hsieh, C. Y. & Hwang, J. C. Flexible organic thin-film transistors with silk fibroin as the gate dielectric. *Advanced Materials* **23**, 1630–1634 (2011).
87. Hota, M. K., Bera, M. K., Kundu, B., Kundu, S. C. & Maiti, C. K. A natural silk fibroin protein-based transparent bio-memristor. *Advanced Functional Materials* **22**, 4493–4499 (2012).
88. Wang, H., Zhu, B., Ma, X., Hao, Y. & Chen, X. Physically transient resistive switching memory based on silk protein. *Small* **12**, 2715–2719 (2016).
89. Parker, S. T. *et al.* Biocompatible silk printed optical waveguides. *Advanced Materials* **21**, 2411–2415 (2009).
90. Tao, H., Kaplan, D. L. & Omenetto, F. G. Silk materials - A road to sustainable high technology. *Advanced Materials* **24**, 2824–2837 (2012).
91. Wang, C., Xia, K., Zhang, Y. & Kaplan, D. L. Silk-based advanced materials for

soft electronics. *Accounts of Chemical Research* **52**, 2916–2927 (2019).

92. Zhu, B. *et al.* Silk fibroin for flexible electronic devices. *Advanced Materials* **28**, 4250–4265 (2016).

93. Shojaeiarani, J., Bajwa, D. S., Rehovsky, C., Bajwa, S. G. & Vahidi, G. Deterioration in the physico-mechanical and thermal properties of biopolymers due to reprocessing. *Polymers* **11**, 58 (2019).

94. Li, X. *et al.* Electronic biopolymers: from molecular engineering to functional devices. *Chemical Engineering Journal* **397**, 125499 (2020).

95. Hsu, P. C. *et al.* Personal thermal management by metallic nanowire-coated textile. *Nano Letters* **15**, 365–371 (2015).

96. Choi, S. *et al.* Stretchable heater using ligand-exchanged silver nanowire nanocomposite for wearable articular thermotherapy. *ACS Nano* **9**, 6626–6633 (2015).

97. Yao, W., Bae, K. J., Jung, M. Y. & Cho, Y. R. Transparent, conductive, and superhydrophobic nanocomposite coatings on polymer substrate. *Journal of Colloid and Interface Science* **506**, 429–436 (2017).

98. Jayathilaka, W. A. D. M. *et al.* Significance of nanomaterials in wearables: a review on wearable actuators and sensors. *Advanced Materials* **31**, (2019).

99. Su, M. *et al.* Nanoparticle based curve arrays for multirecognition flexible electronics. *Advanced Materials* **28**, 1369–1374 (2016).

100. Akinwande, D., Petrone, N. & Hone, J. Two-dimensional flexible nanoelectronics. *Nature Communications* **5**, 1–12 (2014).

101. Gao, L. Flexible device applications of 2D semiconductors. *Small* **13**, 1603994 (2017).

102. Sarwat, S. G. *et al.* Revealing strain-induced effects in ultrathin heterostructures at the nanoscale. *Nano Letters* **18**, 2467–2474 (2018).

103. Dai, Z., Liu, L. & Zhang, Z. Strain engineering of 2D materials: issues and

opportunities at the interface. *Advanced Materials* **31**, 1805417 (2019).

104. Lee, G. H. *et al.* Flexible and transparent MoS_2 field-effect transistors on hexagonal boron nitride-graphene heterostructures. *ACS Nano* **7**, 7931–7936 (2013).

105. Das, S., Gulotty, R., Sumant, A. V. & Roelofs, A. All two-dimensional, flexible, transparent, and thinnest thin film transistor. *Nano Letters* **14**, 2861–2866 (2014).

106. Zhao, J. *et al.* Integrated flexible and high-quality thin film transistors based on monolayer MoS_2. *Advanced Electronic Materials* **2**, 1500379 (2016).

107. Park, H. *et al.* Flexible and transparent thin-film transistors based on two-dimensional materials for active-matrix display. *ACS Applied Materials and Interfaces* **12**, 4749–4754 (2020).

108. Hu, P. *et al.* Highly responsive ultrathin GaS nanosheet photodetectors on rigid and flexible substrates. *Nano Letters* **13**, 1649–1654 (2013).

109. Nalwa, H. S. A review of molybdenum disulfide (MoS_2) based photodetectors: From ultra-broadband, self-powered to flexible devices. *RSC Advances* **10**, 30529–30602 (2020).

110. Zhou, Y. *et al.* Epitaxy and photoresponse of two-dimensional GaSe crystals on flexible transparent mica sheets. *ACS Nano* **8**, 1485–1490 (2014).

111. Yu, W. *et al.* Near-infrared photodetectors based on $MoTe_2$/Graphene heterostructure with high responsivity and flexibility. *Small* **13**, 1700268 (2017).

112. Choi, J., Zhang, H., Du, H. & Choi, J. H. Understanding solvent effects on the properties of two-dimensional transition metal dichalcogenides. *ACS Applied Materials and Interfaces* **8**, 8864–8869 (2016).

113. Srour, J. R. & McGarrity, J. M. Radiation effects on microelectronics in space. *Proceedings of the IEEE* **76**, 1443–1469 (1988).

114. Walker, R. C., Shi, T., Silva, E. C., Jovanovic, I. & Robinson, J. A. Radiation effects on two-dimensional materials. *Physica Status Solidi A* **213**, 3065–3077

(2016).

115. Garcia, R., Knoll, A. W. & Riedo, E. Advanced scanning probe lithography. *Nature Nanotechnology* **9**, 577–587 (2014).

116. Martínez, R. V. *et al.* Large-scale nanopatterning of single proteins used as carriers of magnetic nanoparticles. *Advanced Materials* **22**, 588–591 (2010).

117. Chang, S., Geng, Y. & Yan, Y. Tip-based nanomachining on thin films: a mini review. *Nanomanufacturing and Metrology* **5**, 2–22 (2022).

118. Chen, H. A., Lin, H. Y. & Lin, H. N. Localized surface plasmon resonance in lithographically fabricated single gold nanowires. *Journal of Physical Chemistry C* **114**, 10359–10364 (2010).

119. Shim, W. *et al.* Plow and ridge nanofabrication. *Small* **9**, 3058–3062 (2013).

120. Lee, M. V. *et al.* Nanografting of silanes on silicon dioxide with applications to DNA localization and copper electroless deposition. *Chemistry of Materials* **19**, 5052–5054 (2007).

121. Chen, J. *et al.* Scalable fabrication of multiplexed plasmonic nanoparticle structures based on AFM lithography. *Small* **12**, 5818–5825 (2016).

122. Zhang, Y. *et al.* Cutting forces related with lattice orientations of graphene using an atomic force microscopy based nanorobot. *Applied Physics Letters* **101**, 213101 (2012).

123. Kim, J. *et al.* Fabrication of plasmonic arrays of nanodisks and nanotriangles by nanotip indentation lithography and their optical properties. *Nanoscale* **13**, 4475–4484 (2021).

124. Farmakidis, N. *et al.* Exploiting rotational asymmetry for sub-50 nm mechanical nanocalligraphy. *Microsystems & Nanoengineering* **7**, 84 (2021).

125. Liu, L. *et al.* Fabrication of sub-micrometer-sized MoS_2 thin-film transistor by phase mode AFM lithography. *Small* **14**, 1803273 (2018).

126. Li, M., Shi, J., Xi, N., Wang, Y. & Liu, L. Layer-controllable nanofabrication of two-

dimensional materials with phase-mode AFM. *Materials Letters* **232**, 43–46 (2018).

127. Maleki, H. & Bertola, V. Recent advances and prospects of inkjet printing in heterogeneous catalysis. *Catalysis Science and Technology* **10**, 3140–3159 (2020).
128. *The chemistry of inkjet inks*. (World Scientific, 2009).
129. Nguyen, T. T. N., Chen, Y. H. & He, J. L. Preparation of inkjet-printed titanium monoxide as p-type absorber layer for photovoltaic purposes. *Thin Solid Films* **572**, 8–14 (2014).
130. Lessing, J. *et al.* Inkjet printing of conductive inks with high lateral resolution on omniphobic 'RF paper' for paper-based electronics and MEMS. *Advanced Materials* **26**, 4677–4682 (2014).
131. Wu, L. *et al.* Manipulating oil droplets by superamphiphobic nozzle. *Small* **11**, 4837–4843 (2015).
132. Yan, K., Li, J., Pan, L. & Shi, Y. Inkjet printing for flexible and wearable electronics. *APL Materials* **8**, 120705 (2020).
133. Deegan, R. D. *et al.* Capillary flow as the cause of ring stains from dried liquid drops. *Nature* **389**, 827–829 (1997).
134. Ristenpart, W. D., Kim, P. G., Domingues, C., Wan, J. & Stone, H. A. Influence of substrate conductivity on circulation reversal in evaporating drops. *Physical Review Letters* **99**, 234502 (2007).
135. Kuang, M., Wang, L. & Song, Y. Controllable printing droplets for high-resolution patterns. *Advanced Materials* **26**, 6950–6958 (2014).
136. Viola, F. A. *et al.* A sub-150-nanometre-thick and ultraconformable solution-processed all-organic transistor. *Nature Communications* **12**, 5842 (2021).
137. De Gans, B. J., Duineveld, P. C. & Schubert, U. S. Inkjet printing of polymers: state of the art and future developments. *Advanced Materials* **16**, 203–213 (2004).

138. Li, K. *et al.* Facile full-color printing with a single transparent ink. *Science Advances* **7**, 1–8 (2021).

139. Yang, P., Zhang, L., Kang, D. J., Strahl, R. & Kraus, T. High-resolution jnkjet printing of quantum dot light-emitting microdiode arrays. *Advanced Optical Materials* **8**, 1901429 (2020).

140. Kamal, W. *et al.* Spatially patterned polymer dispersed liquid crystals for image-integrated smart windows. *Advanced Optical Materials* **10**, 2101748 (2022).

141. Viola, F. A. *et al.* A 13.56 MHz rectifier based on fully inkjet printed organic diodes. *Advanced Materials* **32**, 2002329 (2020).

142. Zhang, T., Wang, X., Li, T., Guo, Q. & Yang, J. Fabrication of flexible copper-based electronics with high-resolution and high-conductivity on paper via inkjet printing. *Journal of Materials Chemistry C* **2**, 286–294 (2014).

143. Mikolajek, M. *et al.* Control of the surface morphology of ceramic/polymer composite inks for inkjet printing. *Advanced Engineering Materials* **20**, 1800318 (2018).

144. Fu, S. *et al.* Fabrication of large-area bimodal sensors by all-inkjet-printing. *Advanced Materials Technologies* **4**, 1800703 (2019).

145. Carey, T. *et al.* Fully inkjet-printed two-dimensional material field-effect heterojunctions for wearable and textile electronics. *Nature Communications* **8**, 1202 (2017).

146. Seo, J. W. T. *et al.* Fully inkjet-printed, mechanically flexible MoS_2 nanosheet photodetectors. *ACS Applied Materials and Interfaces* **11**, 5675–5681 (2019).

147. Huang, T. T. & Wu, W. Scalable nanomanufacturing of inkjet-printed wearable energy storage devices. *Journal of Materials Chemistry A* **7**, 23280–23300 (2019).

148. Liu, L., Pei, Y., Ma, S., Sun, X. & Singler, T. J. Inkjet printing controllable polydopamine nanoparticle line array for transparent and flexible touch-sensing application. *Advanced Engineering Materials* **22**, 1901351 (2020).

149. Zhang, C. (John) *et al.* Additive-free MXene inks and direct printing of micro-supercapacitors. *Nature Communications* **10**, 1–9 (2019).

150. Shao, Y. *et al.* 3D crumpled ultrathin 1T MoS_2 for inkjet printing of Mg-ion asymmetric micro-supercapacitors. *ACS Nano* **14**, 7308–7318 (2020).

151. Giannakou, P., Tas, M. O., Le Borgne, B. & Shkunov, M. Water-transferred, inkjet-printed supercapacitors toward conformal and epidermal energy storage. *ACS Applied Materials and Interfaces* **12**, 8456–8465 (2020).

152. Galliker, P. *et al.* Direct printing of nanostructures by electrostatic autofocussing of ink nanodroplets. *Nature Communications* **3**, 890–899 (2012).

153. Mkhize, N. & Bhaskaran, H. Electrohydrodynamic jet printing: introductory concepts and considerations. *Small Science* **2100073**, 2100073 (2021).

154. Guo, L., Duan, Y., Huang, Y. A. & Yin, Z. Experimental study of the influence of ink properties and process parameters on ejection volume in electrohydrodynamic jet printing. *Micromachines* **9**, 522 (2018).

155. Yin, Z., Huang, Y., Duan, Y. & Zhang, H. *Electrohydrodynamic direct-writing for flexible electronic manufacturing*. (Singapore: Springer, 2018). doi:10.1007/978-981-10-4759-6

156. Seong, B. *et al.* Metal-mesh based transparent electrode on a 3-D curved surface by electrohydrodynamic jet printing. *Journal of Micromechanics and Microengineering* **24**, 097002 (2014).

157. Lee, A., Jin, H., Dang, H. W., Choi, K. H. & Ahn, K. H. Optimization of experimental parameters to determine the jetting regimes in electrohydrodynamic printing. *Langmuir* **29**, 13630–13639 (2013).

158. Onses, M. S., Sutanto, E., Ferreira, P. M., Alleyne, A. G. & Rogers, J. A. Mechanisms, capabilities, and applications of high-resolution electrohydrodynamic jet printing. *Small* **11**, 4237–4266 (2015).

159. Chen, C. H., Seville, D. A. & Aksay, I. A. Scaling laws for pulsed

electrohydrodynamic drop formation. *Applied Physics Letters* **89**, (2006).

160. Choi, H. K. *et al.* Scaling laws for jet pulsations associated with high-resolution electrohydrodynamic printing. *Applied Physics Letters* **92**, (2008).
161. He, B., Yang, S., Qin, Z., Wen, B. & Zhang, C. The roles of wettability and surface tension in droplet formation during inkjet printing. *Scientific Reports* **7**, 11841 (2017).
162. Lim, S., Park, S. H., An, T. K., Lee, H. S. & Kim, S. H. Electrohydrodynamic printing of poly(3,4-ethylenedioxythiophene):poly(4-styrenesulfonate) electrodes with ratio-optimized surfactant. *RSC Advances* **6**, 2004–2010 (2016).
163. Zhang, H. B., Edirisinghe, M. J. & Jayasinghe, S. N. Flow behaviour of dielectric liquids in an electric field. *Journal of Fluid Mechanics* **558**, 103–111 (2006).
164. Chang, J., He, J., Lei, Q. & Li, D. Electrohydrodynamic printing of microscale PEDOT:PSS-PEO features with tunable conductive/thermal properties. *ACS Applied Materials and Interfaces* **10**, 19116–19122 (2018).
165. Nguyen, V. D. & Byun, D. Mechanism of electrohydrodynamic printing based on ac voltage without a nozzle electrode. *Applied Physics Letters* **94**, 173509 (2009).
166. Scheideler, W. J. & Chen, C. H. The minimum flow rate scaling of Taylor cone-jets issued from a nozzle. *Applied Physics Letters* **104**, 024103 (2014).
167. Porter, B. F., Mkhize, N. & Bhaskaran, H. Nanoparticle assembly enabled by EHD-printed monolayers. *Microsystems & Nanoengineering* **3**, 17054 (2017).
168. Huang, Y. *et al.* Electrohydrodynamic direct-writing. *Nanoscale* **5**, 12007–12017 (2013).
169. Phung, T. H., Kim, S. & Kwon, K. S. A high speed electrohydrodynamic (EHD) jet printing method for line printing. *Journal of Micromechanics and Microengineering* **27**, 095003 (2017).
170. Sammons, P., Bollineni, S., Sibal, R. & Barton, K. Temperature and humidity variation effect on process behavior in electrohydrodynamic jet printing of a class

of optical adhesives. *In2017 International Solid Freeform Fabrication Symposium 2017* 1784–1794 (2017).

171. Shigeta, K. *et al.* Functional protein microarrays by electrohydrodynamic jet printing. *Analytical Chemistry* **84**, 10012–10018 (2012).
172. Sutanto, E., Tan, Y., Onses, M. S., Cunningham, B. T. & Alleyne, A. Electrohydrodynamic jet printing of micro-optical devices. *Manufacturing Letters* **2**, 4–7 (2014).
173. Can, T. T. T., Ko, H.-L. & Choi, W.-S. EHD-jet patterned MoS_2 on a high-k dielectric for high mobility in thin film transistor applications. *Nanotechnology* **32**, 245710 (2021).
174. Lee, J. G. *et al.* Electrohydrodynamic (EHD) dispensing of nanoliter DNA droplets for microarrays. *Biosensors and Bioelectronics* **21**, 2240–2247 (2006).
175. Park, J. U., Lee, J. H., Paik, U., Lu, Y. & Rogers, J. A. Nanoscale patterns of oligonucleotides formed by electrohydrodynamic jet printing with applications in biosensing and nanomaterials assembly. *Nano Letters* **8**, 4210–4216 (2008).
176. Zhu, M. *et al.* Electrohydrodynamically printed high-resolution full-color hybrid perovskites. *Advanced Functional Materials* **29**, 1903294 (2019).
177. Kim, B. H. *et al.* High-resolution patterns of quantum dots formed by electrohydrodynamic jet printing for light-emitting diodes. *Nano Letters* **15**, 969–973 (2015).
178. Kim, K. *et al.* High-resolution electrohydrodynamic jet printing of small-molecule organic light-emitting diodes. *Nanoscale* **7**, 13410–13415 (2015).
179. Wang, K., Paine, M. D. & Stark, J. P. W. Fully voltage-controlled electrohydrodynamic jet printing of conductive silver tracks with a sub-100 μm linewidth. *Journal of Applied Physics* **106**, 024907 (2009).
180. Criado-Gonzalez, M., Dominguez-Alfaro, A., Lopez-Larrea, N., Alegret, N. & Mecerreyes, D. Additive manufacturing of conducting polymers: recent advances,

challenges, and opportunities. *ACS Applied Polymer Materials* **3**, 2865–2883 (2021).

181. Jayasinghe, S. N. & Edirisinghe, M. J. Electric-field driven jetting from dielectric liquids. *Applied Physics Letters* **85**, 4243–4245 (2004).
182. Wei, C. *et al.* High-resolution ac-pulse modulated electrohydrodynamic jet printing on highly insulating substrates. *Journal of Micromechanics and Microengineering* **24**, (2014).
183. Cui, Z., Han, Y., Huang, Q., Dong, J. & Zhu, Y. Electrohydrodynamic printing of silver nanowires for flexible and stretchable electronics. *Nanoscale* **10**, 6806–6811 (2018).
184. Yang, S. M., Lee, Y. S., Jang, Y., Byun, D. & Choa, S. H. Electromechanical reliability of a flexible metal-grid transparent electrode prepared by electrohydrodynamic (EHD) jet printing. *Microelectronics Reliability* **65**, 151–159 (2016).
185. Teguh Yudistira, H. *et al.* Fabrication of terahertz metamaterial with high refractive index using high-resolution electrohydrodynamic jet printing. *Applied Physics Letters* **103**, 211106 (2013).
186. Han, Y. & Dong, J. Electrohydrodynamic (EHD) printing of molten metal ink for flexible and stretchable conductor with self-healing capability. *Advanced Materials Technologies* **3**, 1700268 (2018).
187. Kim, S. Y. *et al.* High-resolution electrohydrodynamic inkjet printing of stretchable metal oxide semiconductor transistors with high performance. *Nanoscale* **8**, 17113–17121 (2016).
188. Awais, M. N., Kim, H. C., Doh, Y. H. & Choi, K. H. ZrO_2 flexible printed resistive (memristive) switch through electrohydrodynamic printing process. *Thin Solid Films* **536**, 308–312 (2013).
189. Kim, K. *et al.* Direct writing and aligning of small-molecule organic semiconductor

crystals via “ dragging mode ” electrohydrodynamic jet printing for flexible organic field-effect transistor arrays. *The Journal of Physical Chemistry Letters* **8**, 5492–5500 (2017).

190. Liu, J. *et al.* High-performance, micrometer thick/conformal, transparent metal-network electrodes for flexible and curved electronic devices. *Advanced Materials Technologies* **3**, 1800155 (2018).
191. Ding, Y. *et al.* Flexible small-channel thin-film transistors by electrohydrodynamic lithography. *Nanoscale* **9**, 19050–19057 (2017).
192. Huang, Y. *et al.* Hyper-stretchable self-powered sensors based on electrohydrodynamically printed , self-similar piezoelectric nano/microfibers. *Nano Energy* **40**, 432–439 (2017).
193. Tang, X. *et al.* Electrohydrodynamic-jet-printed cinnamate-fluorinated cross-linked polymeric dielectrics for flexible and electrically stable operating organic thin-film transistors and integrated devices. *ACS Applied Materials & Interfaces* **13**, 50149–50162 (2021).
194. Su, S. *et al.* Direct microtip gocused electrohydrodynamic jet printing of tailored microlens arrays on PDMS nanofilm-modified substrate. *Advanced Materials Technologies* **6**, 2100449 (2021).
195. Rehman, M. M., Siddiqui, G. U., Doh, Y. H. & Choi, K. H. Highly flexible and electroforming free resistive switching behavior of tungsten disulfide flakes fabricated through advanced printing technology. *Semiconductor Science and Technology* **32**, 095001 (2017).
196. Dong, H. *et al.* Flexible pressure sensor with high sensitivity and fast response for electronic skin using near-field electrohydrodynamic direct writing. *Organic Electronics* **89**, 106044 (2021).
197. Rehman, M. M. *et al.* Resistive switching in all-printed, flexible and hybrid MoS_2-PVA nanocomposite based memristive device fabricated by reverse offset.

Scientific Reports **6**, 36195 (2016).

198. Siddiqui, G. U., Rehman, M. M., Yang, Y. J. & Choi, K. H. A two-dimensional hexagonal boron nitride/polymer nanocomposite for flexible resistive switching devices. *Journal of Materials Chemistry C* **5**, 862–871 (2017).
199. Wu, S., Li, J. S., Mai, J. & Chang, M. W. Three-dimensional electrohydrodynamic printing and spinning of flexible composite structures for oral multidrug forms. *ACS Applied Materials and Interfaces* **10**, 24876–24885 (2018).
200. Poellmann, M. J., Barton, K. L., Mishra, S. & Johnson, A. J. W. Patterned hydrogel substrates for cell culture with electrohydrodynamic jet printing. *Macromolecular bioscience* **11**, 1164–1168 (2011).
201. Selimis, A., Mironov, V. & Farsari, M. Direct laser writing: principles and materials for scaffold 3D printing. *Microelectronic Engineering* **132**, 83–89 (2015).
202. Bhawalkar, J. D., He, G. S. & Prasad, P. N. Nonlinear multiphoton processes in organic and polymeric materials. *Reports on Progress in Physics* **59**, 1041–1070 (1996).
203. Malinauskas, M., Farsari, M., Piskarskas, A. & Juodkazis, S. Ultrafast laser nanostructuring of photopolymers: A decade of advances. *Physics Reports* **533**, 1–31 (2013).
204. Claeyssens, F. *et al.* Three-dimensional biodegradable structures fabricated by two-photon polymerization. *Langmuir* **25**, 3219–3223 (2009).
205. LaFratta, C. N., Fourkas, J. T., Baldacchini, T. & Farrer, R. A. Multiphoton fabrication. *Angewandte Chemie - International Edition* **46**, 6238–6258 (2007).
206. Selimis, A., Mironov, V. & Farsari, M. Direct laser writing: principles and materials for scaffold 3D printing. *Microelectronic Engineering* **132**, 83–89 (2015).
207. Dinca, V. *et al.* Directed three-dimensional patterning of self-assembled peptide fibrils. *Nano Letters* **8**, 538–543 (2008).
208. Malinauskas, M. *et al.* 3D artificial polymeric scaffolds for stem cell growth

fabricated by femtosecond laser. *Lithuanian Journal of Physics* **50**, 75–82 (2010).

209. Maruo, S., Nakamura, O. & Kawata, S. Three-dimensional microfabrication with two-photon-absorbed photopolymerization. *Optics Letters* **22**, 132–134 (1997).
210. Teh, W. H. *et al.* SU-8 for real three-dimensional subdiffraction-limit two-photon microfabrication. *Applied Physics Letters* **84**, 4095–4097 (2004).
211. Haas, K. H. & Rose, K. Hybrid inorganic/organic polymers with nanoscale building blocks: Precursors, processing, properties and applications. *Reviews on Advanced Materials Science* **5**, 47–52 (2003).
212. Coenjarts, C. A. & Ober, C. K. Two-photon three-dimensional microfabrication of poly(dimethylsiloxane) elastomers. *Chemistry of Materials* **16**, 5556–5558 (2004).
213. Serbin, J. *et al.* Femtosecond laser-induced two-photon polymerization of inorganic–organic hybrid materials for applications in photonics. *Optics Letters* **28**, 301–303 (2003).
214. Mueller, P., Thiel, M. & Wegener, M. 3D direct laser writing using a 405 nm diode laser. *Optics Letters* **39**, 6847 (2014).
215. Bückmann, T. *et al.* Tailored 3D mechanical metamaterials made by dip-in direct-laser-writing optical lithography. *Advanced Materials* **24**, 2710–2714 (2012).
216. Cao, Y., Gan, Z., Jia, B., Evans, R. A. & Gu, M. High-photosensitive resin for super-resolution direct-laser-writing based on photoinhibited polymerization. *Optics Express* **19**, 19486 (2011).
217. Mohr-Weidenfeller, L., Häcker, A. V., Reinhardt, C. & Manske, E. Two-photon direct laser writing beyond the diffraction limit using the nanopositioning and nanomeasuring machine. *Nanomanufacturing and Metrology* **4**, 149–155 (2021).
218. Ams, M., Marshall, G. D., Dekker, P., Piper, J. A. & Withford, M. J. Ultrafast laser written active devices. *Laser and Photonics Reviews* **3**, 535–544 (2009).
219. Caño-García, M. *et al.* All-organic switching polarizer based on polymer waveguides and liquid crystals. *Optics Express* **26**, 9584–9594 (2018).

220. Landowski, A., Zepp, D., Wingerter, S., von Freymann, G. & Widera, A. Direct laser written polymer waveguides with out of plane couplers for optical chips. *APL Photonics* **2**, 106102 (2017).

221. Gissibl, T., Thiele, S., Herkommer, A. & Giessen, H. Two-photon direct laser writing of ultracompact multi-lens objectives. *Nature Photonics* **10**, 554–560 (2016).

222. Dietrich, P. I. *et al.* In situ 3D nanoprinting of free-form coupling elements for hybrid photonic integration. *Nature Photonics* **12**, 241–247 (2018).

223. Siegle, T., Remmel, M., Krämmer, S. & Kalt, H. Split-disk micro-lasers: tunable whispering gallery mode cavities. *APL Photonics* **2**, 096103 (2017).

224. Wu, Z.-L. *et al.* Polymer-based device fabrication and applications using direct laser writing technology. *Polymers* **11**, 553 (2019).

225. Chou, S. Y., Krauss, P. R. & Renstrom, P. J. Imprint of sub-25 nm vias and trenches in polymers. *Applied Physics Letters* **67**, 3114 (1995).

226. Chou, S. Y., Krauss, P. R. & Renstrom, P. J. Imprint lithography with 25-nanometer resolution. *Science* **272**, 85–87 (1996).

227. Guo, L. J. Recent progress in nanoimprint technology and its applications. *Journal of Physics D: Applied Physics* **37**, R123–R141 (2004).

228. Taniguchi, J. & Tokano, Y. Nanoimprint lithography : challenges and prospects. *Nanotechnology* **12**, 91–95 (2001).

229. Guo, L. J. Nanoimprint lithography: methods and material requirements. *Advanced Materials* **19**, 495–513 (2007).

230. Zhang, C. *et al.* Printed photonic elements: Nanoimprinting and beyond. *Journal of Materials Chemistry C* **4**, 5133–5153 (2016).

231. Kang, M. G., Kim, M. S., Kim, J. & Guo, L. J. Organic solar cells using nanoimprinted transparent metal electrodes. *Advanced Materials* **20**, 4408–4413 (2008).

232. Park, I. *et al.* Nanoscale patterning and electronics on flexible substrate by direct nanoimprinting of metallic nanoparticles. *Advanced Materials* **20**, 489–496 (2008).

233. Chen, X. *et al.* High-performance piezoelectric nanogenerators with imprinted P(VDF-TrFE)/$BaTiO_3$ nanocomposite micropillars for self-powered flexible sensors. *Small* **13**, 1–12 (2017).

234. Ahn, S., Cha, J., Myung, H., Kim, S. & Kang, S. Continuous ultraviolet roll nanoimprinting process for replicating large-scale nano- and micropatterns. *Applied Physics Letters* **89**, 213101 (2006).

235. Ahn, S. H. & Guo, L. J. High-speed roll-to-roll nanoimprint lithography on flexible plastic substrates. *Advanced materials* **20**, 2044–2049 (2008).

236. Ali, U. E. *et al.* A universal pick-and-place assembly for nanowires. *Small* **18**, 2201968 (2022).

237. Anastas, P. T. & Zimmerman, J. B. Design through the 12 principles of green engineering. *IEEE Engineering Management Review* **35**, 16–16 (2007).

238. Fiori, G. *et al.* Electronics based on two-dimensional materials. *Nature Nanotechnology* **9**, 768–779 (2014).

239. Schwierz, F. Graphene transistors. *Nature Nanotechnology* **5**, 487–496 (2010).

240. Wang, Q. H., Kalantar-Zadeh, K., Kis, A., Coleman, J. N. & Strano, M. S. Electronics and optoelectronics of two-dimensional transition metal dichalcogenides. *Nature Nanotechnology* **7**, 699–712 (2012).

241. Lopez-Sanchez, O., Lembke, D., Kayci, M., Radenovic, A. & Kis, A. Ultrasensitive photodetectors based on monolayer MoS_2. *Nature Nanotechnology* **8**, 497–501 (2013).

242. Bonaccorso, F., Sun, Z., Hasan, T. & Ferrari, A. C. Graphene photonics and optoelectronics. *Nature Photonics* **4**, 611–622 (2010).

243. Avouris, P., Freitag, M. & Perebeinos, V. Carbon-nanotube photonics and optoelectronics. *Nature Photonics* **2**, 341–350 (2008).

244. Cao, H., Tegenfeldt, J. O., Austin, R. H. & Chou, S. Y. Gradient nanostructures for interfacing microfluidics and nanofluidics. *Applied Physics Letters* **81**, 3058–3060 (2002).

245. Maeki, M., Kimura, N., Sato, Y., Harashima, H. & Tokeshi, M. Advances in microfluidics for lipid nanoparticles and extracellular vesicles and applications in drug delivery systems. *Advanced Drug Delivery Reviews* **128**, 84–100 (2018).

246. Shang, L., Cheng, Y. & Zhao, Y. Emerging droplet microfluidics. *Chemical Reviews* **117**, 7964–8040 (2017).

247. Liu, Y., Pharr, M. & Salvatore, G. A. Lab-on-skin: a review of flexible and stretchable electronics for wearable health monitoring. *ACS Nano* **11**, 9614–9635 (2017).

248. Kim, J., Campbell, A. S., de Ávila, B. E. F. & Wang, J. Wearable biosensors for healthcare monitoring. *Nature Biotechnology* **37**, 389–406 (2019).

249. Han, D. *et al.* Flexible hybrid electronics: direct interfacing of soft and hard electronics for wearable health monitoring. *Advanced Functional Materials* **26**, 8764–8775 (2016).

250. Wang, C. *et al.* Monitoring of the central blood pressure waveform via a conformal ultrasonic device. *Nature Biomedical Engineering* **2**, 687–695 (2018).

251. Wu, W. *et al.* Piezoelectricity of single-atomic-layer MoS_2 for energy conversion and piezotronics. *Nature* **514**, 470–474 (2014).

252. Zhang, D. W. *et al.* Graphene-based counter electrode for dye-sensitized solar cells. *Carbon* **49**, 5382–5388 (2011).

253. Shao, Y. *et al.* Graphene-based materials for flexible supercapacitors. *Chemical Society Reviews* **44**, 3639–3665 (2015).

254. de Luna, M. D. G., Warmadewanthi & Liu, J. C. Combined treatment of polishing wastewater and fluoride-containing wastewater from a semiconductor manufacturer. *Colloids and Surfaces A: Physicochemical and Engineering*

Aspects **347**, 64–68 (2009).

255. Kim, S. *et al.* Chemical use in the semiconductor manufacturing industry. *International Journal of Occupational and Environmental Health* **24**, 109–118 (2018).

256. Lin, C. P., Chang, H. K., Chang, Y. M., Chen, S. W. & Shu, C. M. Emergency response study for chemical releases in the high-tech industry in Taiwan-a semiconductor plant example. *Process Safety and Environmental Protection* **87**, 353–360 (2009).

257. Jang, M., Yoon, C., Park, J. & Kwon, O. Evaluation of hazardous chemicals with material safety data sheet and by-products of a photoresist used in the semiconductor-manufacturing industry. *Safety and Health at Work* **10**, 114–121 (2019).

258. Marano, D. E. *et al.* Exposure assessment among us workers employed in semiconductor wafer fabrication. *Journal of Occupational and Environmental Medicine* **52**, 1075–1081 (2010).

259. Lin, F., Lin, S. W. & Lu, W. M. Dynamic eco-efficiency evaluation of the semiconductor industry: a sustainable development perspective. *Environmental Monitoring and Assessment* **191**, 435 (2019).

260. Lin, F., Lin, S. W. & Lu, W. M. Sustainability assessment of Taiwan's semiconductor industry: a new hybrid model using combined analytic hierarchy process and two-stage additive network data envelopment analysis. *Sustainability* **10**, 1–16 (2018).

261. Chelton, C., Glowatz, M. & Mosovsky, J. Chemical hazards in the semiconductor industry. *IEEE Transactions on Education* **34**, 269–288 (1991).

262. Foecke, T. L. Hazardous waste minimization: part II waste minimization in the electronics products industries. *Journal of the Air Pollution Control Association* **38**, 283–291 (1988).

263. Hong, Y. *et al.* Solvent-free nanofabrication based on ice-assisted electron-beam lithography. *Nano Letters* **20**, 8841–8846 (2020).

264. Ben Halima, N. Poly(vinyl alcohol): review of its promising applications and insights into biodegradation. *RSC Advances* **6**, 39823–39832 (2016).

265. Chaouat, M. *et al.* A novel cross-linked poly(vinyl alcohol) (PVA) for vascular grafts. *Advanced Functional Materials* **18**, 2855–2861 (2008).

266. Pal, K., Banthia, A. K. & Majumdar, D. K. Biomedical evaluation of polyvinyl alcohol-gelatin esterified hydrogel for wound dressing. *Journal of Materials Science: Materials in Medicine* **18**, 1889–1894 (2007).

267. Choo, K., Ching, Y. C., Chuah, C. H., Julai, S. & Liou, N. S. Preparation and characterization of polyvinyl alcohol-chitosan composite films reinforced with cellulose nanofiber. *Materials* **9**, 644 (2016).

268. Kost, J. & Langer, R. Responsive polymeric delivery systems. *Advanced Drug Delivery Reviews* **46**, 125–148 (2012).

269. Pituru, S. M. *et al.* A review on the biocompatibility of PMMA-based dental materials for interim prosthetic restorations with a glimpse into their modern manufacturing techniques. *Materials* **13**, 2894 (2020).

270. Wendel, M., Lorenz, H. & Kotthaus, J. P. Sharpened electron beam deposited tips for high resolution atomic force microscope lithography and imaging. *Applied Physics Letters* **67**, 3732–3734 (1995).

271. Zhang, L. & Dong, J. High-rate tunable ultrasonic force regulated nanomachining lithography with an atomic force microscope. *Nanotechnology* **23**, 085303 (2012).

272. Liu, J. *et al.* Significant enhancement of the adhesion between metal films and polymer substrates by UV-ozone surface modification in nanoscale. *ACS Applied Materials and Interfaces* **8**, 30576–30582 (2016).

273. Ando, T., Uchihashi, T. & Kodera, N. High-speed AFM and applications to biomolecular systems. *Annual Review of Biophysics* **42**, 393–414 (2013).

274. Ando, T. High-speed atomic force microscopy and its future prospects. *Biophysical Reviews* **10**, 285–292 (2018).

275. Liu, C. Parallel scanning probe arrays: their applications. *Materials Today* **11**, 22–29 (2008).

276. Salaita, K. *et al.* Massively parallel dip-pen nanolithography with 55 000-pen two-dimensional arrays. *Angewandte Chemie - International Edition* **45**, 7220–7223 (2006).

277. Carroll, K. M. *et al.* Parallelization of thermochemical nanolithography. *Nanoscale* **6**, 1299–1304 (2014).

278. Radisavljevic, B., Radenovic, A., Brivio, J., Giacometti, V. & Kis, A. Single-layer MoS_2 transistors. *Nature Nanotechnology* **6**, 147–150 (2011).

279. Sebastian, A., Pendurthi, R., Choudhury, T. H., Redwing, J. M. & Das, S. Benchmarking monolayer MoS_2 and WS_2 field-effect transistors. *Nature Communications* **12**, 1–12 (2021).

280. Huh, W., Lee, D. & Lee, C. H. Memristors based on 2D materials as an artificial synapse for neuromorphic electronics. *Advanced Materials* **32**, 2002092 (2020).

281. Choi, M. *et al.* Flexible active-matrix organic light-emitting diode display enabled by MoS_2 thin-film transistor. *Science Advances* **4**, 1–8 (2018).

282. Wang, Q. *et al.* Nonvolatile infrared memory in MoS_2/PbS van der Waals heterostructures. *Science Advances* **4**, 1–8 (2018).

283. Lu, Y. *et al.* Controlling defects in continuous 2D GaS films for high-performance wavelength-tunable UV-discriminating photodetectors. *Advanced Materials* **32**, 1–12 (2020).

284. Sarkar, D. *et al.* MoS_2 field-effect transistor for next-generation label-free biosensors. *ACS Nano* **8**, 3992–4003 (2014).

285. Gan, X., Zhao, H. & Quan, X. Two-dimensional MoS_2: A promising building block for biosensors. *Biosensors and Bioelectronics* **89**, 56–71 (2017).

286. Zhao, J. *et al.* Highly sensitive MoS_2 humidity sensors array for noncontact sensation. *Advanced Materials* **29**, 1702076 (2017).

287. Choi, W. *et al.* Recent development of two-dimensional transition metal dichalcogenides and their applications. *Materials Today* **20**, 116–130 (2017).

288. Da Silveira Firmiano, E. G. *et al.* Supercapacitor electrodes obtained by directly bonding 2D MoS_2 on reduced graphene oxide. *Advanced Energy Materials* **4**, 1301380 (2014).

289. Peimyoo, N. *et al.* Chemically driven tunable light emission of charged and neutral excitons in monolayer WS_2. *ACS Nano* **8**, 11320–11329 (2014).

290. Li, H., Wu, J., Yin, Z. & Zhang, H. Preparation and applications of mechanically exfoliated single-layer and multilayer MoS_2 and WSe_2 nanosheets. *Accounts of Chemical Research* **47**, 1067–1075 (2014).

291. Coleman, J. N. *et al.* Two-dimensional nanosheets produced by liquid exfoliation of layered materials. *Science* **331**, 568–71 (2011).

292. Hernandez, Y. *et al.* High-yield production of graphene by liquid-phase exfoliation of graphite. *Nature Nanotechnology* **3**, 563–568 (2008).

293. Bergin, S. D. *et al.* Towards solutions of single-walled carbon nanotubes in common solvents. *Advanced Materials* **20**, 1876–1881 (2008).

294. Gaur, A. P. S. *et al.* Surface energy engineering for tunable wettability through controlled synthesis of MoS_2. *Nano Letters* **14**, 4314–4321 (2014).

295. Jawaid, A. *et al.* Mechanism for liquid phase exfoliation of MoS_2. *Chemistry of Materials* **28**, 337–348 (2016).

296. O'Neill, A., Khan, U. & Coleman, J. N. Preparation of high concentration dispersions of exfoliated MoS_2 with increased flake size. *Chemistry of Materials* **24**, 2414–2421 (2012).

297. Forsberg, V. *et al.* Exfoliated MoS_2 in water without additives. *PloS one* **11**, e0154522 (2016).

298. Zhou, K. G., Mao, N. N., Wang, H. X., Peng, Y. & Zhang, H. L. A mixed-solvent strategy for efficient exfoliation of inorganic graphene analogues. *Angewandte Chemie - International Edition* **50**, 10839–10842 (2011).

299. Li, J., Naiini, M. M., Vaziri, S., Lemme, M. C. & Östling, M. Inkjet printing of MoS_2. *Advanced Functional Materials* **24**, 6524–6531 (2014).

300. Pereira, N. M. *et al.* Aerosol-printed MoS_2 ink as a high sensitivity humidity sensor. *ACS Omega* **7**, 9388–9396 (2022).

301. Feng, X. *et al.* A fully printed flexible MoS_2 memristive artificial synapse with femtojoule switching energy. *Advanced Electronic Materials* **5**, 1900740 (2019).

302. Liang, L. & Meunier, V. First-principles Raman spectra of MoS_2, WS_2 and their heterostructures. *Nanoscale* **6**, 5394–5401 (2014).

303. Yu, F., Hu, M., Kang, F. & Lv, R. Flexible photodetector based on large-area few-layer MoS_2. *Progress in Natural Science: Materials International* **28**, 563–568 (2018).

304. Yin, Z. *et al.* Single-layer MoS_2 phototransistors. *ACS Nano* **6**, 74–80 (2012).

305. Fang, H. & Hu, W. Photogating in low dimensional photodetectors. *Advanced Science* **4**, 1700323 (2017).

306. Buscema, M. *et al.* Photocurrent generation with two-dimensional van der Waals semiconductors. *Chemical Society Reviews* **44**, 3691–3718 (2015).

307. Chen, T. *et al.* Ultrathin all-2D lateral graphene/GaS/graphene UV photodetectors by direct CVD growth. *ACS Applied Materials and Interfaces* **11**, 48172–48178 (2019).

308. Aso, S. I. *et al.* Incidence and mortality of acute myocardial infarction a population-based study including patients with out-of-hospital cardiac arrest. *International Heart Journal* **52**, 197–202 (2011).

309. Kamiya, T., Nomura, K. & Hosono, H. Present status of amorphous In–Ga–Zn–O thin-film transistors. *Science and Technology of Advanced Materials* **11**, 044305

(2010).

310. K. Nomura *et al.* Room-temperature fabrication of transparent flexible thin-film transistors using amorphous oxide semiconductors. *Nature* **432**, 488–492 (2004).

311. Chae, M.-S., Park, J. H., Son, H. W., Hwang, K. S. & Kim, T. G. IGZO-based electrolyte-gated field-effect transistor for in situ biological sensing platform. *Sensors and Actuators B: Chemical* **262**, 876–883 (2018).

312. Kim, H. & Kwon, J. Y. Enzyme immobilization on metal oxide semiconductors exploiting amine functionalized layer. *RSC Advances* **7**, 19656–19661 (2017).

313. Du, X., Li, Y., Motley, J. R., Stickle, W. F. & Herman, G. S. Glucose sensing using functionalized amorphous In-Ga-Zn-O field-effect transistors. *ACS Applied Materials and Interfaces* **8**, 7631–7637 (2016).

314. Kim, S. J. *et al.* Low-cost label-free electrical detection of artificial DNA nanostructures using solution-processed oxide thin-film transistors. *ACS Applied Materials and Interfaces* **5**, 10715–10720 (2013).

315. Ryu, B., Noh, H. K., Choi, E. A. & Chang, K. J. O-vacancy as the origin of negative bias illumination stress instability in amorphous In-Ga-Zn-O thin film transistors. *Applied Physics Letters* **97**, 1–4 (2010).

316. Oh, H. *et al.* Photon-accelerated negative bias instability involving subgap states creation in amorphous In-Ga-Zn-O thin film transistor. *Applied Physics Letters* **97**, 2008–2011 (2010).

317. Ortiz-conde, A., García-sánchez, F. J., Muci, J., Terán, A. & Liou, J. J. Microelectronics reliability revisiting MOSFET threshold voltage extraction methods. *Microelectronics Reliability* **53**, 90–104 (2013).

318. Sam, S. *et al.* Semiquantitative study of the EDC/NHS activation of acid terminal groups at modified porous silicon surfaces. *Langmuir* **26**, 809–814 (2010).

319. Kersey, L., Ebacher, V., Bazargan, V., Wang, R. & Stoeber, B. The effect of adhesion promoter on the adhesion of PDMS to different substrate materials. *Lab*

on a Chip **9**, 1002–1004 (2009).